Technische Universität München

Max-Planck-Institut für Plasmaphysik
Garching bei München

Characterisation and Mitigation of Chemical Erosion of Doped Carbon Materials

María Elena Juan Pardo

Vollständiger Abdruck der von der Fakultät für Maschinenwesen der Technischen Universität München zur Erlangung des akademischen Grades eines

Doktor-Ingenieurs

genehmigten Dissertation.

Vorsitzender:	Univ.-Prof. Dr.-Ing. H. Baier
Prüfer der Dissertation:	1. Hon.-Prof. Dr.-Ing., Dr.-Eng. (Japan) H. H. Bolt
	2. Univ.-Prof. Dr. mont. habil. E. Werner

Die Dissertation wurde am 16.06.2004 bei der Technischen Universität München eingereicht und durch die Fakultät für Maschinenwesen am 16.09.2004 angenommen.

To my family

Abstract

Carbon-based materials are the unique choice as *plasma-facing materials* (*PFM*s) for the successful operation of fusion devices with magnetically confined plasma, such as the planned *International Thermonuclear Experimental Reactor* (*ITER*), in order to withstand the highest expected power densities (up to 20 MW/m^2) without major degradation. Particularly, c*arbon fibre reinforced carbon* materials (*CFC*) has been suggested as good *PFM* choice for certain areas of the vessel wall of *ITER*, due to their improved mechanical properties compared to other carbon materials, in spite of the high costs associated with their manufacture.

But carbon-based materials possess a high chemical reactivity with hydrogen ions incident from the plasma as well as the ability to trap hydrogen in co-deposited layers, leading to short lifetime of the components and high tritium inventories, i.e. risk of radioactive contamination.

As an alternative to *CFCs*, new isotropic fine-grain graphites doped with metal carbides have been produced in order to reduce the high chemical erosion yield under hydrogen impact. This reduction would simultaneously diminish the co-deposition and increase the lifetime of the carbon components. With the addition of dopants further beneficial effects are searched, such as an enhancement of the thermal conductivity as well as improved mechanical properties. The chemical erosion behaviour and the deuterium retention of these improved doped graphites under deuterium bombardment are characterised in this work.

Due to the expectation of a more pronounced effect of doping with a finer distribution of the dopants, magnetron-sputtered nano-dispersed metal-doped carbon films were additionally investigated in order to elucidate the mechanisms of the mitigation of the chemical erosion.

The obtained results are very promising: at low temperatures and deuterium impact energies, dopant enrichment on the surface due to preferential sputtering of carbon strongly contributes to a reduction of the erosion yield; at elevated temperatures, an almost complete suppression of the chemical erosion yield measured by the production of CD_4 molecules is observed when dopants are nano-dispersed, which can be explained by a reduction of the activation energy for hydrogen release; and finally, the investigated doped graphites have a similar or even lower deuterium retention by implantation than other graphites.

Kurzfassung

Materialien auf der Basis von Kohlenstoff sind die bevorzugte Wahl für die erste dem Plasma gegenüberstehende Wand in Anlagen zur kontrollierten thermonuklearen Fusion mit magnetisch eingeschlossenem Wasserstoffplasma, wie dem geplanten Internationalen Tokamak Reaktor Experiment (*International Thermonuclear Experimental Reactor*, *ITER*). Kohlenstoffe können mit der höchsten bei ITER erwarteten Leistungsdichte (etwa 20 MW/m^2) ohne wesentliche Schädigung belastet werden. Vor allem mit Kohlenstofffasern verstärkter Kohlenstoff (*carbon fibre reinforced carbon, CFC*) ist, trotz seiner hohen Kosten, auf Grund seiner gegenüber normalem Kohlenstoff verbesserten mechanischen Eigenschaften für bestimmte sehr hoch belastete Wandstellen bei *ITER* vorgesehen.

Kohlenstoffmaterialien zeigen jedoch eine hohe chemische Reaktivität und Erosion durch die Wasserstoffionen aus dem Plasma, was zu einer kurzen Lebensdauer der Wandkacheln führt. Außerdem können sich auf den Wänden durch sogenannte Co-Deponierung, sowie direkte Deponierung von Kohlenwasserstoffen, große Mengen von Tritium in den Oberflächenschichten der Wände ansammeln. Diese akkumulierte Radioaktivität stellt ein großes Risiko dar.

Als eine mögliche Alternative zu *CFC*-Materialien wurden neue isotrope mit Metallkarbiden dotierte hergestellt. Diese sollten eine kleinere Erosion bei Wasserstoffbeschuss zeigen, das heißt eine längere Lebensdauer haben und zugleich das Aufsammeln von Wasserstoffisotopen durch Co-Deponierung vermindern. Durch die Dotierung erwartet man weitere Vorteile, wie die Erhöhung der Wärmeleitfähigkeit und eine Verbesserung der mechanischen Eigenschaften. Die hier vorgelegte Arbeit behandelt die chemische Erosion dieser verbesserten dotierten Kohlenstoffe und bringt Ergebnisse über das Aufsammeln von eingeschossenen Wasserstoffionen.

Da man erwartete, dass die Dotierung den Kohlenstoff umso deutlicher verbessert, je feiner und gleichmäßiger sie verteilt ist, wurden auch durch Magnetron-Zerstäubung hergestellte dotierte Kohlenstoffe mit nano-dispersen Dotierungen bezüglich der Mechanismen der Reduktion der chemischen Erosion untersucht.

Die Ergebnisse sind sehr vielversprechend. Bei niedrigen Temperaturen und kleinen Energien der Deuterium-Ionen zeigt sich eine verringerte Erosion auf Grund der angereicherten Dotierung in Folge der präferentiellen Erosion des Kohlenstoffs durch chemische Erosion. Bei höheren Temperaturen ist die chemische Erosion, die über die Emission von CD_4 gemessen wurde, bei den nano-dispers dotierten Graphiten fast

vollständig unterdrückt. Dies wird damit erklärt, dass durch die Dotierung die Aktivierungsenergie für die Freisetzung von Wasserstoff erniedrigt wird. Zusätzlich zeigen die dotierten Graphite eine kleinere Rückhaltung von eingeschossenem Wasserstoff als reiner Kohlenstoff.

Content

List of symbols

ϕ: flux

γ: maximum energy transfer factor

ρ: geometric density

σ_H: cross-section for the hydrogenation of sp^2 carbon atoms to sp^3 by thermalised hydrogen.

a-C: amorphous carbon film

a-C:H: amorphous hydrogenated carbon film

E_0: projectile energy

E_{act}: activation energy

E_{Hrel}: activation energy for hydrogen release

E_{th}: threshold energy

H^+: proton

$K(T)$: thermal conductivity (as a function of the temperature)

m_1: mass of the impinging projectile

m_2: mass of the target atom

S: area of the beam spot on the surface of the target (assuming homogeneous flux)

$S_n\ (E_0)$: nuclear stopping power at projectile energy E_0

T_e: electron temperature

T_{max}: temperature for which Y_{therm} is maximum

U_o: surface binding energy

Y: sputtering (erosion) yield

Y_{CD4}: CD_4-production yield

Y_{chem}: chemical erosion yield

Y_e: erosion yield defined as eroded *C* atoms per incident energetic *D*

Y_i: total erosion yield measured by mono-energetic ion beam

Y_{max}: maximum chemical erosion yield

Y_{phys}: physical sputtering yield

Y_{RES}: radiation enhanced sublimation sputtering yield

Y_{surf}: surface erosion yield

Y_{t+e}: erosion yield defined as eroded *C* atoms per incident thermal + energetic *D*

Y_{therm}: thermally activated erosion yield

Y_{tot}: total erosion yield

Abbreviations

CEIT: Centro de Estudios e Investigaciones Técnicas de Gipuzkoa

CFC: carbon fibre reinforced carbon

EDX: energy dispersive X-ray spectroscopy.

ELM: edge localised mode

HIP: hot isostatic pressing

IBA: ion beam analysis

IPP-Garching: Max-Planck-Institut für Plasmaphysik in Garching

ITER: International Thermonuclear Experimental Reactor

MC: metal carbide

MCMB: meso-carbon micro-beads

NRA: nuclear reaction analysis

OES: optical emission spectroscopy

PFM: plasma-facing material

RBS: Rutherford backscattering spectroscopy

RES: radiation enhanced sublimation

RF: radio frequency

RT: room temperature

SEM: scanning electron microscopy

SEP: Société Européene de Propulsion

TDS: thermal desorption spectroscopy

TEM: transmission electron microscopy

TOF: time-of-flight experiments

TT: Thermal Technology

XPS: X-ray photoelectron spectroscopy

XRD: X-ray diffraction

1. Introduction

In this introductory section the motivation for the thesis is presented. The whole work is embodied in an extensive and broad research project, and the objectives of both the global project and this particular thesis are marked. Finally, the structure of the work is outlined.

1.1. Carbon as plasma-facing material?

The aim of thermonuclear fusion research is to confine a hot *D*/*T* plasma long enough such that fusion processes between the hydrogen isotopes lead to a net energy gain (see Appendix A).

The successful operation of fusion devices with magnetically confined plasma, such as the planned tokamak *International Thermonuclear Experimental Reactor* (*ITER*), depends on the selection of plasma-facing components for withstanding the high power loads, as well as the particle and neutron fluxes from the plasma without major degradation [1-3]. The lifetime of the plasma-facing components and the contamination of the plasma will be determined by the erosion rates, as well as by the transport of eroded material into the plasma and its re-deposition at the vessel walls.

Particularly, transient and off-normal plasma conditions (e.g. *Edge Localised Modes* (*ELMs*), plasma disruptions, electrical arcs and slow transients of high power) are expected to deliver very high heat loads onto the *Plasma-Facing Materials* (*PFMs*). Due to their high thermal shock resistance, carbon-based materials are an essential choice as *PFM* in today's thermonuclear fusion experiments for those areas receiving the highest power densities (up to 20 MW/m^2), i.e. at the divertor plates [4,5], for which *carbon fibre reinforced carbon* materials (*CFC*s) have been suggested as a feasible good choice [6]. Additionally, carbon does not melt, has low activation by neutron irradiation, adequate thermo-mechanical properties and carbon atoms lead to low radiation energy losses when they enter the central plasma [7]. The broad experience accumulated with carbon-based materials as *PFM* during the last decades of operation with tokamaks, predicting a large

flexibility of operation due to the compatibility of a carbon divertor with an extended range of plasma regimes [8], is also an important advantage of carbon-based materials compared to metals.

But carbon-based materials also present some drawbacks. The most important disadvantage is certainly the high chemical reactivity of carbon with hydrogen ions coming from the plasma, which leads to very critical consequences:

- Short lifetime of the carbon-based components [9,10]. This is directly correlated with the large chemical erosion yield of carbon. For *ITER*, this fact means that the carbon tiles would have to be replaced after a certain number of plasma discharges, forcing to stop the device for a period of time and to spend money in new tiles, which is certainly undesirable.
- High tritium inventory [8,9,11,12], i.e. high risk of radioactive contamination. The variety of hydrocarbon groups formed as erosion products re-deposit in other locations of the vessel walls. The hydrocarbon layers grow about linearly with time of operation due to the ability of carbon to trap hydrogen (co-deposition) [13-15] and may consume the available Tritium in few plasma discharges. Additionally these hydrocarbon layers cause a significant permanent retention of radioactive tritium on the vessel walls.

Besides, an additional inconvenience of the *CFC*s developed for the *ITER* divertor is the high cost associated with their intricate manufacturing process.

One possible solution to these problems could be to limit the use of carbon-based materials in these devices. In fact, *CFCs* will probably be selected for *ITER* and their use will be restricted to those surfaces of the divertor plates receiving the highest heat loads, where it seems to be indispensable to successfully withstand transient events [7].

Another approach is to try to develop improved carbon-based materials with reduced chemical erosion yields. A reduction of the yields will directly reduce the co-deposition and extend the lifetime of the carbon components. As a result of the effort of various research groups, it was found that doping of carbon materials with small amounts (several at.%) of various elements (*B*, *Si*, *Ti*…) largely reduces their chemical reactivity with hydrogen and their chemical erosion [16-34]. On the other hand, a stronger reduction of the chemical erosion will be expected with finer and more homogeneous distribution of the dopants [24,29,30]. These ideas are the basis for the work presented in this thesis, which is included within the frame of a larger project dedicated to the study, design and elaboration

of isotropic fine-grain graphites improved by doping, as a carbon-based material alternative to *CFCs* for fusion applications.

However, adding dopants to carbon should not be detrimental to the other essential properties that *PFM*s demand, such as thermal conductivity, as it was found after *B* doping [17] or mechanical resistance. In fact, the development of new doped graphites for this application must focus on enhancing thermal conductivity as well as thermal-shock resistance; the latter of which implies high thermal conductivity, good mechanical resistance, low Young's modulus and low thermal expansion.

Metals and carbides are known to act as catalysts for graphitisation [35], causing an increase of the degree of graphitisation and the thermal conductivity. The catalytic effect of dopants is expected to be more efficient with a fine and homogeneous distribution of the dopant. At the same time, if these dopants form stable carbides, a fine and homogeneous distribution may reinforce the mechanical properties, as long as the initial powders for the carbon precursor have a small particle size.

All of the above-mentioned reveals promising development and optimisation possibilities of doped graphitic materials for their use in areas of high heat and particle loads of future fusion facilities. Up to now commercial materials (doped and undoped graphites and *CFCs*) have been investigated for this aim. But no systematic development of materials specifically designed for this purpose was known. This task is deemed necessary and achievable.

This project, consisting of developing and optimising improved doped graphites, is carried out in close collaboration between the Spanish materials research centre *CEIT* (*Centro de Estudios e Investigaciones Científicas de Gipuzkoa*) in San Sebastián, Spain and the *Max-Planck-Institut für Plasmaphysik in Garching*, Germany (*IPP-Garching*).

The global aim of the project is to demonstrate, on laboratory scale, the optimisation possibilities of doped isotropic fine-grain graphites, achieving strong reduction of chemical erosion, high thermal conductivity, high thermal-shock resistance and low cost. The intention is to establish solid bases for the subsequent industrial manufacture of a material that could compete with current *CFCs*, as a candidate material for the areas of higher heat and particle loads in the divertor of future devices. In the following, the specific aim of this thesis in the framework of the global project will be exhibited.

1.2. Objectives and structure of the thesis

Several doped-graphite samples produced at *CEIT* were routinely sent to *IPP-Garching* in order to study their chemical erosion and hydrogen retention. To analyse the dopant concentration of the samples they were investigated by *Rutherford Backscattering Spectrometry* (*RBS*) at a Tandem accelerator. To characterise the thermal diffusivity the laser flash method was employed. All of these are research topics included in this thesis. Hydrogen retention of the doped graphites produced at the *CEIT* has been systematically studied throughout two Diploma Theses [36,37] undertaken at *IPP-Garching*. A third Diploma Thesis [38], also carried out at *IPP-Garching* and intimately linked with the subject of this work, has produced and characterised magnetron doped carbon films for studies of the chemical erosion mechanisms.

Within this framework, the thesis presented here intends to bring together, comprise and unify all the collaboration work that has been performed at *IPP-Garching* with the following objectives:

- Characterisation of the chemical erosion behaviour of the improved doped graphites produced at *CEIT* by mono-energetic deuterium beam impact as a function of the energy (30 and 1000 eV), temperature (77 – 1100 K) and fluence (up to fluences of the order of 10^{25} D/m^2).
- Characterisation of the deuterium retention by mono-energetic deuterium implantation of the improved doped graphites produced at *CEIT* as a function of the fluence, in order to analyse the possible influence of porosity and degree of graphitisation as well as the influence of doping.
- Development of a mechanistic explanation of the effects of doping in the reduction of the chemical erosion of carbon that corresponds with the experimental observations.
- Evaluation of the capability of the development of the improved doped graphites produced at *CEIT* to reduce the chemical erosion by hydrogen impact.

This work is structured in five sections.

In this first **section 1**, the need of the investigation has been justified and the thesis has been embodied in the corpus of an extensive research programme, outlining its major objectives, both in the frame of the global project as well as in the particular scope of this work.

The following section (**section 2**) is dedicated to a review of the background knowledge and state of the art regarding the issues of this thesis. It has been divided into three parts: the first one, *erosion processes of pure carbon materials by hydrogen impact*, deals with the central and critical subject of the thesis: the mechanisms involved in the chemical erosion of carbon by hydrogen. This part tries to provide the general knowledge of the physics behind. The second part, *hydrogen inventory in carbon materials*, deals with the tritium retention. The last part, *doping of carbon materials*, reviews the specific knowledge acquired until now about the *influence of dopants on the thermo-mechanical properties*, as well as *on the chemical erosion mechanisms by hydrogen impact* and *on the retention and release of hydrogen*. The section concludes with the formulation of 3 open questions to which the thesis intends to answer.

In **section 3** the experimental part is presented. The two main groups of investigated materials are described: fine-grain carbide-doped graphites produced at *CEIT*, and magnetron-sputtered doped carbon films produced mainly at *IPP-Garching.* Following, the device where the erosion and implantation measurements were taken by mono-energetic deuterium beam impact (Garching high current ion source) is introduced. The section ends with a description of the measurement procedures used for each different kind of experiment carried out.

The main contribution of this thesis is condensed in **section 4** where, on the one hand, the results of the experiments together with a detailed discussion of them are presented and, on the other hand, answers to the open questions formulated at the end of the section 2 are given. For comparison and to facilitate a better interpretation of the results, supporting erosion measurements by plasmas were performed in collaboration with other research groups: University of Augsburg in Germany (at the planar inductively coupled *Radio Frequency* (*RF*) Plasma device) and *UCSD* (*University of California in San Diego*, CA, USA, at the plasma simulator PISCES-B). The results will also be examined here.

Finally, the conclusions and contributions of this thesis are summarised in **section 5**.

At the end of the thesis 4 appendixes with more detailed information related to this work can be found. They have been separated from the rest of the sections in an a attempt to avoid saturating the reader with too many theoretical details, calculations or pictures, such that the thesis could be read more fluently. **Appendix A** contains some basic notions about nuclear fusion and plasma-wall interactions, and an introduction to the next major step in fusion research, *ITER*. In **Appendix B** basic knowledge about the structure and properties of graphites can be found, together with a review of the catalytic

graphitisation by doping with metal carbides. **Appendix C** summarised the manufacturing procedure of the carbide-doped fine-grain graphites from *CEIT* and describes the procedure for the determination of the thermal conductivity data. Finally, **Appendix D**, shows detailed calculations of the characterisation of the mono-energetic deuterium ion beam profiles.

2. Background knowledge

This section is divided into three parts. The first one, *erosion processes of pure carbon materials by hydrogen impact*, deals with the crucial core subject of the thesis: the erosion mechanisms of carbon by hydrogen, and intends to provide the general knowledge of the physics involved. The second part is about *hydrogen inventory in pure carbon materials*, which deals with the problematic of the tritium retention. And the last one, *doping of carbon materials*, the various specific studies on the influence of dopants on the thermo-mechanical properties, as well as on the chemical erosion mechanisms by hydrogen impact and on the retention and release of hydrogen. The section concludes with the formulation of 3 open questions to which the thesis will try to answer.

2.1. Erosion mechanisms of pure carbon-based materials by hydrogen impact

This sub-section is dedicated to the main carbon-hydrogen interactions that take place in a fusion device, which are investigated in this thesis. More general information about plasma-wall interactions, together with some basic notions about nuclear fusion and an introduction to the next major step in fusion research, *ITER*, can be found in **Appendix A**.

The carbon-hydrogen interaction is a complex process, which depends on many factors, such as kind of hydrogen species, energy and angle of incident, together with the previous history of the carbon material and the possible synergy with other simultaneously arriving particles. But, despite the difficulties and because of already mentioned safety and efficiency reasons, it is necessary to understand the mechanisms implicated in the erosion of pure carbon for avoiding co-deposition and, in this way, searching solutions to one significant cause that increases the tritium inventory. For that reason, the erosion processes of pure carbon materials by hydrogen impact will be discussed.

For that, the term “sputtering” will often be used in this thesis to refer to “the erosion of material surfaces by particle impact” [39], as synonym of erosion in general. And “*erosion*

yield", *Y*, will also be a term frequently used for the quantification of an erosion process, as the average number of atoms removed from the target for each incident particle [40]:

$$Y = \frac{\sum \text{removed atoms}}{\sum \text{incident particles}} \tag{2.1}$$

Y is usually investigated by weight loss measurements, whenever the number of incident particles can also be quantified.

For carbon, several different erosion processes have been identified: physical sputtering, chemical sputtering and radiation enhanced sublimation. Besides, different regimes of the chemical sputtering have been distinguished. Hence, for carbon, the *total erosion yield*, Y_{tot} is given by adding up of the *physical sputtering yield*, Y_{phys}, *chemical sputtering yield*, Y_{chem} and *radiation enhanced sublimation sputtering yield*, Y_{RES} [41]:

$$Y_{tot} = Y_{phys} + \underbrace{Y_{surf} + Y_{therm}(1 + DY_{phys})}_{Y_{chem}} + Y_{RES} \tag{2.2}$$

- Physical sputtering, given by Y_{phys}, is caused by collisions between the incoming hydrogen particles and the carbon atoms in the surface layers of the solid, which initiate collisions in the carbon lattice. Surface atoms that have received an energy larger than the surface binding energy and a momentum in the outward direction, are emitted i.e. sputtered.

- Chemical erosion or chemical sputtering (both terms will be used indistinctively as synonyms), given by Y_{chem}, is the "formation of volatile molecules on the target surface due to a chemical reaction between the incident particles and the target atoms" [42]. Y_{chem} cannot only be determined by weight loss measurements, but also by investigations of the molecule formation during the erosion process, e.g. by optical spectroscopy or by *quadrupole mass spectrometry* (*QMS*).

  Different regimes simultaneously contribute to Y_{chem}: a surface regime (also called ion-induced erosion), given by Y_{surf}, which takes places at low temperatures and low hydrogen impact energies; and a thermally activated regime, given by Y_{therm}, which occurs when temperature increases. Besides, the thermal erosion is enhanced by radiation damage, which can be assumed

proportional to Y_{phys}. The term D in equation 2.2. is a constant depending on the isotope mass of the incident particle.

It should be noted that the given definition of chemical erosion applied to the particular case of hydrogen bombardment, differs from that used by other authors, such as Hopf, von Keudell and Jacob [43], who accept the definition given by Winters and Coburn [44,45]. For these authors, "chemical erosion" would only refer to what in this thesis has been named *thermally activated regime* and the term "chemical sputtering" would designate what here is called *surface regime*.

- *Radiation enhanced sublimation* or *RES*, given by Y_{RES}, is a particular erosion mechanism of carbon. At high impact energies and temperatures above 1200 K, atomic carbon is emitted.

In the following, the meaning of each term of the equation 2.2 will be clarified more in detail.

2.1.1. Physical sputtering (Y_{phys})

Physical sputtering is the most important mechanism of impurity release since it occurs for all materials independently of the chemical nature, wall condition and wall temperature. It basically consists in the removal of atoms due to energetic particle bombardment, which reverse their momentum in a collision, transferring enough energy to a surface (or subsurface) atom or group such that it exceeds the surface binding energy. Thus, Y_{phys} decreases with increasing surface binding energy, and it has a *threshold energy*, E_{th}, since no surface atoms leave the solid if the maximum transferable energy is below the binding energy.

As an example to illustrate this, **Fig. 2.1** shows the physical sputtering yield of carbon under helium bombardment as a function of the helium impact energy. Above E_{th} (30.2 eV calculated by fitting of measured data and shown in **Fig. 2.1** [46], 25.4 eV calculated with the programme TRIM.SP [47]), Y_{phys} increases monotonically with increasing energy of the incident helium particles. At energies above 1 keV; the helium particles penetrate deeper into the solid and deposit less energy close to the surface, so that Y_{phys} presents a maximum at around 1 keV.

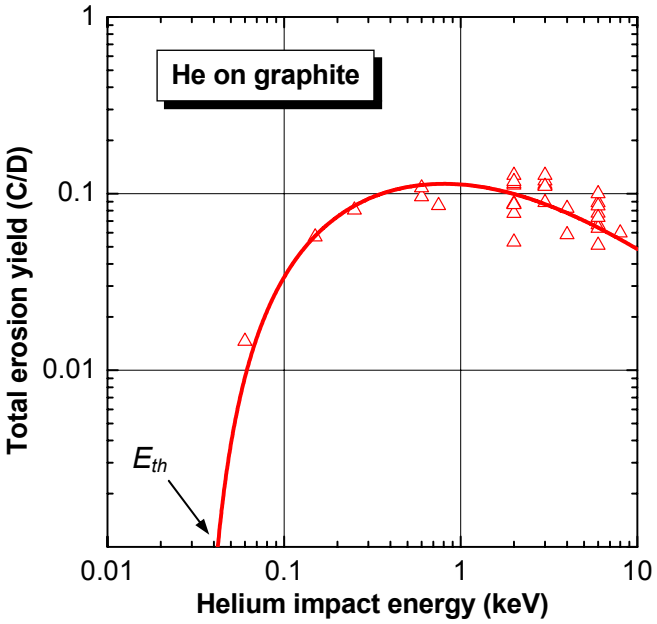

Fig. 2.1. Physical sputtering yield of carbon by helium bombardment as a function of the helium impact energy [46].

The physical sputtering process is reasonably understood and documented [40,46-52]. The most widely used analytical formula for calculating Y_{phys} was introduced by Bohdansky in 1984 [50], who describes it as a function of the *projectile energy*, E_0 and angle of incidence. At normal incidence results in:

$$Y_{phys}(E_0) = QS_n(E_0)\left[1-\left(\frac{E_{th}}{E_0}\right)^{2/3}\right]\left(1-\frac{E_{th}}{E_0}\right)^2 \tag{2.3}$$

where E_{th} and Q are fitting parameters, and $S_n(E_0)$ is the nuclear stopping power for E_0.

Bohdansky *et al.* [50,53] also made an effort to describe empirically E_{th} as a function of the mass ratio by the following formula:

$$E_{th} = \begin{cases} \dfrac{U_o}{\gamma(1-\gamma)} & \text{for } \dfrac{m_1}{m_2} \le 0.2 \\ 8U_0\left(\dfrac{m_1}{m_2}\right)^{2/5} & \text{for } \dfrac{m_1}{m_2} > 0.2 \end{cases} \tag{2.4}$$

with

$$\gamma = \frac{4m_1m_2}{(m_1+m_2)^2} \tag{2.5}$$

where γ is the maximum energy transfer factor, U_o is the surface binding energy and m_1 and m_2 are the masses of the projectile and the target atom, respectively. For the surface binding energy the heat of sublimation is usually taken [53]. For the case of graphite this is 7.4 eV [54], resulting in E_{th} of 30 eV for D^+ and 40 eV for H^+ bombardment. Other authors,

such as Matsunami *et al.* [55] or Smith *et al.* [56] use different fittings, but they obtain for E_{th} virtually the same value as given by equation 2.4. García-Rosales *et al.* revised the Bohdansky's formula [51] based on new effective and systematic fittings of a large number of experimental and calculated sputtering yield data accumulated in three decades at *IPP-Garching*. They described differently the nuclear stopping, S_n, using the Kr-C interaction potential with the reduced energy ε: $S_n^{KrC}(\varepsilon)$. This formula results in a better fit of the sputtering data especially at low incident energies, resulting in E_{th} of 28 eV for D^+. Very recently, Eckstein and Preuss revised again the formula for physical sputtering [57], proposing:

$$Y_{phys}(E_0) = qS_n^{KrC}(\varepsilon)\frac{\left(\frac{E_0}{E_{th}}-1\right)^{\mu}}{\lambda+\left(\frac{E_0}{E_{th}}-1\right)^{\mu}} \tag{2.6}$$

q is used as a new fit parameter. E_{th} appears in both nominator and denominator, to ensure that the high energy behaviour is not affected by E_{th}. μ is an empirical exponent used to describe the strength of the decrease near E_{th}. And the third additional parameter, λ, generates the onset of the decrease, as proposed in [58]. This formula was not obtained by fitting of experimental data, but of calculated sputtering yields from [46,51].

2.1.2. Chemical erosion (Y_{chem}) and its two regimes (Y_{surf} and Y_{therm})

Chemical erosion, i.e. "the formation of volatile molecules on the target surface due to a chemical reaction between the incident particles and the target atoms" [42], is especially observable under hydrogen and oxygen bombardment by the formation of molecules, such as CH_4 and CO. This section will concentrate on chemical erosion by hydrogen impact.

The erosion processes of carbon under deuterium bombardment in dependence of impact energy are summarised in **Fig. 2.2**. Y_{phys} represents the energy dependence of the physical sputtering calculated with the revised Bohdansky's formula [51]. At low incident energies the measured yields are well above the calculated yields. This is due to the chemical sputtering. At high temperatures, the total erosion yield (Y_{tot}) is much larger than the single contribution of Y_{phys} (see $Y_{hot\ (550\text{-}850\ K)}$ in **Fig. 2.2**), and also at *room temperature* (*RT*) and low deuterium impact energies (even below E_{th}, see Y_{RT} in **Fig. 2.2**).

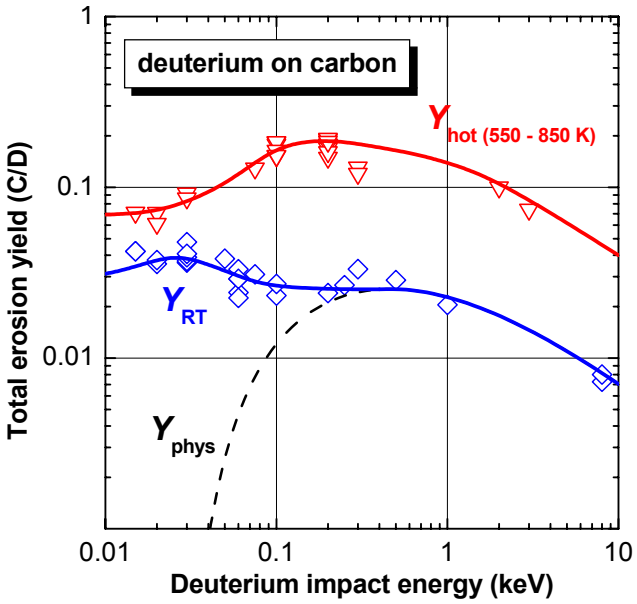

Fig. 2.2. Impact energy dependence of the total erosion yield (Y_{tot}) of deuterium on carbon obtained by weight loss with flux densities of 1-8 $\times$ 10^{-19} m^{-2} s^{-1} [59]. For $Y_{hot\ (550\text{-}850\ K)}$ and Y_{RT} the data were measured at temperatures between 550 and 850 K where the erosion was maximum and at *RT*, respectively.

These chemical erosion processes of carbon materials under hydrogen bombardment have been investigated by different groups in laboratory experiments for several years [41,60-71]. Erents *et al.* [60] were one of the first authors who published in 1976 on chemical erosion as a function of the temperature by controlled ion beam. They investigated the methane (CH_4, mass 16) formation during proton ion bombardment, as well as the deutero-methane (CD_4, mass 20) formation under deuterium bombardment, and both masses showed a pronounced maximum, Y_{max} at around 850 and 800 K (for CD_4 and CH_4, respectively). They explained quantitatively the maximum by a developed model that Balooch and Olander [60] had already suggested for the interaction of atomic hydrogen beam with carbon surfaces. The model assumes a rate for the formation of CH_4 directly proportional to the surface concentration of hydrogen atoms, and predicts the formation of the peak as the competition of two processes under steady state conditions: the formation of CH_4 molecules and the thermal desorption of H_2. This model also predicts a dependence of the yield with *flux*, ϕ, as $1/\phi$ at high incident fluxes. Further, Roth *et al.* [62] observed a dependence of Y_{max} on the ion energy, which they suggested to be in connexion with surface damage due to the energetic ion bombardment. Yamada and Sone [63] also interpreted this fact in 1983 as a dependence of the bond breaking and carbon displacement in the implanted layer produced by the energy deposited by the ions. In 1995, Küppers [66] reported in great detail the atomistic steps of the reaction of thermal atomic hydrogen with an *amorphous hydrogenated carbon layer* (*a-C:H*). Horn *et al.* [65] recapitulated each elementary reaction step in a schematic circular diagram (shown in **Fig. 2.3**), which illustratively presents all processes together.

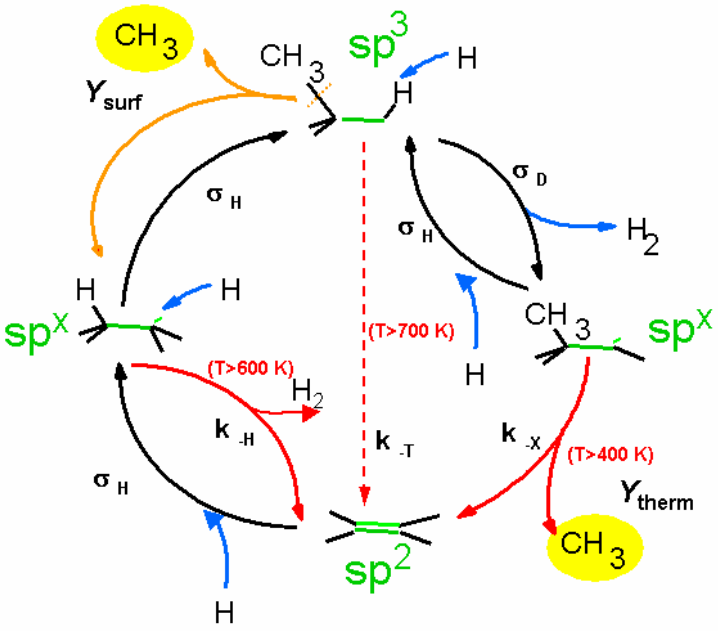

Fig. 2.3. Schematic diagram of the reaction steps of the hydrogen impact induced chemical erosion of *amorphous hydrogenated carbon layers* (*a-C:H*). The elementary reactions are illustrated at an individual two carbon entity of the *a-C:H* surface at the indicated temperature regions [65,67].

In 1996 Roth and García-Rosales [67] extended the last investigations to the case of energetic ion bombardment, proposing an analytical description, which is still used at present. Mech *et al.* [69] confirmed the validity of the model of Küppers and co-workers for the erosion of carbon by atomic hydrogen and also of its adaptation to the case of hydrogen ions made by Roth and García-Rosales [67]. Mech *et al.* improved both models by the introduction of distributed activation energies for the atom-induced thermal release of methane and hydrogen, by the use of a slightly activated abstraction process (and not constant cross section) and by the treatment of the implantation zone as one “effective surface” (greater than the geometrical surface, also taking into account internal surfaces that are well connected to the geometrical one via ion induced damage pathways).

All these last investigations lead to the identification of essentially two regimes of the chemical erosion of carbon: a thermally activated regime, described by Y_{therm}, and a surface regime or also called ion-induced release of hydrocarbon groups, described by Y_{surf}.

a) Thermally activated regime (Y_{therm})

The arriving energetic hydrogen ions are slowed down in collisions with carbon atoms and electrons in the solid, producing sp^3 hydrocarbon complexes via an intermediate radical stage sp^x after their interaction, either with sp^2-hybridised carbon atoms at the edges of graphitic planes or with broken bonds (see **Fig. 2.3** on the left). This process of

hydrogenation is proportional to the cross section σ_H= 1.1 Å^2. Hydrogen abstraction, with a cross-section σ_D = 0.05 Å^2, and re-hydrogenation, again with σ_H = 1.1 Å^2, also take place by further bombardment with thermal atomic hydrogen (**Fig. 2.3** on the right). The hydrogen abstraction also leaves another radical stage sp^x, but its concentration is much smaller than the sp^3 concentration due to the large differences in the cross-sections of the processes. At temperatures above 400 K and in the presence of energetic hydrogen, hydrocarbon groups in the neighbourhood of sp^x radicals can be thermally released, returning the substrate to the basic graphitic sp^2 configuration by the joint of the two neighbouring free bonds to a double bond. This is the first mechanism of chemical erosion. If the temperature is sufficiently high (>600 K) to allow the ion-induced recombination of hydrogen, the hydrogenation process is interrupted; the concentration of sp^3 decreases and thus, the chemical erosion is reduced. As a result of the competition between the supply of sp^x radical centres with neighbouring hydrocarbon groups (balanced by the hydrogen abstraction and the re-hydrogenation), which are thermally desorbed, and the hydrogen release, Y_{therm} exhibits its maximum at the temperature T_{max}, between 600 and 900 K, depending on the hydrogen isotope, flux, energy of ions and presence of radiation damage in the material [72]. By stopping the hydrogen irradiation, the only possible mechanism to release hydrocarbon complexes occurs above 700 K, returning carbon atoms from the sp^3 to the sp^2-hybridisation state (see centre dotted vertical line in **Fig. 2.3**).

It has quickly been commented that Y_{therm} also depends on the radiation damage. The energy deposited by the increased incident hydrogen ions leads to breaking *C-C* bonds, creating open bonds and imperfections, which are new active sites for successive reactions with the incoming ions. The radiation damage shows an energy dependency very similar to the one of physical sputtering, such that this damage can be described by a multiplicative term that includes Y_{phys}. This is the meaning of $Y_{therm}DY_{phys}$ in the equation 2.2, where D is a constant depending on the isotope mass of the impacting particle (for deuterium, D = 125). The radiation damage process also shows a threshold energy E_{th} for the production of damage. Above this threshold energy the graphite lattice is amorphised and the variation in the erosion yield due to the structure of the material is reduced [73]. Below E_{th}, the initial crystalline perfection determines Y_{therm} [72,74].

b) Surface regime (Y_{surf})

This chemical regime, which is described by Y_{surf}, takes place at low surface temperatures and low ion energies (below 100 eV). Under those conditions only the surface of the carbon material is hydrogenated; C_xH_y hydrocarbon radicals are bonded to sp^3 hybridised carbon, carbon of the lattice with an energy much smaller than the *C-C* binding energy in the network, leading to an ion-induced desorption of hydrocarbon radicals. Roth and García-Rosales [67] have illustrated this process as physical sputtering of the superficial hydrocarbon groups by the incident hydrogen ions, with very low threshold energy, in the order of few eV (1-2 eV or even lower). As the emission of hydrocarbon radicals can only occur at the surface, this term was named Y_{surf}. They have also called this regime as kinetic hydrocarbon emission. But some authors disagree with this explanation. One of them, Vietzke [70] has recently measured by *time-of flight experiment*s (*TOF*) the energy distribution of chemically released CD_4 and CD_3 from graphite by energetic D^+ impact, as well as by a synergistic reaction due to Ne^+ and D^0 atoms. Although he determined a non-thermal component in the emitted species, he elucidated that the averaged velocity of molecules when leaving the graphite would have to be four times larger than the experimental results to explain this erosion process by a kinetic hydrocarbon emission (even if only assuming a binding energy of 1 eV). He observed a significant time delay (in the range of ms) of the CD_4 signal after switching off the ion beam and by a constant atomic deuterium flux, i.e. no abrupt decrease of the signal as expected from physical sputtering.

Salonen *et al.* also explains in a different way this chemical erosion regime, as the breaking of bonds between C_xH_y hydrocarbon groups and sp^3 hybridised carbon of the lattice by the incident hydrogen ions, leading to C_xH_y- emission [75,76]. Hopf *et al.* [43,77,78] recently published on the chemical sputtering of hydrocarbon films by low-energy Ar^+ ion and *H* atom impact. After their investigations, they agree with the argumentations of Vietzke and Salonen *et al.*, and they also propose for this chemical erosion regime a similar mechanism, which consists of breaking of carbon bonds due to the incident ions and instantaneous passivation of them by the abundant flux of atomic hydrogen, leading to the formation of hydrocarbon molecules in the common range of ions and hydrogen atoms, until they are diffused to the surface and desorbed.

2.1.3. Radiation Enhanced Sublimation, RES (Y_{RES})

Radiation Enhanced Sublimation (*RES*) is a particular erosion mechanism of carbon-based materials, which has also been investigated and is well reviewed [79-83]. At temperatures above 1200 K and by irradiation with energetic ions, Y_{tot} increases monotonically with increasing temperature [82]. In opposition to the thermal sublimation of carbon up to temperatures of 2000 K, only mono-atomic carbon is emitted. The accepted mechanistic explanation for this erosion process is the following: carbon interstitials are produced by incident energetic particles, some of them diffusing to the surface and sublimating with an activation energy below 1 eV (due to the low binding energy of interstitials, peculiar property of carbon), which is much less than needed for thermal sublimation (7.4 eV [54]). Again, with regard to the activation energy for the formation of interstitials, this process also presents an E_{th}. The model suggests a dependence of Y_{RES} with the *flux* ϕ, such that $Y_{RES} \propto \phi^{-0.25}$ [81,83], which has experimentally been corroborated for the case of high fluxes (ϕ between 10^{19}-10^{21} $m^{-2}s^{-2}$) [83].

Due to the dependence of the migration of interstitials with the orientation of the graphite planes, Y_{RES} also depends on the structure of the carbon material [82].

2.2. Hydrogen inventory in pure carbon materials

It is of high interest for the researchers of the fusion community to have a realistic prediction of the stored tritium inventory in future fusion devices, due to its key role for safety considerations. The total amount of tritium retained in the device can be basically foreseen as the adding up of, on the one hand, the retained tritium by implantation into the *PFMs* and, on the other hand, the tritium inventory retained in deposited hydrocarbon layers. This section contains a brief description of the mechanisms of hydrogen retention and hydrogen release.

2.2.1. Hydrogen retention

A lot of investigations in the last decades were performed in order to better understand the mechanisms involved in the hydrogen retention of carbon-based materials [60,84-94]: reflection, implantation and reemission of impacting hydrogen, diffusion,

recombination and trapping of atomic hydrogen and additional adsorption and dissociation for molecular hydrogen. The influence of the structure of carbon-based materials on the nano- and micro-metric scale can also affect some of these mechanisms and it has to be taken into account [86-93,95-98].

a) Implantation

When a carbon material is bombarded with energetic hydrogen ions or neutrals, a part of them are backscattered and the rest are implanted. The implanted ones are slowed down and stopped, and they remain all trapped in the surface near layers how far the impacting hydrogen can penetrate, until this surface is saturated. After further implantation, the so-called *implantation zone* is enlarged until the surface of the material. At *RT* the saturation level is about 0.4 *H/C*; this ratio has been found to be independent of the carbon structure [99-103] and implantation energy [92] but strongly dependent on the temperature. The implantation range is of about several 10 nm for typical energies of around 1 keV [104], resulting in a total trapped inventory of the order of several 10^{21} hydrogen atoms/m^2. If all available hydrogen trap sites are already occupied and fluence further increases, a growing fraction of the incident flux is re-emitted as molecules until reaching stationary state, in which incident and re-emitted flux are nearly balanced. For higher fluences hydrogen retention is governed by diffusion.

b) Diffusion

A second mechanism of hydrogen retention is the diffusion of hydrogen beyond the implantation zone into the bulk of the material until a trapping site is found [85,92,94,97,105]. Diffusion can take place along grain boundaries or internal surfaces (open porosity, with an *activation energy,* E_{act} of 1 eV, which already occurs at *RT*), as well as along the graphite layers (E_{act} of 2.5 eV) and even perpendicular to the graphite layers above temperatures of 2000 K (E_{act} of 4 eV) [89].

The so-called *inherent trap concentration* or concentration of hydrogen trapped beyond the implantation zone is not yet well known, but it has been estimated to be of the order of 10^{-4}-10^{-3} for graphite [94]. The diffusion range may exceed several mm. The hydrogen inventory trapped by diffusion into the bulk slowly increases with incident fluence and saturation has not been observed even for the highest fluences reached in laboratory experiments (~10^{25} atoms/m^2) [105]. At this fluence, the hydrogen trapped

beyond the implantation zone is also the same as for the case of implantation, of several 10^{21} atoms/m^2. For fluences above 10^{25} atoms/m^2 the migrated and trapped hydrogen beyond the implantation zone exceeds the inventory trapped in the implantation zone [94].

c) Co-deposition

The co-deposition is actually the major problem of carbon materials for their application as *PFM*. Due to the impacting plasma particles, some of the carbon atoms are eroded and deposited together with hydrogen on surrounding surfaces. The layers formed have ratio of about 0.4 *H/C* when the surface is bombarded with ions at *RT* and there was not found any limit to their proliferation [106], growing about linearly with the discharge time [106]. This mechanism could most likely be the responsible of the largest tritium inventory in plasma-facing components of *D-T* burning fusion plasmas. W. Jacob *et al*. have recently investigated in great detail the plasma-assisted growth of such kind of thin hydrocarbon films [107-110].

2.2.2. Hydrogen release and hydrocarbon formation

During both irradiation and thermal desorption experiments hydrogen is released from the carbon material in form of atoms, molecules and hydrocarbons, depending on the implantation temperature and energy. When ion irradiation energies are in the keV range, the dominant hydrocarbon group formed is CH_4 [111-113]; as it has already been seen in section 2.1.2, its formation has a maximum at around 800 K. However, at energies below 1 keV the formation of heavier hydrocarbons becomes gradually more dominant [113].

At low temperatures hydrogen is released only in the form of molecules, showing a maximum production at around 1000 K. Up to temperatures of about 900-1100 K an increasing fraction of the implanted hydrogen is released in atomic form [114-116]; which has a peak around 1100-1200 K. During steady-state irradiation, where all incident hydrogen is essentially released, the fraction of atomic hydrogen released increases with increasing graphite temperature. At temperatures up to 2000 K nearly all hydrogen is reemitted in the form of atoms (due to ordinary thermo-dynamical dissociation of hydrogen), depending on both the implantation energy and flux [116,117].

2.3. Doping of carbon materials

In this sub-section the influence of dopants on the thermo-mechanical properties, as well as on the erosion behaviour by hydrogen impact and on the retention and release of hydrogen, will be reviewed.

2.3.1. Influence of dopants on the thermo-mechanical properties

It has been observed that the addition of small amounts of metal carbides to carbon in the first steps of the manufacturing process catalyses the graphitisation [35,118-120]. A proposed mechanism for this catalytic effect of the carbides is the dissolution of disordered carbon in a molten metal carbide nano-particle, followed by the precipitation as ordered graphite [121]. More details about the catalytic graphitisation by doping with metal carbides can be found in **Appendix B**.

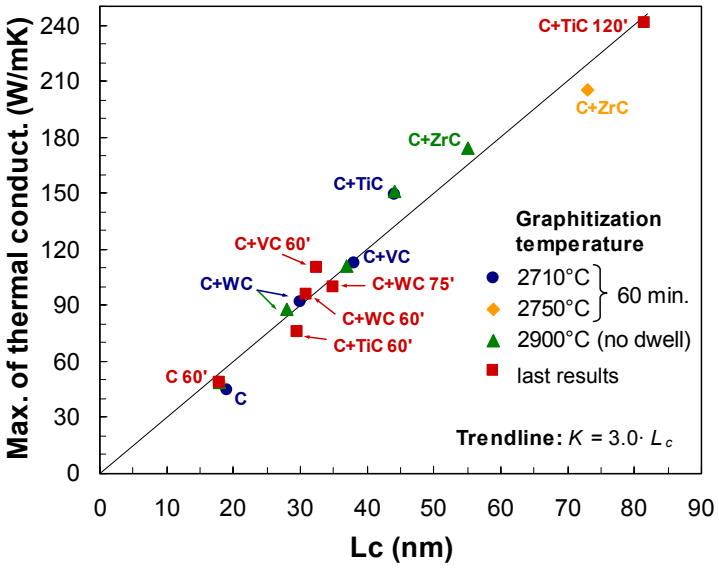

Fig. 2.4. Maximum thermal conductivity as a function of the size of the graphitic crystals, L_C, obtained for different fine-grain graphites doped with *ZrC*, V_8C_7, *WC* and *TiC* manufactured at the *CEIT* [120,125].

The increase of the crystallite size leads to higher thermal conductivities of these doped graphites [33,122-124] compared to pure graphite. García-Rosales *et al.* have investigated this effect at *CEIT* during the last years. They have found out that the maximum thermal conductivity is linearly related to the *height of the graphitic crystals*, L_C by a factor of 3, as can be confirmed in **Fig. 2.4** [120,125]. The maximum value of thermal conductivity is taken in order to assure that the mean free path of the phonons is

governed by the same feature (in this case, the crystalline borders). Although this simple relation has yet not been clearly understood, if future measurements prove its reproducibility, it would imply the possibility of determining thermal conductivity from the size of the graphitic crystals, which is a much easier and faster measurement.

Adding dopants to the initial material is not only harmless to its mechanical properties, but it has shown to substantially improve them in some cases. This behaviour obeys mainly to two facts: the reinforcement effect of carbides in a carbon matrix, and the change in the morphology of porosity. In section 3.1.1 more details will be offered on the main thermo-mechanical properties of the fine-grain carbide-doped graphites produced at *CEIT*, and how have been these properties affected by doping.

2.3.2. Influence of dopants on Y_{chem} and Y_{RES} by hydrogen impact

As it has already been seen in sections 1.1 and 2.2, the erosion of carbon materials under hydrogen bombardment leads to large erosion yields and contributes to a high tritium inventory in co-deposited carbon layers [13-15]. It has been already mentioned in the introductory chapter that doping of carbon with small amounts (several at.%) of some elements like B, Si or Ti reduces one or both processes of chemical erosion [16-33]. This reduction is expected to be the more effective the finer and more homogeneously the dopants are distributed in the graphite matrix [29,30].

The effects of dopants on the chemical erosion mechanisms and *RES* of carbon-based materials were summarised by Balden [29]. It is well known that boron doping in graphites strongly reduces Y_{therm} [19,21,126]. Boron dissolves substitutionally in the graphite lattice and enhances the hydrogen release, i.e. the *activation energy for hydrogen release,* E_{Hrel}, is reduced [26] resulting in a reduction of Y_{therm} and a shift of Y_{max} to lower temperatures (see **Fig. 2.5**). But boron strongly degrades the thermal conductivity of graphite due to increased phonon scattering [127]. Therefore, boron-doped graphites are not suitable for their application as *PFM*.

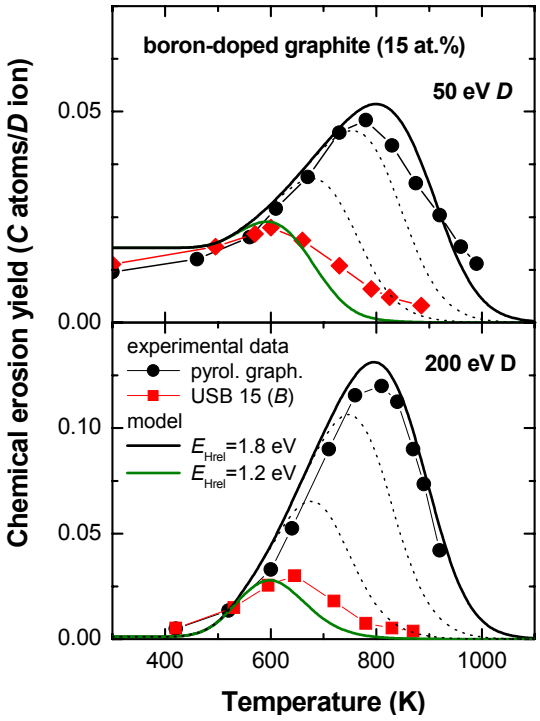

Fig. 2.5. Temperature dependence of the hydrocarbon yield for pure carbon and a 15 at.% *B*-doped graphite (USB 15) [19]. The data are compared with predictions from the analytical model proposed by Roth and García-Rosales [67] for a variation of the *activation energy of hydrogen release*, E_{Hrel} (dotted line: intermediate prediction in steps of 0.2 eV) [27].

Dopant enrichment on the surface due to preferential sputtering of carbon strongly contributes to a reduction of Y_{tot} [24,128,129]. This dopant enrichment increases until reaching a steady state, when a surface layer with a thickness of about the mean dopant particle distance is eroded and the carbides completely shield the carbon surface [24,29].

Y_{RES} has also been reported by Franzen *et al.* to be reduced by doping with boron, silicon and titanium [22], in contrast to the observations of Hino *et al*. [130], who did not observed any reduction of Y_{RES} by doping. Franzen *et al.* generally observed a decrease of Y_{RES} with increasing dopant concentrations, independently of the dopant element but dependent on different graphite orientations, which they could not physically explain. They concluded that Y_{RES} is influenced not only by the dopant element itself, but also by the graphite structural changes due to the doping and manufacturing process.

2.3.3. Influence of dopants on the retention and release of hydrogen

Different authors have investigated the deuterium retention by implantation in different doped graphites [20,94,97,131,132]. It was found that the thermal desorption of molecular hydrogen from implanted boron-doped graphite occurs at temperatures about 150 K lower than for undoped graphites [94], due to an enhanced recombinative release of hydrogen

molecules by boron-doping. It has generally been found a larger retention of implanted deuterium in doped specimens than in undoped graphites [97]. It was suggested that the porosity of the specimens could play an important role in the deuterium retention behaviour of doped graphites, but no clear association between porosity and retention could be found, such that there are still no clear conclusions about the effect of dopants on the deuterium retention behaviour of doped graphites.

2.4. Open questions of main interest

There are still many unanswered questions regarding the influence of dopants on the erosion behaviour by hydrogen bombardment and on the hydrogen retention by implantation. Throughout this thesis, some of these questions will be tackled. They are summarised here in this sub-section. The considerable capabilities of the development of the improved doped graphites produced at *CEIT* to reduce the chemical erosion by hydrogen impact have already been mentioned. But,

- **Question 1:** What is the optimum material with regard to erosion, thermal conductivity and tritium retention?
- **Question 2:** What are the mechanisms responsible for the mitigation of the chemical erosion by doping (which erosion regime is influenced by doping)?
- **Question 3:** Is the erosion behaviour of the doped graphites developed at *CEIT* so promising that these graphites could seriously be a better choice than *CFCs* for their use at the divertor plates in *ITER*?

In order to answer these questions it is necessary to understand the erosion mechanisms of pure carbon and to apply this knowledge to the more complicated case of doped graphites. In this way it is possible to achieve a clarification of the processes involved in the reduction of the erosion yield and to try to optimise them.

3. Experimental

In this work the erosion behaviour and the deuterium retention by implantation of different carbon-based materials under mono-energetic deuterium beam impact are investigated. Different materials were selected for the investigations and several measurements were prepared. This section is dedicated to the description of the two main groups of materials investigated, as well as to the experimental set-up wherein the central experiments were performed (Garching high current ion source). A considerable amount of design, construction and characterisation of the experimental facility and its components were required for some measurements at very low temperatures; those details concerning the modifications of the set-up for the realisation of these measurements will also be shown here. This section also includes brief explanations about the experimental procedure and the different techniques used for the characterisation of the materials after the erosion experiments.

3.1. Materials

The different types of materials investigated throughout the thesis will now be presented. The first important group consists of doped graphites, produced and characterised at the *CEIT*. The second group are thin films, some of which were produced at the University of Greifswald and some at *IPP-Garching*. But why is it necessary to investigate two different groups of carbon-based materials?

On the one hand, it is interesting to investigate the properties of a technically viable material, i.e. a workable material competitive with other plasma-facing candidate materials for its application at the divertor plates. On the other hand, in previous publications it has been proposed that the reduction of the chemical erosion of carbon under hydrogen bombardment by doping is the more effective the finer and more homogeneously dopants are distributed in the graphite matrix [29,30]. So, it could also be very useful for fundamental investigations to be provided with an “ideal” test material, where the dopants

are “ideally” homogeneously distributed, i.e. nano-dispersed and, therefore, where the detectable mitigation of the chemical erosion by doping is expected to be more prominent.

For these reasons two different types of doped materials were selected for their investigation throughout this work: fine-grain carbide-doped graphites as well as nano-dispersed metal-doped carbon films. A third group of undoped carbon materials is also investigated for comparison. **Fig. 3.1** summarises the strategy followed in the fulfilment of this investigation work.

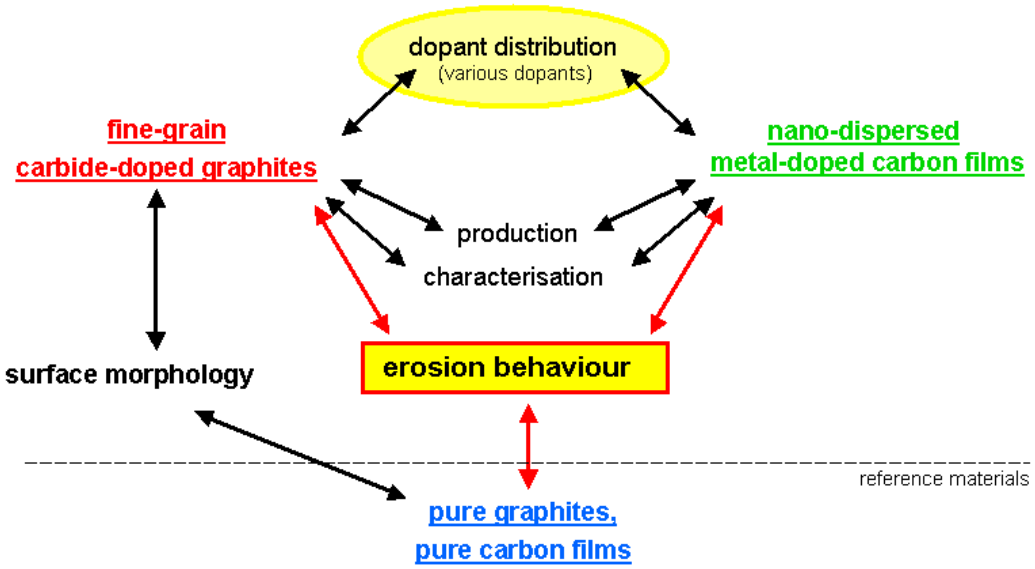

Fig. 3.1. Outline of the strategy followed by the realization of this investigation.

The various doped carbon materials differ from each other in the dopant distribution: fine-grain carbide-doped graphites have the dopants dispersed on a micro-metre scale, whereas the metal-doped carbon films have dopant dispersion on a nanometre scale. Both groups of doped-carbon materials are produced and characterised in the framework of a large project, in which this thesis is included. The erosion behaviour of all materials is characterised and compared with the behaviour shown by the reference materials, pure graphites and pure carbon films. The surface morphology is also investigated after the erosion measurements and compared with the undoped graphite used as reference. The results will be used as input for the production of new doped materials.

3.1.1. Fine-grain carbide-doped graphites

To find the optimum parameters for the manufacture of doped carbon-based materials, the substance used as dopant, as well as the quality and characteristics of doping, especially the amount, size and distribution of dopant, are very important. *CEIT* leads a part of the project in charge of investigating all these parameters for the optimisation of the thermo-mechanical properties of improved doped-carbon materials.

As it was already introduced in the sub-section 1.2, samples of these improved carbide-doped fine-grain graphites have been periodically sent to *IPP-Garching* to characterise, among other properties, the erosion behaviour. It is important to have a global view about their properties, because the erosion behaviour will in some way depend on them. Therefore, it has been judged necessary to summarise in the following from [120,125,133-138], the main properties of the improved doped graphites investigated in this work. To avoid that this section could result too long, more complete information about the manufacturing procedure and the optimisation of some of the parameters involved has been recapitulated in **Appendix C**.

This sub-section informs about the main properties of the improved doped graphites produced at *CEIT*: distribution of dopants, thermal conductivity, catalytic graphitisation by doping, porosity and mechanical properties.

a) Distribution of dopants

The manufacturing process of graphitic materials doped with metal carbides from *meso-carbon micro-beads* (*MCMB*) powder has been optimised at *CEIT* obtaining a homogeneous distribution of the carbides after calcination. Nevertheless, for some dopants and after several graphitisation processes, this homogeneous distribution is lost; in some cases because carbides agglomerate, in others, because the dopants diminish in the outer regions. Therefore, the graphitisation process has been optimised for each blend, choosing adequate values of temperature and residence time for each specific dopant.

Before the erosion experiments, the surfaces of the samples were polished and subsequently cleaned in an ultrasonic bath. Due to the polishing, the dopant grains were depleted in the surface near layer of 1 μm thickness.

b) Thermal conductivity

The *height of the graphitic crystals* (L_C) and the thermal conductivity both can give an idea of the degree of graphitisation achieved, since crystals grow bigger and thermal conductivity increases as the graphitisation process. A higher dwell maintenance time has a very positive effect on the size of the crystals and thus on the thermal conductivity (as it has already been shown sub-section 2.3.1 see **Fig. 2.4**).

However, depending on the temperature of the cycles, a micro structural decay occurs because localised agglomeration of carbides takes place simultaneously, which significantly deteriorates the mechanical properties. Consequently, it is comprehensible that dwell time and graphitisation temperature are essential parameters when optimised doped isotropic graphitic materials have to be obtained.

The thermal conductivity was determined as explained in sub-section C-2 of **Appendix C**. The highest value of it achieved up to now in the work carried out in *CEIT* corresponds to the mesophase of Repsol-YPF doped with *TiC* and graphitised for 2 hours dwell time (see **Fig. 3.2**), with a value of 225 W/mK at *RT*. Comparing it with the maximum one obtained for the graphitised pure mesophase of Repsol-YPF, which is not higher than 45 W/mK (**Fig. 3.2**), a significant improvement of a factor ~5 has been achieved by *Ti*-doping or *TiC*.

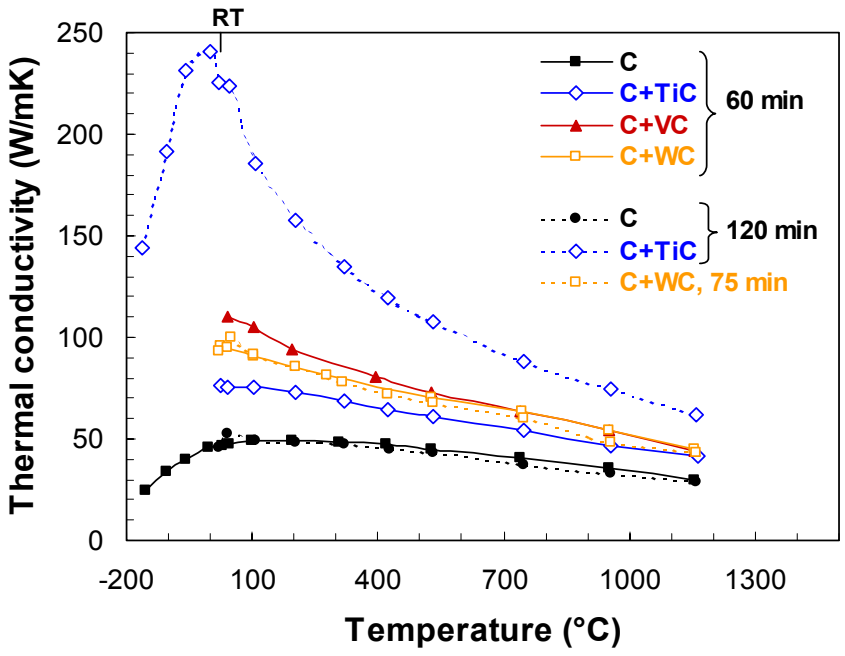

Fig. 3.2. Thermal conductivity as a function of the temperature for some of the last graphitised doped samples produced at *CEIT* (Graphitisation temperature between 2870 and 3020 K) [120]. The dwell times at the maximum temperature are given in minutes.

Furthermore, it is important to bring up here that the thermal conductivity of other commercial graphites [139-141] may go beyond 100 W/mK. This fact reveals that the thermal conductivity of doped graphites is restricted by the graphitisation limit of the initial material. Therefore, changes in the initial characteristics of the graphite precursor might noticeably influence the final thermal properties of the doped graphites. In this way, work is currently been set at *CEIT* on an initial material with a higher graphitisation capacity: a synthetic mesophase supplied by *Mitsubishi*. This material, which is often used in the production of carbon fibres and graphitic foams, has proved to be highly graphitisable. Thus, a further increase of the thermal conductivity of the doped graphites is expected.

Although the current *CFC*s candidates for the divertor of *ITER* have higher thermal conductivity (~350 W/mK [6]), one may be sure that an adequate selection of the initial material and an optimisation of the processing route will allow the development of doped graphites with similar thermal conductivity and thus capable of competing with *CFCs*.

c) Catalytic graphitisation by doping

The temperature at which metal carbides start to catalyse graphitisation is different for each of the carbides and is related to their corresponding eutectic (see **Table C.1** in **Appendix C**). Apparently, the most active dopant seems to be *TiC*, followed by *ZrC*, V_8C_7 and *WC*. On the other hand, V_8C_7 is the catalyser that starts to act at the lowest temperatures, followed by *TiC*. Among the four catalysers considered, the least effective is *WC*, as it doesn't act until very high temperatures and has little influence. In **Appendix B** can be found more details about the catalytic graphitisation by doping (based in the model S-L-S).

d) Porosity

An important effect observed in doped materials is the change in porosity, which turns from open to closed in a relatively narrow temperature range. This change in porosity happens at a different temperature for each carbide, similar to the one at which the carbide starts to catalyse graphitisation. Hence, one intuitively supposes that a close relationship between these two phenomena should exist.

The fact that doped materials bear a completely closed porosity after graphitisation, grants the possibility of achieving a higher densification by *HIP* (*Hot Isostatic Pressure*), needing no capsulation for the samples. By means of this technique, porosity has been

reduced to 50%, no matter how high it was after graphitisation. In this way, the closed porosity of the samples doped with V_8C_7 was reduced from nearly 20% to less than 10%. Analogously, the porosity of samples doped with *WC* decreased from 10% to less than 5%. For the rest of dopants a similar pattern was expected, nevertheless, it didn't emerge, because the samples cracked due to *end-capping*[1].

e) Mechanical properties

Adding dopants to the initial material, not only does not prejudice the mechanical properties, but it considerably improves them in some cases. This is causes by mainly to two facts: the reinforcement effect of carbides in a carbon matrix, and the change in morphology of the porosity.

- The flexural strength increases from 90 MPa for an undoped material to 105-120 MPa after doping.
- The Young's modulus of all materials studied is surprisingly low, especially of graphitic material doped with V_8C_7 (<5 GPa).
- The strain-to-failure is high even though the material is fragile; it varies between 1.3 and 2.16%.

Employing *HIP* after graphitisation strongly changes the flexural strength. Likewise, it has been proved to have no effect on the stiffness of the materials, except for V_8C_7 doped graphite, for which the Young's Modulus decreased markedly down to ~3 GPa. Such a low stiffness turns to beneficial, since it provides the material with a high thermal-shock resistance. In the same way, applying *HIP* does not affect the strain-to failure, except for the materials doped with V_8C_7, where the value rises by approximately 70%. The creation large of carbide clusters and the emergence of regions with heterogeneously distributed carbide, deteriorate the mechanical properties. These micro structural heterogeneities concentrate stress and act as nuclei for fracture, being in most cases more decisive than porosity or impurities.

When these mechanical properties are compared with those of *CFC* candidates for the divertor of *ITER* (flexural strength ~170 MPa, Young's modulus ~70 GPa [142,143]),

[1] The friction between the powder and the piston and matrix walls, as well as a poor filling of powder in the matrix, may induce density gradients during the compression of a green compact, which originate crack formation.

one would expect the materials developed at the *CEIT* to be competitive, once heterogeneities causing fracture in most cases have been eliminated.

3.1.2. Nano-dispersed doped carbon films

As it has already been commented several times, the reduction of the chemical erosion of carbon under hydrogen bombardment by doping is expected to be the more effective, the finer the dopants are and the more homogeneously they are distributed in the graphite matrix [29,30]. The type, amount, size and distribution of dopant seem to be key parameters in finding an improved doped carbon-based material with optimised thermo-mechanical and erosion behaviour.

The prime motivation to begin parallel research to the carbide-doped fine-grain graphites performed at the *CEIT* was indeed the corroboration of this hypothesis: that the smaller the dopant, the higher the reduction of the erosion. Unfortunately, the size of the dopant is not an easy parameter to play around with in the production of fine-grain graphites, since it is limited by the size of the carbide powder used. This powder may be bought in different sizes, but usually no smaller than 1 micron to avoid the precautions needed to manipulate nano-metric powders (health risk if inhaled) as well as higher danger of agglomerating powders, which seriously would complicate the manufacturing process. These unavoidable difficulties dealing with powders turn thin films into a perfect system to study the influence of doping on a nanometre scale.

During manufacture of the improved doped graphites, the amount of dopant is in turn difficult to vary, due to the arduous preparation of the various blends and the complete process. Nano-dispersed doped carbon films stand out as an ideal material to optimise the parameters, such as the amount of dopant and a very fine distribution of it, which are hard to examine systematically.

But another important reason that has encouraged research with these doped films is the interest in the behaviour of mixed layers deposited after erosion. In future fusion devices such as *ITER*, the choice of *PFMs* for high heat flux components is a compromise between material durability, tolerance to peak loading, trapping of *tritium* and plasma poisoning. For that reason, different materials have been chosen for different locations, depending on the relative importance of these effects: *Be*-, *W*- and *C*-based materials (see **Appendix A** for more information). The use of carbon-based materials together with metallic *PFM* will lead to deposition of mixed layers, which will contain carbon and metals

in different ratios. And they could again be re-eroded by hydrogen. Hence, the importance of investigating the chemical erosion behaviour of such mixed layers: on the one hand, to clarify and improve estimations for the re-erosion of mixed layers, and on the other hand, to examine the co-deposition of such mixed layers with hydrogen, for estimations of the tritium inventory.

For all the aforesaid, two different types of doped films have been investigated at two distinct phases of the project: the first ones were produced at the University of Greifswald and were doped *amorphous hydrogenated carbon layers* (doped *a-C:H*); the second ones, more in number and diversity, were prepared for this study at *IPP-Garching*. Those produced at the first stage were used to explore the field; the question was whether an a nano-dispersed dopant would induce a stronger effect on the mechanisms of chemical erosion. After the first measurements, the enormous potential of these doped films to carry out mechanistic studies of the erosion mechanisms was regarded even all the more positively. Then the possibility of producing such thin films at *IPP-Garching* was considered. The idea was to use the magnetron sputtering device to produce different types of doped carbon films, according to the interest of study, to perform a systematic investigation of important parameters, such as amount and type of dopant. Moreover, the use of magnetron sputtering for the deposition of thin films simulates the deposition process that takes place in a fusion plasma environment: in both cases, material arrives at the substrate (wall) mainly as individual atoms. In addition, these films are an ideal test system for diffusion and reaction studies [144,145], as well as to investigate the catalytic effect of some metals on the graphitisation process during the production of doped graphites [35,120,146]

Such nano-structured carbon films also enjoy great popularity in other research fields, because of their excellent tribological properties [147-153]. These carbon films have shown promising properties for a wide range of applications in microelectronics, electrochemistry, catalysis, gas sensing, and hydrogen storage [154].

The first explorations at *IPP-Garching* of producing these films were focused on the specific case of *Ti*-doped carbon films, on which there was already some knowledge coming from Greifswald [155]. The investigation was systematised and amplified to a wider range of dopants (*W*, *V*, *Zr*, *Cu* and *Cr*) in a Diploma Thesis closely linked to this work and recently finished [38].

Production

Although both types of thin films were produced by magnetron sputtering, the difference between them lies in the hydrogenated *Greifswald* films in contrast to the non-hydrogenated *IPP-Garching* films. No meaningful differences have been estimated as far as erosion behaviour is concerned because the ion bombardment during the erosion measurements hydrogenates the films to the same amount.

Various *Ti*- and *Mo*-doped *a-C:H* films were produced in a co-operation with the University of Greifswald. The metal-doped films were deposited by means of chemical-assisted magnetron sputtering [155] on silicon wafers as substrate. The doping material was sputtered in a reactive gas atmosphere consisting of a mixture of argon and methane. Methane contributes as carbon source to the layer growth, while the sputtered dopant atoms are expected to be homogeneously dispersed in the film on a nanometre level.

In a next step, pure *a-C* and *Ti*-doped *a-C* films were also prepared by magnetron sputtering but this time at the *IPP-Garching* device. In a second production phase, new *W*-, *V*-, *Zr*-, *Cu*- and *Cr*-doped *a-C* films were systematically produced and characterised [38]. Due to the imminent connection between the structure of the films and their erosion behaviour, a brief description of the production technique used for the manufacture of these films has been included in the following together with a review of their main properties, which have been summarised from [38].

The magnetron sputtering device

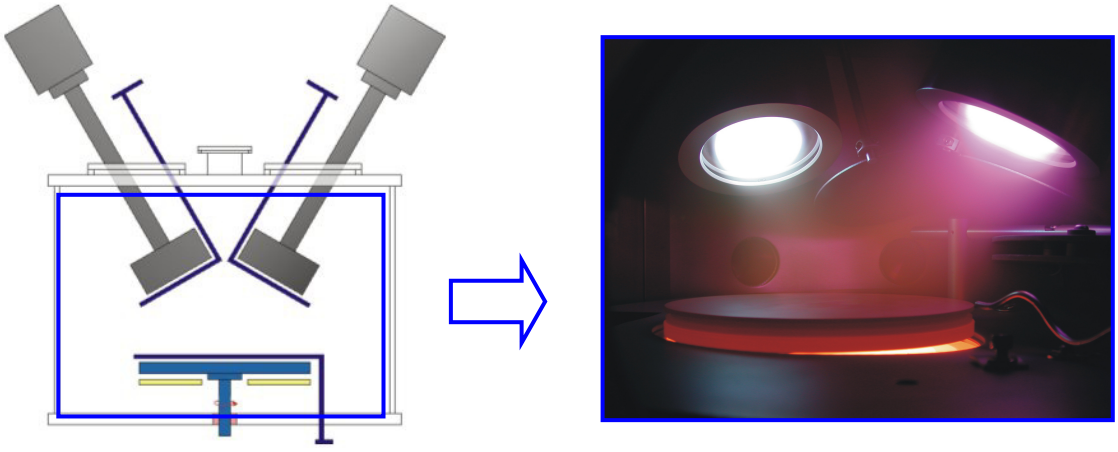

Fig. 3.3. On the left, schematic of the Denton Vacuum Discovery-18 Deposition System, with the confocal arrangement used for the cathodes. The distance between the substrate and the target was adjusted to 120 mm from the centre of the target to the centre of the deposition table. On the right, photo of the inside of the chamber during a sputter deposition process.

The specific magnetron sputtering device used for the production at of the second group of metal-doped films at *IPP-Garching* was a Denton Vacuum Discovery-18 Deposition System, for which a schematic is shown in **Fig. 3.3**.

The device is designed for thin film production in research. Its configuration provides easy access to substrates, sources, and instrumentation while maintaining excellent pumping characteristics. The system's inherent flexibility allows for the operation of two sputter sources and the ability to heat, *RF* bias, and rotate the substrate.

Metal and graphite were used as targets. Their surfaces have to be smooth with no sharp points that could result in localised arcing. The metal targets had purities of 99.99%, whereas those of the non-metals are generally less, with a typical upper purity limit of 99.9%. As sputtering gas, argon (99.9999%) was applied. The doped carbon films were deposited on silicon and graphite substrates using two types of discharges: *DC* for the metal cathode and *RF* for the graphite cathode. By controlling the argon flux, a deposition pressure of 0.45 Pa was maintained. The specimen holder was rotated during the deposition process. The substrate holder was neither biased nor intentionally heated. The sputter rates for both targets were investigated in detail using a crystal oscillator - Quartz Thickness Monitor QSG050 (display resolution: 0.1 nm, operating frequency: 6 MHz). In order to obtain the intended dopant content in the films (0-20 at.%) the *DC* power was modified. The lowest concentrations of dopant (<2 at.%) were by far the most complicated to achieve. The deposition rate of carbon limited the growth rate of the film to about 3 nm/s. More details about deposition properties can be found in [38].

Characterisation and quality of the thin films

This sub-section contains important information about the composition and distribution of dopants in the nano-dispersed doped carbon films, and also about their morphology and internal structure. At the end, the conclusions of an investigation of their thermal stability will be presented.

a) Composition and thickness

➔ Metal-doped a-C:H films produced in Greifswald

The averaged film composition and thickness of the first group of doped films produced in Greifswald (metal-doped *a-C:H* layers) were determined by *ion beam analysis*

(*IBA*). Backscattering of 1.5 MeV *protons* (H^+) at a scattering angle of 165° and elastic recoil detection using 2.6 MeV ^{4}*He* were used to determine the carbon, oxygen and dopant amount (*Ti* and *Mo*) and the hydrogen content, respectively. Only four of these films were selected for erosion investigations, due to their acceptable content of impurities. The averaged concentrations of dopants in these films are in the wide range of 6 to 50 at.%, and the hydrogen content is neglected in the concentration calculations (because the films will be further bombarded by deuterium): 2 films with 10 at.% *Ti* and 3 and 5 at.% *O*, respectively; one film with 13 at.% *Ti* and 6 at.% *O*, and one film more with 50 at.% *Mo* and without any detectable *O*.

➔ Metal-doped a-C films produced at IPP-Garching

Employing the measured deposition rates as a formation of discharge power, it was possible to control the dopant concentration within 5% of the nominal value.

As it has already been mentioned, the majority of the films were produced to subsequently carry out erosion experiments. So, they were systematically fabricated for this aim, in order to investigate the influence of:

- Type of dopant: *Ti*-, *W*-, *V*-, *Zr*-, *Cu*- and *Cr*-doped *a-C* films were deposited.
- Amount of dopant: thin films were produced with similar concentrations for each dopant, in order to allow comparison between them: high (~15 at.%), medium (~8 at.%) and low (the lowest possible) concentration of dopant. Higher concentrations of dopants have been avoided in order to keep the properties of *a-C* films (and not to produce carbide thin films).

Depth profiles and film thickness were both determined by *Rutherford Backscattering Spectrometry* (*RBS*) of 0.8 and 4 MeV ^{4}*He* at a scattering angle of 165°, and cross-checked by *XPS*. The thickness of the films varies between ~300 and ~1800 nm, but most of them are usually 400 and 1000 nm.

The films contained *O* and *Ar* impurities in an amount of always less than about 4 at.% and 1.5 at.%, respectively. Before carrying out the majority of the erosion measurements, the samples were degassed at ~1200 K for about 15 minutes. After that treatment, *Ar* practically disappeared (at.% *Ar* <0.6).

b) Distribution of dopants

The depth distribution of dopants of the films produced at *IPP-Garching* was also investigated by *RBS*. Backscattering of 800 keV ^{4}*He* ions was performed at a scattering angle of 165º. This relatively low energy maximises the achievable depth resolution of the spectrum. Depending on the elements, individual spectra might even overlap, but here the higher depth resolution is more important. Using this technique, in some of the films a heterogeneous distribution of the dopant was found, but always at about ¾ of the film thickness, i.e. within the first 100-250 nm to the interface. The rest of the films were homogeneous, and this homogeneity was always better than ~1 at.% across the depths of interest for the erosion experiments (<100 nm).

The lateral distribution of dopant and the morphology of the films produced at *IPP-Garching* were investigated by *Scanning Electron Microscopy* (*SEM*). A structure was always observed, even in the films deposited on silicon. The structure looks like small spheres with approximately the same length scale for all the elements and compositions studied: a lateral expansion of ~25 nm and a height of definitely less than 10 nm in thickness of several hundred nanometres. Additionally, the spherical structure was enlarged by up to one order of magnitude when the substrate had been rough or smooth.

c) Internal structure

Although the structure of the films after deposition was expected to be amorphous, investigations by *X-ray diffraction* (*XRD*) were done to clarify whether the energy with which the sputtered particles were deposited might induce the creation of any crystalline structure on the nanometre scale. The identification of the diffraction curves was accomplished using the database JCPDS-ICDD.

Only in the *W*- and *Cu*-doped carbon films small crystallites (at least of ~2 nm) could be identified just after production. In the other films, the very probable presence of similar nano-crystals could not be confirmed by *XRD*, perhaps not implicitly due to a small size of the crystals, but due to a more disordered structure of them, which would lead to wider and smaller diffraction peaks.

However, for the specific case of *Ti*-doping, already reported *XPS* studies [156] indicate that *Ti* atoms react to *TiC* in the mixture already at *RT*. The presence of possible nano-crystals in *Ti*-doped carbon films was further explored by *Transmission El*ectron *Microscopy* (*TEM*).

Fig. 3.4 shows two *TEM* images, which corroborate the presence of nano-crystallites. An electron diffraction pattern solved for one of the crystallites confirms the formation of *TiC* nano-crystals after the production of this film.

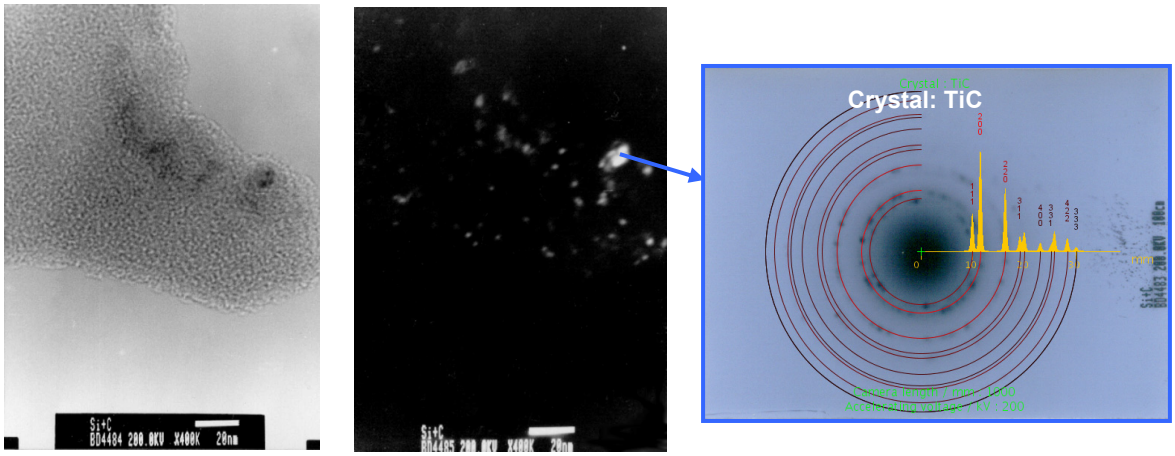

Fig. 3.4. On the left, a *TEM* image of a *Ti*-doped carbon film after deposition shows small nano-crystallites with dark contrast. They can be better distinguished in the centred *TEM* image, where they are shining on a dark field. The picture on the right shows an already solved electron diffraction pattern of one of the small nano-crystallites, which corresponds to a *TiC* crystal.

d) Thermal stability

As it was already pointed out, before carrying out most of the erosion measurements, the samples were degassed at temperatures up to ~1200 K for about 15 minutes. For this reason, it is important to know whether the films are stable or not during such a heat treatment.

Films heated under the above mentioned conditions were investigated by *RBS* with 4 MeV ^{4}*He*, and the spectra obtained before and after heating were compared. *Ti*-, *W*-, *V*- and *Zr*-doped carbon films showed absolutely no change, i.e. no diffusion process was observable.

Investigations of the same heated films by *XRD* showed, however, significantly higher intensities and the emergence of new peaks, which were correlated to carbides in almost all the films (except for *Cu*). This fact could correspond to some changes in the crystal structure, such as growth of crystallites, formation of nano-clusters or even of new crystallites. An estimation of the sizes of the crystallites after degassing always yielded the range of ~10 nm, except for the *Cu*- and *Cr*-doped films, for which clustering was observed by *SEM* and *RBS*, destroying the desired properties of the films; clusters of >60 nm and 15 nm were detected by *XRD*, respectively. Due to this micro-structural changes by heating, these films were rejected for chemical erosion experiments.

3.1.3. Reference materials: pure carbon

The erosion behaviour of the investigated doped materials is always compared with the behaviour shown by a well-known pure carbon material. For this work, four different kinds of undoped materials have been used as reference for the comparisons:

- HPG is a pyrolytic graphite from *Union Carbide* (*UC*, USA), polycrystalline, with a mosaic spread of ±11º cut parallel to the main graphitic basal plane (see **Fig. 3.5**). It has nearly no porosity and its high density (2.24 g/cm^3) is very closed to the one of an ideal graphite (~2.2 g/cm^3). The size of its crystallites can reach several microns.
- EK98 is an isotropic fine-grain graphite from SGL Carbon (Germany) with grains as big as 25 µm diameter, which consist of smaller disordered crystallites of sizes between 10 and 100 nm. The much porosity, which separates the grains, leads to a low density (1.85 g/cm^3).

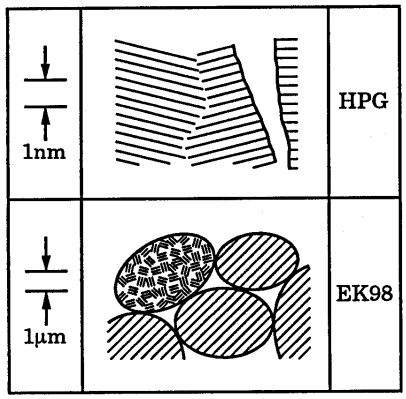

Fig. 3.5. Schematic illustration of the structures of the pyrolytic graphite HPG and the polycrystalline graphite EK98. A different length scale of the microstructure can be observed. [115,139,140].

- Undoped fine-grain graphite from *CEIT* is also an isotropic material with a microstructure very similar to EK98; the small crystallites are of a size of about 15 nm. Almost all porosity is of the open type (~12-15%).
- Pure amorphous carbon films were also produced at *IPP-Garching* by means of magnetron sputtering, in the same way as the doped carbon films. Their disordered structure and morphology, similar to that of the doped carbon films, have already been described in sub-section 3.1.2.

3.1.4. Denotation of samples investigated

Name	Short description	Density (g/cm^3)	Bulk composition (at.%)	Depletion film thickness* (μm)	Main grain size of dopant (μm)	Producer
HPG	Pyrolytic graphite with mosaic spread of ±11° cut parallel to the main basal plane orientation (Grade HPG)	~2.2	Non	—	—	*UC*, USA
EK98	Fine-grain graphite	1.86	Non	—	—	*SGL* Carbon AG, Germany
R6650M	Fine-grain graphite	1.85	Non	—	—	*SGL* Carbon AG, Germany
C_{CEIT}	Graphitised by heating of *MCMB*	~1.9	Non	—	—	*CEIT*, San Sebastian, Spain [122]
TiC2 TiC4 VC4 WC4 WC4in WC19 ZrC4	Graphitised by heating of *MCMB* mixed with carbide powder (*TiC*, V_8C_7, *WC*, *ZrC*)	— ~2.1 ~2.0 ~2.9 ~2.9 ~2.9 ~2.3	2 at.% *Ti* 4 at.% *Ti* 4 at.% *V* 4 at.% *W* 4 at.% *W* 4 at.% *W* 4 at.% *Zr*	 0.7 1 2 2 0.6	~1 ~1 0.9-1.3 ~0.7 ~0.7** 0.9-1.3 ~1	*CEIT*, San Sebastian, Spain [122]
RGTi91	Uniaxial pressing of a mixture of graphite and Ti powders and re-crystallisation with *TiC* formation	2.23	2 at.% *Ti*	—	~2-5	Composite, Moscow, Russia via Efremov Institute, St. Petersburg, Russia [20]
LT10	Isostatically pressed graphite and *TiC* powder mixture	2.79	10 at.% *Ti*	-—	~2-5	*CERAM*, France
C/SiC	2D carbon fibre architecture with *SiC* matrix	—	~20 at.% *Si*	—	—	*MAN* Technologie AG, Germany

Table 3.1. Denotation of samples and some properties of them. (*The dopant is depleted in the surface; **with large *WC* grain clusters, i.e. strongly inhomogeneous dopant distribution).

name	dopant	graphitisation temperature (K)	carbide grain size (µm)	bulk conc. (at.%)	surf. conc. (at.%)	Density (g/cm³)	porosity (%)		L_c (nm)	thermal conductivity (W/mK)		D_2/CD_4 ratio	
							Total	Closed		@ 300 K	@1220 K	medium fluence	high fluence
Ti2350	*TiC*	2620	~1	4.5	3.4	2.13	13.0	4.5	16.9	37	34	4.3	5.4
Ti2750		3020		5.3	1.7	2.04	14.1	13.4	38.9	167	66	5.0	7.0
V2350	*VC*	2620	1.5-2	4.5	2.8	1.99	20.7	8.8	15.3	49	39	5.6	7.9
V2750		3020		4.3	2.8	1.96	19.1	16.3	31.7	103	52	3.3	4.3
W2350	*WC*	2620	~0.7	3.5	1.5	2.95	12.9	5.0	17.7	~26	~25	~4	10.7
W2750		3020		3.5	1.8	2.80	16.3	14.1	24.4	~92	~50	3.6	5.1
Zr2350	*ZrC*	2620	~1	3.6	2.3	2.26	15.7	3.9	17.0	28	27	4.6	5.2
Zr2750		3020		3.5	1.9	2.27	15.9	15.4	72.6	185	67	4.4	5.1
CCalc	undoped	1270	—	—	—	1.65	19.5	1.4	-	<27	<28	4.0	4.5
C2100		2370	—	—	—	1.91	-	-	15.9*	35	29	3.0	3.8
C2350		2620	—	—	—	1.92	11.0	2.0	16.6	30	27	3.3	4.1
C2750		3020	—	—	—	1.94	12.0	0.3	18.9	62	41	3.3	4.0
HPG	pyrolytic graphite	Union Carbide, USA	—	—	—	~2.2	4.3	4.3	34.4	—	—	3.3	4.5

Table 3.2. Summary of some properties of the specimens studied for the temperature dependence and the *TDS* experiments. L_c is the crystallite size perpendicular to the graphite basal planes (* graphitisation temperature 2470 K). Mean value of the D_2 to CD_4 ratio for the medium fluences (2-500×10^{21} D/m^2) and for the highest fluences (>500×10^{21} D/m^2).

3.2. Erosion and implantation measurements by mono-energetic deuterium beam impact

In a real fusion device, several species simultaneously interact with the *PFMs*: energetic and thermal fuel ions, neutrals, helium ash, Franck-Condon atoms, neutrons and electrons. All these particles together will have an influence on the net erosion of the *PFMs*. In addition, the simultaneous impact of some of these species together could lead to higher erosion yields than the simple linear sum of the yields due to each species acting separately, for example simultaneous ion-neutral impact [43,64,77,78,113,157-160]. So synergistic effects also have to be investigated. Although such a complicated environment can only be reproduced in a real experimental tokamak, this has the serious inconvenience that it is nearly impossible to separate the contributions of individual species for the identification of the main reaction processes. Thus, experiments such as plasma generators or ion beam accelerators are ideal equipments to study the erosion of a *PFM* by single or limited multi-species impact.

Among all species mentioned above, the hydrogenic fuel ions are of special concern due to their high reactivity. They are expected to arrive at the divertor plates of *ITER* with energies of a few tens of eVs. As it has often been remarked, the use of carbon in such places of the *ITER* divertor seems to be indispensable to survive the expected transient thermal loads, which could reach 20 MW/m^2. So laboratory simulations of the reactions between hydrogen and carbon seem essential to predict extremely critical parameters, e.g. the lifetime of the components or the tritium inventory, especially at low energy ion impact.

In this work, most of the measurements were performed at a laboratory experiment used to separately simulate the impact of various light ions on *PFMs*: the Garching high current ion source [46]. Therefore, this sub-section starts with a description of the main components of the set-up.

After that, the procedure followed during the measurements will be described. First of all and before a set of measurements can be taken, the ion beam profile has to be characterised. Directly after characterising the beam, the experiments may commence. They are basically divided into 3 groups: fluence dependence measurements, temperature dependence measurements and *TDS* measurements. The first two groups of measurements search for the influence of dopants on the erosion mechanisms of carbon by deuterium impact, and the last one explores the influence of dopants on the deuterium

retention by implantation. The ion current and ion density were always controlled during the measurements. Both the total and chemical erosion yields were determined by weight loss measurements and by erosion products analysis using *QMS*, respectively.

3.2.1. The device: Garching high current ion source

The Garching high current ion source can be adjusted to produce mono-energetic mass-separated ion beams of light ions, like *H*, *He*, *O* and *C* with energies between 20 eV and 8 keV.

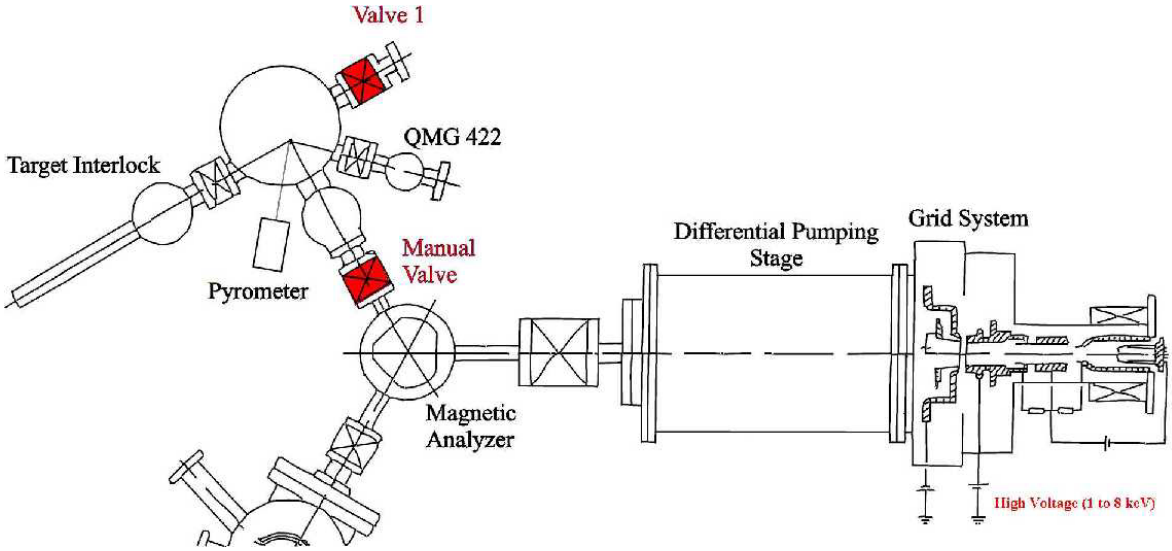

Fig. 3.6. Sketch of the Garching high current ion source for light ions.

A sketch of the device is shown in **Fig. 3.6**. The main components of the system are the ion source, the differential pumping stages, the magnetic analyser for mass separation and the target chamber, in which most of the measurements were performed.

Components of the set-up

a) Ion source

As ion source a high current injector of the Oak Ridge type is used. When a current of about 18 A powers the water-cooled cathode, it abundantly emits electrons, which ionise the inflowing deuterium gas. Subsequently, the ions are extracted and accelerated by a high voltage and afterwards focussed inside the grid system.

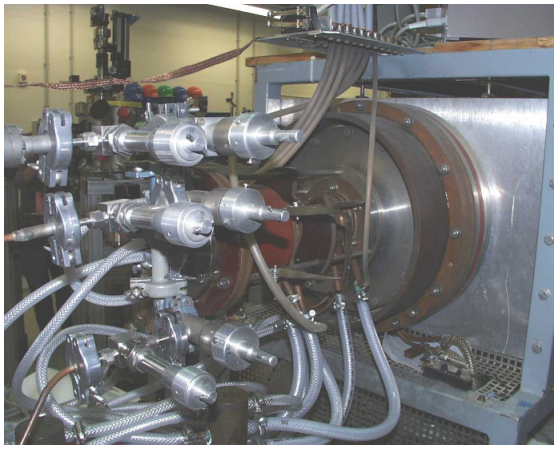

Fig. 3.7. Image of the ion source with the gas inlets. Up to three gases can simultaneously be used at the cathode to produce the plasma.

b) Differential pumping stages

Differential pumping stages equipped with turbo-molecular pumps (TURBOVAC 1000 C, 850 l/s for N_2) are installed between the grid system and the magnetic analyser (see **Fig. 3.6**) to prevent excessive neutralisation of the beam as well as to maintain a low partial pressure of the working gas in the target chamber. The pressure in this differential pumping stage is about 1×10^{-3} Pa.

c) Magnetic analyser

The important role of the magnetic analyser consists of selecting ions, which have a specific mass, depending on the electric field matched on it. It allows only the ions with a specific radius of curvature imparted by the $E\times B$ force to reach the target chamber.

The mass selection is determined by the following equation:

$$\frac{m}{e} = \frac{\left(2UB^2\right)}{E^2} \tag{3.1}$$

were m and e are the mass and the electric charge of the ion, respectively, B is the magnetic field, E is the electric field and U the ion energy.

d) Target chamber

The target chamber is evacuated with a turbo-molecular pump (500 l/s for N_2) reaching pressures better than $\sim10^{-6}$ Pa. During bombardment, the pressure increases to

$\sim 10^{-4}$ Pa. A liquid nitrogen-cooled copper trap allows to strongly reduce water as residual gas and improves the vacuum conditions to $\sim 10^{-5}$ Pa.

During this work, for the investigation of the chemical erosion processes of doped carbon materials under low and high deuterium impact energies, the source was employed to generate 30 eV and 1 keV deuterium ion beams, respectively. Due to the fact that the current density rapidly decreases at extraction voltages below 3 kV, causing inappropriately long irradiation times, the ion beam was extracted from the ion source with high voltage, after that magnetically analysed and subsequently decelerated. The deceleration can directly be carried out in front of the target by a positive target bias in order to obtain the desired final impact energy of the beam into the target.

Before impinging on the target, the ion beam has to pass through two apertures; from those the last one determines the size and shape of the spot. To obtain an accurate ion current measurement, a Faraday cup consisting on a double cylinder arrangement surrounds the target, collecting the secondary electrons produced by the impact of the ions on the target and reducing the dispersion of the beam. The outer cylinder is biased at –50 V with respect to the target potential in order to prevent the entrance into the chamber of the secondary electrons produced by the beam at the apertures. The inner cylinder is at ground potential (the deceleration is in fact done between inner cylinder and target).

In order to obtain a mono-energetic deuterium beam, molecular ions D_3^+, instead of D^+, were in general used for further increasing the current density. For example, in order to obtain a 1 keV deuterium ion beam, the bombardment was performed with 6 keV molecular ions D_3^+, which were decelerated to 3 keV. For these light ions, no overlapping collisions occur, and the sputtering yield is equal for atomic and molecular ions, such that after the splitting of D_3^+, the ion beam results to be equivalent to 3 times a D^+ ion beam of 1 KeV. The energy with which the majority of the erosion experiments were performed was 90 eV D_3^+ (i.e. 30 eV D). The usual deuterium fluxes were around 10^{19} D/m^2 s.

At low energies, where the sputtering yield of some light ions decreases strongly, the fraction of neutral particles in the beam has to be controlled. These neutrals are not decelerated by the target bias and reach the target with the full extraction energy, such that they might contribute to the total erosion with an important fraction. In a previous recent study [59] the amount of neutrals of a deuterium beam extracted with 1 kV (3 keV) was determined by measuring the weight loss of a gold target bombarded with 60 eV deuterium (180 eV D_3^+) impact energy. This energy is below the threshold energy for physical sputtering, which is for gold the only existing erosion process by deuterium bombardment [46]. Therefore, the measured weight loss was assigned to the physical

sputtering of the neutral deuterium atoms of 1 keV, and the fraction of neutrals was determined to be about 3%.

e) Microbalance

The target chamber is equipped with a Mettler ME21 vacuum-microbalance, which allows to weigh the target in-situ with a sensitivity of $\pm$ 1μg. When the target is hung on it, a beam is deflected and the magnitude of the developed deflection at the weighting produces a proportional current. Besides, the current produces a magnetic counteracting force that keeps the beam on zero deflection.

f) Target holder

The target holder has not only the function of holding up the target, but it also has to easily allow the carrying of the sample to the target interlock chamber, as well as to the microbalance. For these reasons, the target holder has a special design, as **Fig. 3.8** illustrates. It is entirely made of Molybdenum for resisting high temperatures and avoiding possible interactions with the ion beam and the residual gas.

The target cup is connected to an electronic integrator, which collects the charge passing through it, such that a direct measurement of the current flowing through the target is possible. The interface of the *quadrupole mass spectrometer* (*QMS*) has been used for monitoring and recording this current.

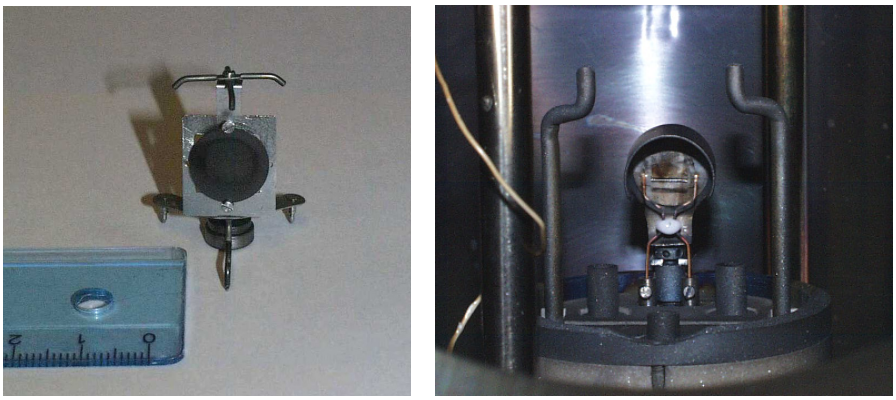

Fig. 3.8. On the left, target holder with a graphite sample mounted on it. The masses at the bottom are tare masses used for the weight loss measurements. On the right, a detail of the target system without the target holder showing the tungsten filament used as electron emitter for heating.

g) Target heating

A tungsten filament directly positioned behind the target allows heating by electron bombardment from the rear (see **Fig. 3.8** on the right). The electrons emitted are accelerated to the target by the same mentioned bias voltage that decelerates the ion beam (up to 3 keV). This configuration has the advantage that most of the electrons reach the target, and not the chamber walls. The magnitude of the current that flows through the filament determines the amount of electrons emitted; thus, by controlling this current (either manually or automatically by a computer), different temperatures are achievable (up to ~1450 K). This kind of heating is very efficient and allows a nearly uniform heating of the target.

h) Quadrupole mass spectrometer (QMS)

Separated from the vacuum target chamber by an aperture located at 45º to the normal of the target surface a *QMS* from the company Balzers, model QMG 422 with a crossbeam ion source is located for the analysis of the reaction products during ion bombardment and *TDS* measurement.

The QMG 422 is independently pumped by a turbo-molecular pump (TURBOVAC 361, 345 l/s for N_2) and surrounded by a liquid nitrogen-cooled copper shield to improve its vacuum conditions.

A *QMS* is “an instrument in which ions are produced from a sample, separated according to their mass to charge ratios, and recorded” [161]. When the residual gas of the vacuum chamber reaches the *QMS*, its atoms or molecules are ionised by electron bombardment at a certain energy depending on the voltage of the cathode. After that, the ions are accelerated and separated by electric fields in accordance with their mass/charge ratio, and finally they are electrically detected and recorded in a computer. A secondary electron multiplier allows amplifying the ion currents with gains from 10^4 to 10^8. **Fig. 3.9** shows the separating principle of the *QMS*, with 4 hyperbolic rod electrodes at a voltage composed of a high-frequency alternating component $V \cos \omega t$ and a superposed direct voltage U. ω determines the mass to be detected.

The interpretation of the mass spectra has to be done with care, because cracking of heavier molecules due to the ionisation process can contribute to other lighter masses. Another problem is that different species with same weight could concurrently be present, making complicated the quantification of the contribution of each one to this mass.

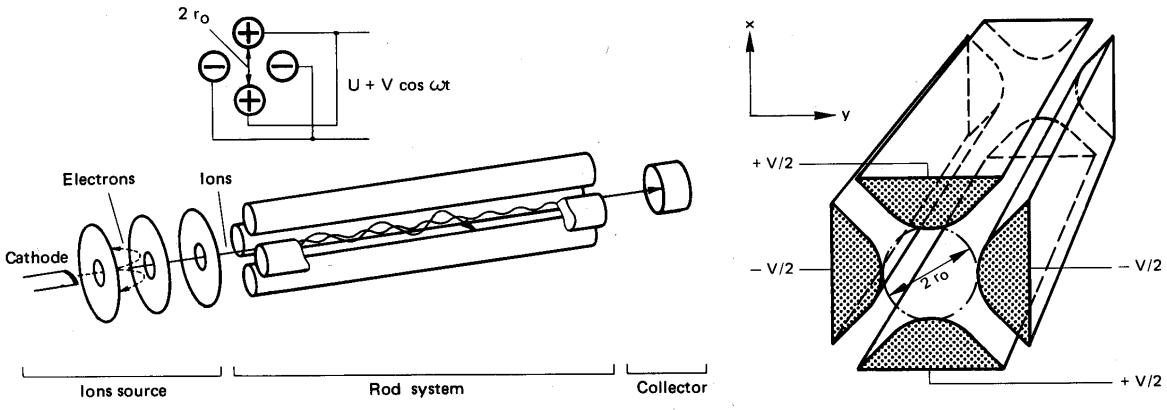

Fig. 3.9. On the left, structure of a quadrupole analyser. On the right, principle of the quadrupole mass filter: field-generating potentials [162].

Table 3.3 summarises the parameters of the QMG 422 used for the *TDS* and erosion measurements.

Analyser parameters		
Detector type	Secondary electron multiplier	
Resolution	20	
Ion source parameters	**TDS exp.**	**Erosion exp.**
Emission current	1 mA	1 mA
Emission protection	4.4 A	4 A
Ion ref.	100 V	100 V
Cathode	80 eV	70 eV
Focus	8 V	8 V
Field axis	10 V	5.5 V
Extraction	200 V	120 V
Deflection	250 V	250 V

Table 3.3 *QMS* optimised parameters used for the *TDS* and erosion experiments.

i) Temperature measurement

An infrared pyrometer MAUER TMSR 95/105 is located outside the target chamber and directed to the target surface through a magnesium fluoride (MgF_2) window with an angle of 45º to the normal of the target.

The instrument is a radiation thermometer, which contains a sensor that converts thermal radiation received through some type of optics into an electrical signal. Optical filters allow only a selected wavelength (within a narrow band) to reach the sensor.

The infrared pyrometer was used for monitoring the temperature of the target during the erosion experiments. Before starting measuring, the calibration of the infrared pyrometer was performed at the same time as the target was degassed at ~1200 K. For this calibration, an optical pyrometer, which operates at temperatures up to 973 K, was used. The temperature of the target was measured with the optical pyrometer and the temperature of the infrared pyrometer was crosschecked such that it was the same in both instruments.

The pyrometer has 2 measurement ranges: low temperature range (323-773 K) and high temperature range (673-1273 K). For each one, the voltage can be decoded into a temperature by the following linear equations:

$$T\,[K] = 44.753 \cdot V\,[Volts] + 49.176 + 273.15, \text{ for } T = 323 \text{ to } 773\ K \qquad (3.2)$$

$$T\,[K] = 60.129 \cdot V\,[Volts] + 401.20 + 273.15, \text{ for } T = 673 \text{ to } 1273\ K \qquad (3.3)$$

Temperatures above 1273 K were measured with the optical pyrometer and linearly extrapolated from equation 3.3.

Modifications of the set-up for the measurements below room temperature

a) Cooling system

For a better understanding of the involved mechanisms on the mitigation of chemical erosion by doping, measurements with 30 eV deuterium beam below *RT* were required. For this purpose, the set-up had to be modified in the course of about five months. The main changes of the adjusted set-up are schematically illustrated in **Fig. 3.10**.

A new cooling system that used nitrogen gas as refrigerant was constructed. The gas flowed with a certain pressure through a spiral tube made of copper, which was immersed into liquid nitrogen. While passing through the pipe, the nitrogen gas cooled down and subsequently was pressed through the target holder.

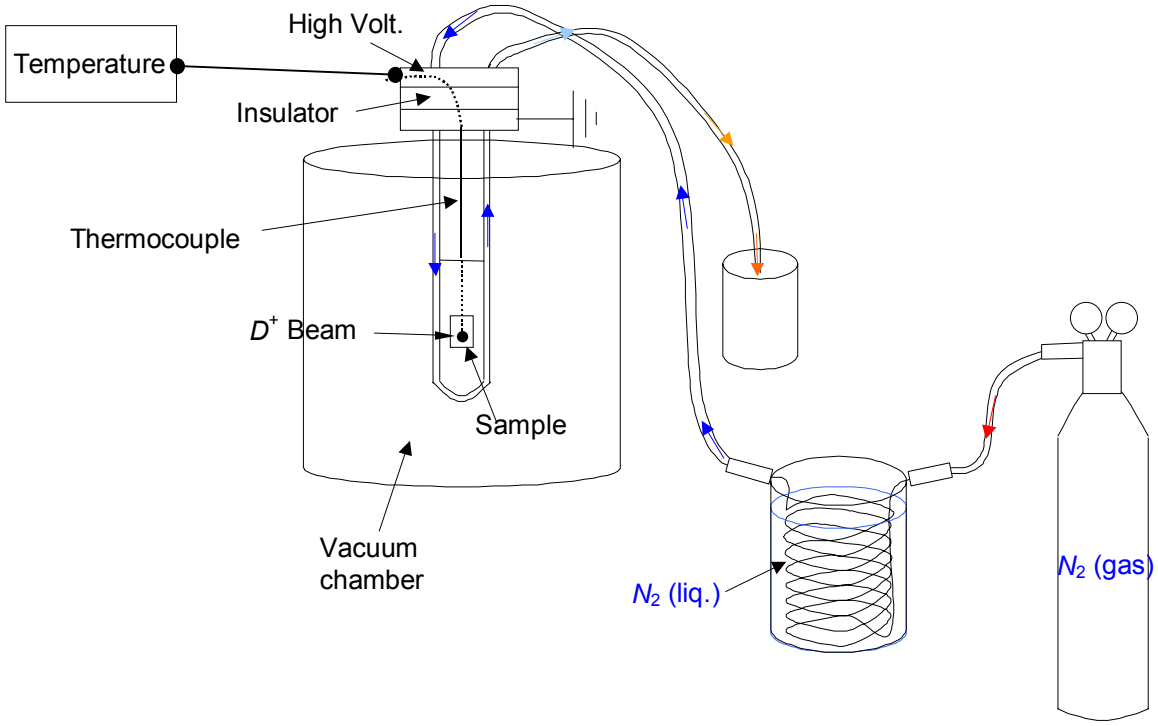

Fig. 3.10. Schematic of the cooling system attached to the target holder used for the chemical erosion measurements below *RT* under 30 eV deuterium bombardment.

b) Target holder

A target holder of copper equipped with a tube for the cooling medium was connected to the new cooling system and assembled into the vacuum chamber. The sample was mounted fixed onto this holder, such that the only way to change the target was venting the chamber.

High voltage (3 kV) had to be directly applied to the target holder for deceleration the ion beam. For design reasons, the required insulation for such a high voltage had to be installed outside of the vacuum chamber. Therefore water condensation and even ice formation on it was unavoidable, and a lot of work was carried out in order to assure the essential security.

Details about the configuration of the target holder are illustrated in **Fig. 3.11**.

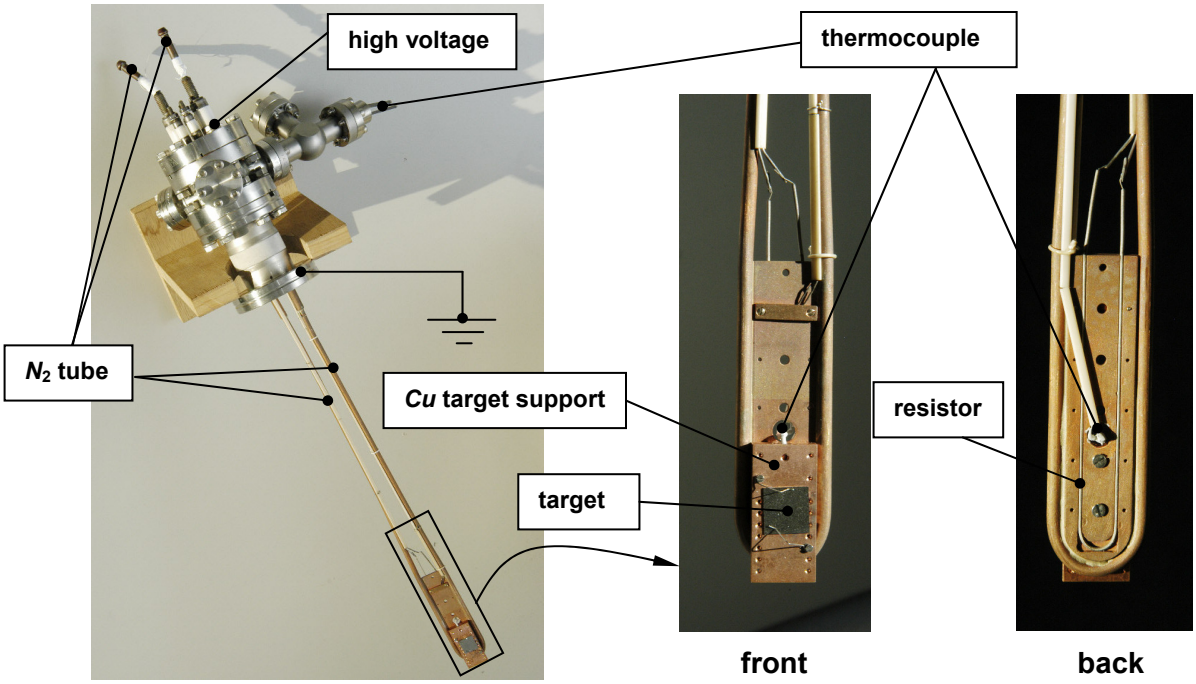

Fig. 3.11. Images of the target holder used for the measurements below *RT* and its equipment.

c) Target heating and temperature measurement

The target holder had a resistor (see **Fig. 3.10**), which allowed ohmic heating of the target up to 410 K. The samples were always degassed before the erosion experiments at the maximum available temperature for dwell times above 1 hour.

The resistor also permitted reaching intermediate temperatures between ~77 and 270 K, without which they would have been unfeasible. These temperatures were achieved by controlling the pressure of the refrigerant gas together with simultaneous heating.

A thermocouple type K (*Ni-Cr* vs. *Ni-Al*) was installed onto the target holder for directly monitoring the temperature during the experiments.

3.2.2. Determination of the ion beam profile

An investigation of the ion beam profile is critical for the determination of the flux distribution of deuterium on the bombarded samples and the spot size. For that reason, it has always been characterised before starting a measurement campaign.

To do this, samples of an a*morphous hydrogenated carbon film* (*a-C:H*) of about 340 nm deposited on a silicon wafer were eroded under different deuterium fluxes with normal incidence bombardment. The samples were very homogeneous due to the well-controlled deposition process made *at IPP-Garching* and the perfect flat surface of the wafer.

The obtained erosion profile is correlated with the spatial flux variation of deuterium (as long as there is normal incidence bombardment, because erosion can strongly depend on angle [46]). The reaction between deuterium ions and a thin *a-C:H* film can give an erosion depth on the order of magnitude of visible light wavelength, depending on the quantity of ions used. Fluences were selected for this purpose, and a first qualitative analysis could rapidly be done by simple visual examination. As an example of this, **Fig. 3.12** shows one of the eroded *a-C:H* layers used for the characterisation of the spot size and flux dependence under 90 eV D_3^+ deuterium impact, with an extraction voltage of 3.09 kV, deceleration voltage of 3 kV, and aperture of 6×3 mm^2.

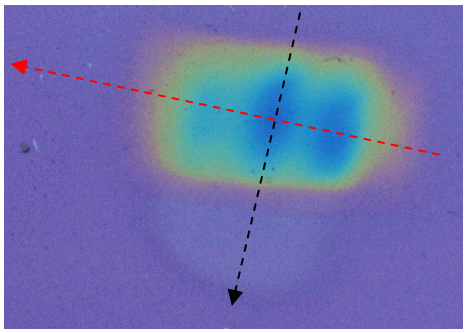

Fig. 3.12. Image of an *a-C:H* film (A17) deposited on a *Si* wafer after bombardment at *RT* with 90 eV D_3^+ (3.09-3 keV) and an aperture of 6×3 mm^2. The coloured erosion spot is produced by the reaction of the D_3^+ ions with the thin film, whereas the imprecise one on the bottom by the high energetic neutrals (not decelerated).

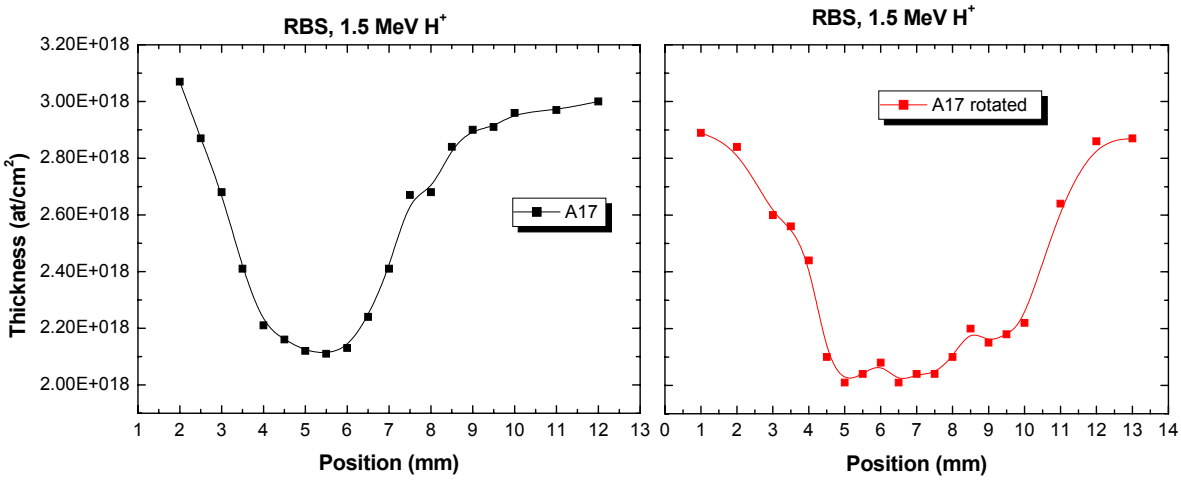

Fig. 3.13. Depth profile of the *a-C:H* film (A17) shown in **Fig. 3.12** obtained by integration of the carbon peak from the spectrum of backscattered protons (with 1.5 MeV incident energy and 0.5 cm^2 spot). The spectra were measured following the direction of the arrows of **Fig. 3.12**, in steps of 0.5 or 1 mm.

For the quantification of the depth profile *RBS* was used. The thickness of the carbon layer is correlated with the integral of the carbon peak from the spectrum of the backscattered protons (incident energy of 1.5 MeV) at a scattering angle of 165º (see **Fig. 3.13**). More details about the calculation of the depth profiles can be found in **Appendix D**.

The spot size on the samples after erosion with 30 eV and 1 keV deuterium varied between ~0.24 and 0.8 cm^2, depending on the extraction and deceleration voltage, and on the size and geometry of the last aperture. **Table 3.4** summarises the calculated equivalent surfaces of the spot for each set of measurements (the 6×3 mm^2 rectangular aperture has been used for all experiments for the reason that it leads to the best profile):

Measurement	**D_3^+ impact energy (extraction-deceleration) [keV]**	**Area, *S* [cm^2]**
TDS 1	3 (4-1)	0.24
TDS 2	3 (4-1)	0.45
Erosion 1	3 (6-3)	0.4
Erosion 2	0.09 (3.09-3)	0.8
Erosion 3	0.09 (3.09-3)	0.8
Erosion 4	0.09 (3.09-3)	0.4

Table 3.4. Calculated equivalent surface areas of the deuterium spot for different combinations of extraction/deceleration voltages measured before a set of measurements were performed.

3.2.3. Fluence dependence measurements

For the investigations of the variation of Y_{tot} as a function of the accumulated fluence, long erosion measurements under deuterium ion bombardment of 30 eV impacting energy were performed. Each measurement took at least one complete week of implantation (continuous bombardment, during both day and night).

a) Determination of the fluence

The fluence is a standard parameter used in the literature for the determination of the amount of atoms implanted during a determined time.

As it was pointed out in sub-section 3.2.1, the target cup is connected to an electronic integrator. This integrator counts the charge passing through it together with the

secondary electrons produced by the impact of the ions on the target. With this value of charge, the fluence has been calculated using the following equation:

$$F = \frac{3 \cdot Q}{e \cdot S} \tag{3.4}$$

where F is the *fluence* [ions/m^2], Q is the *total charge* [C], e is the elementary charge (1.6×10^{-19} C/ion), S represents the area of the beam spot on the surface of the target [m^2] assuming homogeneous flux (the values of S used were summarised in **Table 3.4**) and finally, 3 is the factor regarding the decomposition of D_3^+ into deuterium atoms on the surface of the target.

b) Determination of Y_{tot}

Y_{tot} was determined by weight loss measurements, using the following equation:

$$Y_{tot} = \frac{\Delta m \cdot N_0}{3 \cdot Q \cdot m_2} \tag{3.5}$$

where Δm is the mass change [g], N_0 is Avogadro's number (6.023×10^{23} atom/mol), $3 \cdot Q$ represents the amount of incoming ions, calculated for the particular case of D_3^+ as 3 times the total charge through the target, (the factor 3 again comes from decomposition of D_3^+ into atomic deuterium), and m_2 is the target atomic mass (for the case of carbon, 12 g/mol).

The microbalance permits a very precise (±1 µg) and rapid determination of Y_{tot} thanks to its in-situ location in the vacuum target chamber, which allows a direct measurement of Δm after erosion.

3.2.4. Temperature dependence measurements

For the investigations of Y_{therm}, the target was heated during ion impact by electron bombardment from the rear. Before starting the experiment, the sample was degassed at ~1200 K for 15 minutes. Simultaneously, the calibration of the infrared pyrometer was performed by cross-checking the temperature of the sample with an optical pyrometer.

Fig. 3.14 a shows the usual flow diagram designed for these experiments. The temperature was monitored with the infrared pyrometer during the measurements and recorded using the analogue input of the *QMS*, which was connected to a computer. Throughout ion bombardment, the target temperature was increased in steps by changing

the voltage of the tungsten filament used as source of electrons. This voltage was controlled by a computer programme, which was optimised for a stepwise increase of the temperature, avoiding too long transition times between temperatures. The dwell time was variable for each temperature step, awaiting constant emission of erosion products from the *QMS*. The accumulated fluence per temperature step was usually between 2 and 8×10^{21} D/m^2.

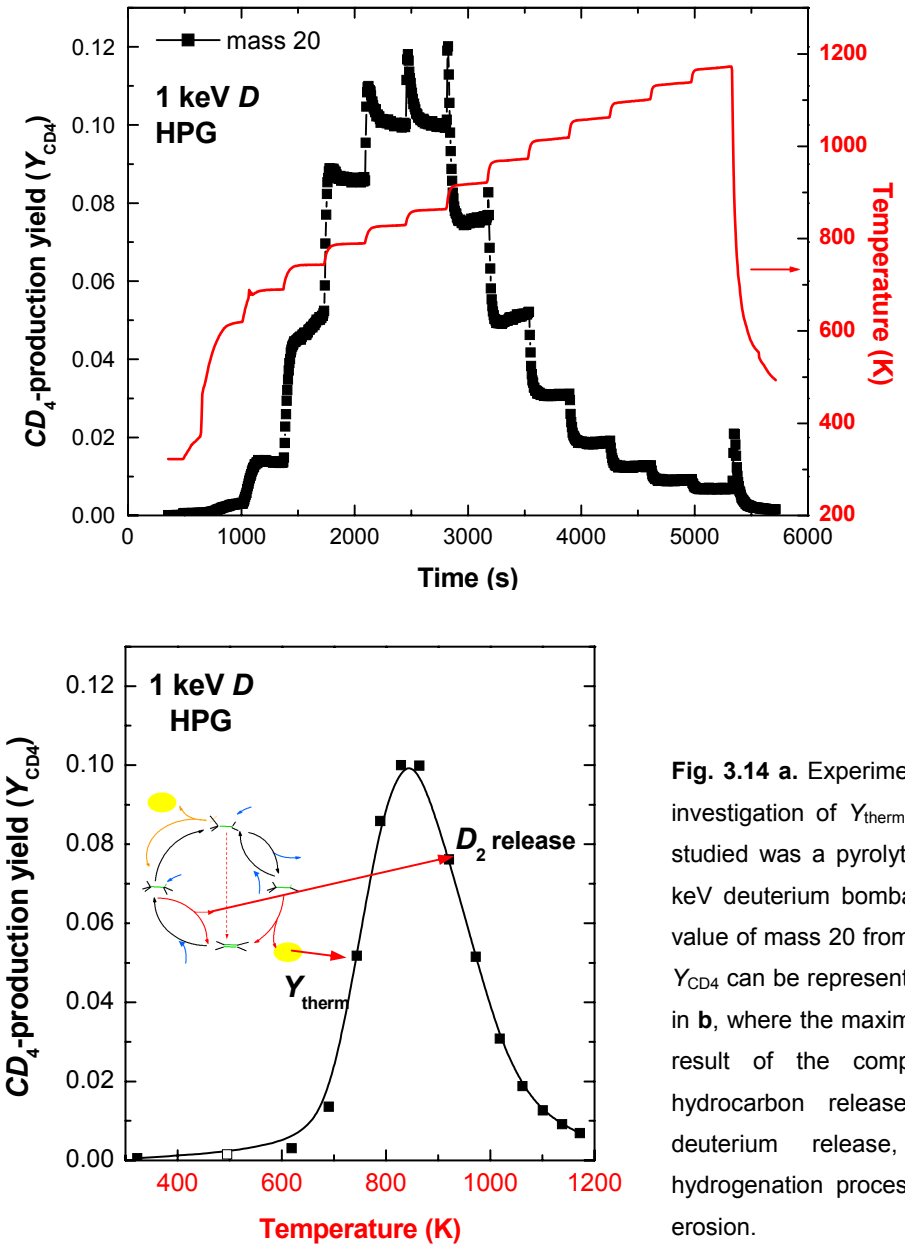

Fig. 3.14 a. Experimental flow path used for the investigation of Y_{therm}. In this case, the sample studied was a pyrolytic graphite (HPG) under 1 keV deuterium bombardment. Taking the mean value of mass 20 from each step of temperature, Y_{CD4} can be represented vs. the temperature like in **b**, where the maximum of Y_{CD4} is clear to see, result of the competition of 2 processes: hydrocarbon release, given by Y_{therm}, and deuterium release, which interrupts the hydrogenation process and stops the chemical erosion.

Y_{therm} was investigated with the *QMS* by evaluating the measured eroded hydrocarbon species of masses between 2 and 40, which were recorded as a function of time during ion bombardment. The *CD_4-production yield*, Y_{CD4}, was investigated particularly, i.e. the

signal for mass 20 (CD_4) was predominantly evaluated. Mass 18 was also investigated in more detail than other masses in order to study the production of the radical CD_3. But it is necessary to take into account other disturbing contributions to both masses 18 and 20. For example, mass 18 could also come from CD_2H_2, H_2O, and DO from cracked deuterated water (D_2O). D_2O itself contributes to mass 20, as well as CD_4 molecules from the background gas and from the recombination of CD_3 with D on the walls. Nevertheless, deuterated heavier hydrocarbons do not crack into mass 20 and cracking into mass 18 is less than 4% [163,164], i.e. mass 18 and 20 are good indicators of the production of CD_3 and CD_4, respectively.

The measurement started at *RT* with all valves closed. After around 1 minute the valve between the *QMS* and the target chamber was opened. The next step was opening the valve separating the magnetic analyser and the target chamber. Afterwards, the valve between the vacuum pump and of the target chamber was closed and, in this way, the residual gas pressure increased, i.e. the intensity of the *QMS* signals was higher than before. Subsequently, the high voltage was regulated to allow the deuterium ion beam to impinge on the target. Then, the programme controlling the temperature was started and the specimen temperature was increased in steps with varying dwell time awaiting about constant emission of CD_4. By abruptly changing the temperature, transient peaks in the CD_4 emission are sometimes observed, due to an excess in sp^3 complexes, analogous to previously reported transient behaviours [165,166].

In the last step of the temperature ramp, the beam was switched on and off for recording the background of the mass 20 without beam. After that, the programme stopped and the sample was cooled down until reaching again ~*RT*. At the end, and before finishing the experiment, the valves were closed in reverse order of the start-up procedure.

Taking the mean value of mass 20 from each step of temperature, Y_{CD4} can be represented vs. the temperature as shown in **Fig. 3.14 b**, where the maximum of Y_{CD4} is clear to see, result of the competition of the 2 processes already explained in sub-section 2.1.2: the thermal release of hydrocarbon groups, given by Y_{therm}, and the thermal release of deuterium, which is activated at higher temperatures and interrupts the hydrogenation process, stopping the chemical erosion.

It is important to call attention to the first data point of a temperature dependence experiment, which is always measured at *RT*. Therefore, when the deuterium impacting energy is 30 eV, this data will not correspond to Y_{therm}, but to Y_{surf}, because the thermal release of deuterium has not yet been activated (Y_{therm} at *RT* is always zero).

Background correction and QMS calibration

For the background correction, the intensities of the mass signals without ion beam were recorded at *RT* (two times: before starting the measurement and after the cooling down phase at the end) and once more, at the maximum temperature achieved during the temperature ramp. A linear increase of the background with increasing temperature was assumed (or linear decrease with decreasing temperature), and the recorded signals without ion beam were used for its calculation. The linearity was checked at some intermediate temperatures, for which the calculated linear interpolation resulted to be very close to the real background measured. Thus, although this assumption unavoidably introduces an error in the evaluation of the data, this error has been proven to lead only to slight variations of Y_{CD4}, which could be a little more important at temperatures close to *RT* and the maximum temperature. Besides, the method has been verified to be very robust.

The contribution of the beam-induced background originated at the apertures of the beam or by reflected deuterium at the wall could be estimated from measurements on specimens without chemical erosion of carbon, e.g. *Si* or *W*. In such measurements the signals of mass 18 and 20 during the deuterium bombardment have small and nearly constant values above the background gas level. These values vary from measurement to measurement. The contribution of the beam-induced background is between half and twice that of the background gas and is not taken into account in the background correction.

The calibration of Y_{CD4} was carried out in the same way as reported and discussed in detail in [59], by setting the maximum CD_4 signal of pyrolytic graphite bombarded with 1 keV deuterium at T_{max} (~850 K) equal to Y_{therm} = 0.1. This value was gained by subtracting the contribution of Y_{phys} to Y_{tot}, which was determined by weight loss measurements [67]. This assumption equals Y_{therm} to Y_{CD4}, presupposing that the only molecule chemically produced at this energy and this temperature is CD_4, which is in fact observed to be the most predominant molecule formed [111-113,167]. However, this calibration does not take into account variations in the ratios of radicals to molecules and C_1D_z to heavier hydrocarbons, $C_{x>1}D_y$ for different impact energies. The contribution of heavier hydrocarbon groups to Y_{chem} (both Y_{therm} and Y_{surf}) has already been investigated by other authors and it was found to be significant at deuterium impact energies lower than 100 eV (~Y_{chem}/2) [168,169]. Thus, an absolute important error, of the order of a factor of 2, will be introduced in the measurements performed at impacting deuterium energy of 30 eV. Nevertheless, this absolute mistake does not disturb the comparison of different data calibrated in the same way.

3.2.5. Thermal desorption spectroscopy measurements (TDS)

Thermal desorption spectroscopy (*TDS*) measurements were performed for different doped graphite samples produced at *CEIT* by deuterium ion implantation, in order to obtained the total amount of deuterium retained after a certain ion fluence.

Fig. 3.15 offers a good overview of the experimental flow path. During the first phase, the implantation, the ion source was adjusted to produce 4 keV D_3^+ ions, which were extracted, magnetically energy/mass separated and decelerated to 3 keV D_3^+ (resulting in an energy of 1keV per deuterium).

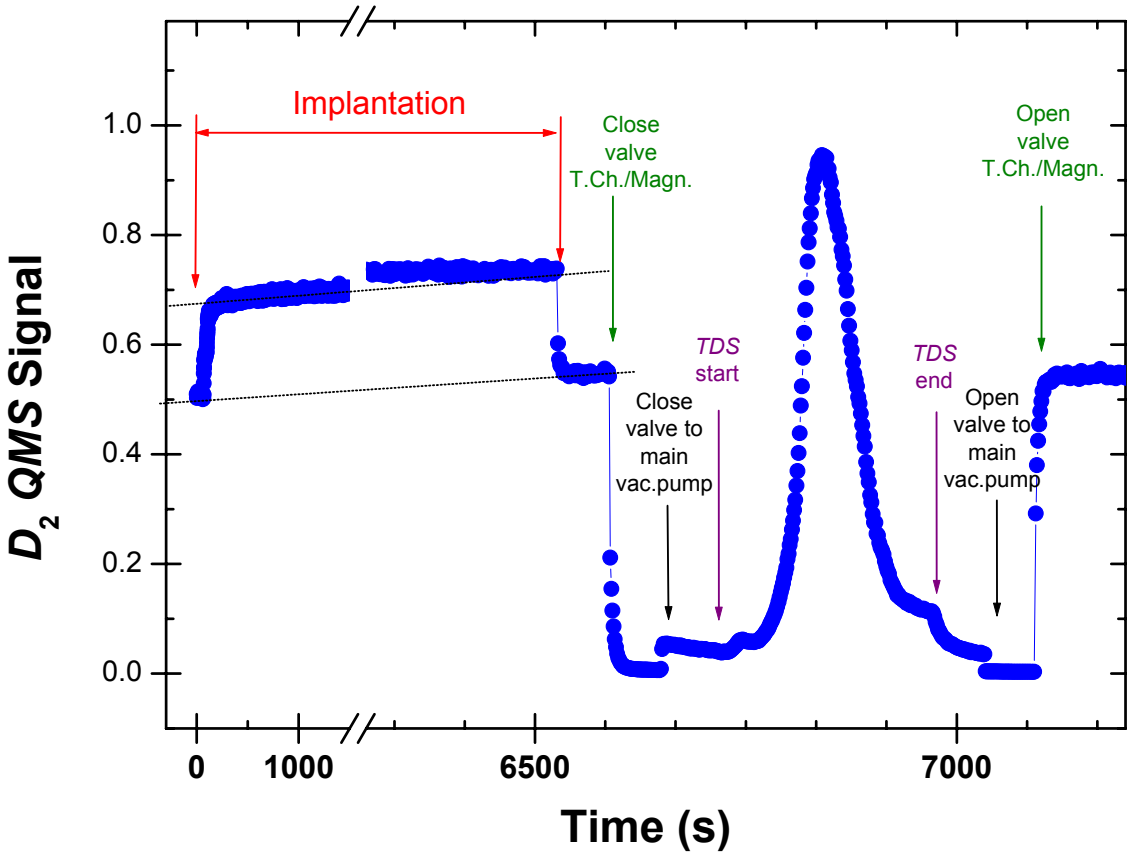

Fig. 3.15. Path flow diagram for the *TDS* measurements. The close/opening of two important valves has also been indicated: the one between the target chamber and the magnetic analyser (T.Ch./Magn) and the one that isolates the turbo-molecular vacuum pump from the target chamber (vac. pump).

The *TDS* measurements were always started 6 minutes after finishing the implantation. The samples were linearly heated up to about 1400 K (heating rate~5.7±0.5 K/s) in the same way as for the erosion measurements (electron bombardment). The highest temperature was held for 1 minute.

Relevant masses were investigated and recorded with the *QMS* every 6 seconds: masses 2, 3, 4 and 20, which were attributed to the species H_2, HD, D_2 and CD_4, respectively; and masses attributed to C_2D_y species (masses 26, 28, 30 and 34).

Data processing and QMS calibration

The data processing is quite complex. The amount of retained deuterium in the specimen was calculated from the contribution of D_2 and CD_4 by integrating the signals and multiplying them with a sensitivity factor (the *HD* signal was neglected). For this, it is necessary, on the one hand, to obtain the sensitivity factors for both masses and, on the other hand, to determine and subtract the backgrounds before integrating the signals.

The sensitivity factor for the D_2 signal was obtained by implanting a *Ti* sample at *RT* under the same conditions and after that performing *TDS*. Since this metal has very high trapping at 1 keV (~100%) and its reflection coefficient is well known (~15%) [41], the theoretical amount of retained deuterium can be calculated, and with this value the calibration coefficient for the D_2 was obtained after background subtraction.

The sensitivity factor for the CD_4 signal was determined by taking the ratio of the D_2 and CD_4 integrals determined in a previous study [94] for the same kind of pyrolytic graphite at the same fluence.

Before integrating the D_2 signal, it is necessary to subtract the linear background and then to separate the part coming from the specimen and from the thermal desorption of the sample surrounding, which warms up during *TDS*. It is supposed that desorption of D_2 and desorption of H_2 from the surrounding are linearly correlated, and that the deuterium signal just before switching off the heating is coming from this background. The factor between the H_2 and D_2 intensities strongly varies with the history of the machine (e.g. last venting). The background-subtracted D_2 intensity nearly vanishes for all measurements just after reaching the highest temperature. An equivalent background subtraction was made for the *HD* signal. The CD_4 signal was integrated without any treatment.

As mentioned before, the *HD* signal has been neglected for the determination of the deuterium retention. To get an idea of the error introduced by neglecting this mass, the amount of deuterium released as *HD* was calculated in an analogue way to the D_2 signal. For most measurements this contribution resulted to be only of 3%, and for a few it reached nearly 6% of the final retained deuterium (counting only D_2 and CD_4).

4. Results and discussion

The results are divided into the two principal areas of this work: influence of dopants on the chemical erosion mechanisms of carbon by deuterium impact and influence of dopants on the deuterium retention by implantation. In the first part, which is the longest one, dedicated to the investigation of the mechanisms of chemical erosion of doped carbon materials, multi-component effects leading to a preferential erosion of carbon are considered, too. Some supporting erosion measurements complete the knowledge comparing the results obtained under mono-energetic ion beam bombardment with different results gained in two different plasma devices. In order to get a better understanding of the erosion processes, innovative investigations of Y_{tot} and Y_{CD4} performed below *RT* under low deuterium impact energy complete the comprehension of the erosion mechanisms. In the second part, *TDS* measurements are shortly introduced and compared with literature data for discussing the influence of dopants on the deuterium retention by implantation. Finally, the open questions formulated at the end of section 2 will be answered.

4.1. Influence of dopants on Y_{surf} and Y_{therm}

This chapter is dedicated to the investigation of the influence of doping on the mechanisms involved in the chemical erosion of carbon under deuterium bombardment.

A possible way to influence Y_{tot} with dopants is by means of chemical changes. A chemical interaction of the metal carbide with the electronic structure of carbon in the graphite lattice might vary the mechanisms implicated in the chemical erosion of carbon, and its contribution has to be investigated. With this intention, the surface regime, given by Y_{surf} and the thermally activated regime, given by Y_{therm}, will be considered separately.

Furthermore, the addition of dopants transforms the carbon material into a composite material, so additional multi-component effects have to be taken into account, since they will also influence both erosion regimes.

4.1.1. Multi-component effects

Surface morphology and composition changes of the samples during ion bombardment have to be considered when investigating the influence of dopants on the chemical erosion mechanisms of carbon by deuterium impact. These changes are expected because the individual components in a composed material exhibit different erosion yields due to their different masses and binding energies. Since the doped carbon materials investigated are composed of two phases, carbon and metal carbides, and carbon has a higher sputtering yield than the metals and the carbides [46], during bombardment with deuterium ions, carbon will be eroded faster than the carbides, leading to changes in the surface composition.

The preferential erosion of carbon is especially manifest in experiments at low impact energies, at which carbon is chemically eroded and the erosion yields of the dopants are negligible due to the proximity to E_{th} for physical sputtering. Moreover, when the impacting energy is even below this E_{th}, only carbon will be eroded. In contrast, the carbides will remain on the surface, shielding the underlying carbon atoms and protecting them from further erosion, resulting in a strong reduction of Y_{tot} after long bombardment times. The corresponding evolution of the surface morphology has been illustrated in **Fig. 4.1**. As it has already been mentioned in sub-section 2.3.2, the dopant enrichment on the surface increases until reaching a steady state after long fluences, when a surface layer with a thickness of about the mean dopant particle distance is eroded and the carbides completely shield the carbon surface [24,29].

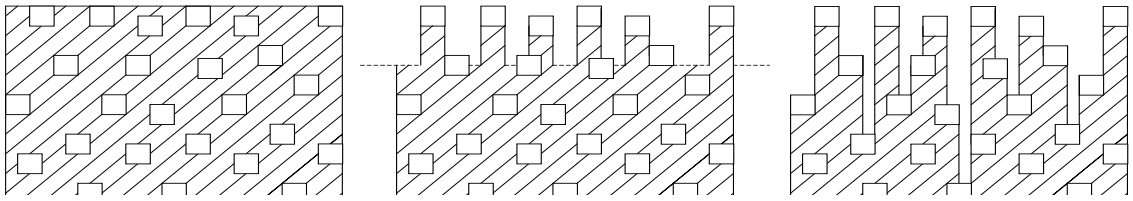

Fig. 4.1. Schematic illustrating the evolution of the surface morphology of a metal carbide doped graphite under deuterium ion bombardment when the energy of the impinging ions is below the threshold energy for physical sputtering of the metal carbides. On the left: initial surface; on the right: modified surface covered with a pure metal carbide; in the centre: intermediate state.

Summarising, an influence of dopants on Y_{tot} always exists, at least due to the expected preferential erosion of carbon and the resulting enrichment of dopant on the

surface. A fluence dependence of the erosion yield always occurs. So the preferential erosion of carbon always has to be considered. This effect will lead to beneficial consequences regarding the reduction of the net erosion of carbon. At the same time, the development of a strong surface topography is expected.

Establishing the difference between a chemical influence of the dopants on the chemical erosion mechanisms and a modification of the yield due to morphological changes on the surface is a rather complicated issue and should be carefully addressed.

4.1.2. Fluence dependence measurements

In order to study the influence of doping on Y_{surf}, erosion measurements were performed at *RT* under 30 eV deuterium bombardment. This deuterium impacting energy is very close to the threshold energy for physical sputtering of carbon (E_{th} = 24.3 eV [46]), such that Y_{phys} can be neglected at this energy. Thus, under these conditions Y_{surf} is the only contributor to the total erosion of carbon, (see sub-section 2.1.2 for more details), i.e. Y_{tot} is equivalent to Y_{surf} and therefore, Y_{tot} has been investigated for the study of Y_{surf}.

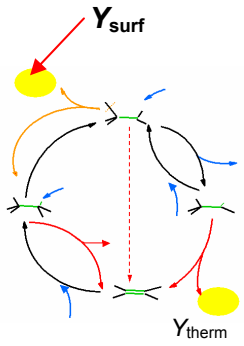

The determination of Y_{tot} was performed by weight loss measurements assuming that only carbon was eroded. The assumption was made regarding the fact that the selected impacting energy of the deuterium ions was always below the threshold energy E_{th} for physical sputtering of the dopants. To confirm this, **Table 4.1** collects some experimental data for E_{th} of the different dopants investigated in this thesis, both in pure metal state and as metal carbides. It is observable that all values of E_{th} are above 30 eV.

	Ti	*TiC*	*V*	V_8C_7	*W*	*WC*	*Zr*	*ZrC*
E_{th} exp. [eV]	33.2	54	Not available	Not available	178	171	100	74

Table 4.1. Experimental threshold energies E_{th} for physical sputtering of some pure metals and metal carbides under deuterium bombardment. [46].

Actually, due to the reflection of the deuterium ions, some lateral erosion of carbon could also happen, leading to a loss of the carbide grains during the measurement itself and the introduction of errors in the calculation of Y_{tot}. Re-deposition of eroded particles

has also not been taken into account for obtaining Y_{tot}, which would lead to an additional error. The quantification of these errors is unfortunately unfeasible, but this existence should be considered for a proper interpretation of the data.

The selected energy for the investigation of Y_{surf}, 30 eV, is also a good choice for evaluating the reduction of the yield caused by the preferential erosion of carbon, due to the aforementioned reasons. Fluence dependence experiments were aimed to this. At intervals of typically 1×10^{24} D/m^2 weight loss measurements were done. Fluences up to 10^{25} D/m^2 were accumulated, because this reduction is expected to increase with increasing ion fluence.

But how to distinguish the chemical effects of dopants on Y_{surf} and the effect of preferential erosion of carbon? These two effects might be separated at very low fluences, where morphological changes are minimum. But the accumulation of a certain fluence is always unavoidable and particularly when experimental data are got by weight loss.

Different specimens were selected for the separate investigation of diverse parameters, such as type of dopant, dopant concentration and size of the dopants. The denotation and some properties of these materials have already been listed in **Table 3.1**. In the following, the results will be shown one by one and afterwards discussed entirely.

Carbide-doped fine-grain graphites

a) Parameters: type of dopant, dopant concentration and size of dopant

The fluence dependence of Y_{tot} is shown in **Fig. 4.2** for different pure fine-grain graphite and various metal carbide doped graphites. The graphites were similarly produced at *CEIT* and contain 4 at.% of the metal in the bulk. The aim of these measurements is to investigate the influence of the type of dopant.

Initially, at very low fluences (~10^{23} D/m^2), none of the doped samples showed a reduction of Y_{tot} compared to pure fine-grain graphite. This fact indicates that there is no existing chemical influence of dopants on Y_{surf}.

After long bombardment, at high ion fluences (~10^{25} D/m^2), a reduction of Y_{tot} by up to a factor of ~10 was found for the *TiC*-doped graphite, and about a factor of 2 for the *WC*- and V_8C_7-doped graphites. These differences complicate the interpretation of **Fig. 4.2**: on the one hand, there is no observable chemical influence of doping on Y_{surf} from the

analysed results at low fluences; but on the other hand, the observable differences of the yield for each doped specimen at large fluences suggest that Y_{tot} depends on the kind of metal carbide used as dopant, proposing *TiC* as the most effective one.

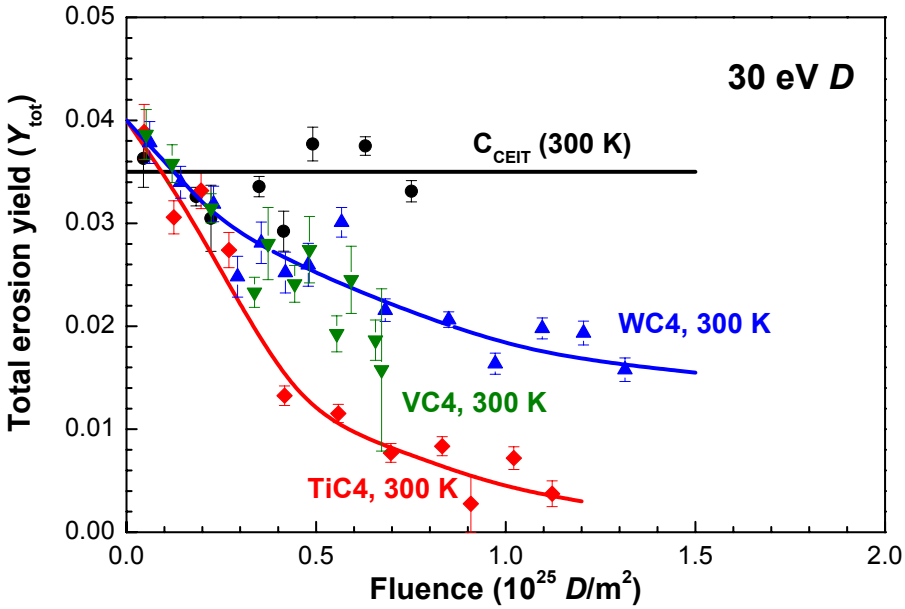

Fig. 4.2. Fluence dependence of the total erosion yield measured by weight loss for 30 eV deuterium impact at *RT*. The results are shown for a fine grain graphite (C_{CEIT}) and different carbide-doped graphites produced at *CEIT* with a metal concentration of about 4 at.% (TiC4: *Ti*; VC4: *V*; WC4: *W*). The lines are to guide the eye.

The contribution of the preferential erosion of carbon to the reduction of Y_{tot} is certainly responsible for a large part of the strong reduction of Y_{tot} at high fluences, but its quantification is problematic due to the differences shown when different metal carbides are used as dopants.

Fig. 4.3 illustrates the evolution of Y_{tot} as a function of the deuterium ion fluence at *RT*, again for 30 eV ion impact energy. In this case, all investigated graphites are doped with the same dopant, *TiC*. The dopant particles have different sizes, and the amount of dopant used for each sample is different, too. So the aim of these measurements is to investigate the effect of the size and amount of dopant.

The results for the pure fine-grain graphite and the 4 at.% *Ti*-doped samples produced at *CEIT*, which have already been shown in **Fig. 4.2**, are included for comparison. Another *TiC*-doped graphite sample manufactured at *CEIT* with a smaller concentration of *Ti* (2 at.%, TiC2) was investigated as well. The last specimen examined was a commercial *TiC*-doped graphite (LT10) with a doping content of 10 at.% *Ti* , for which the size of the carbides was three times larger than for the other *Ti*-doped graphites.

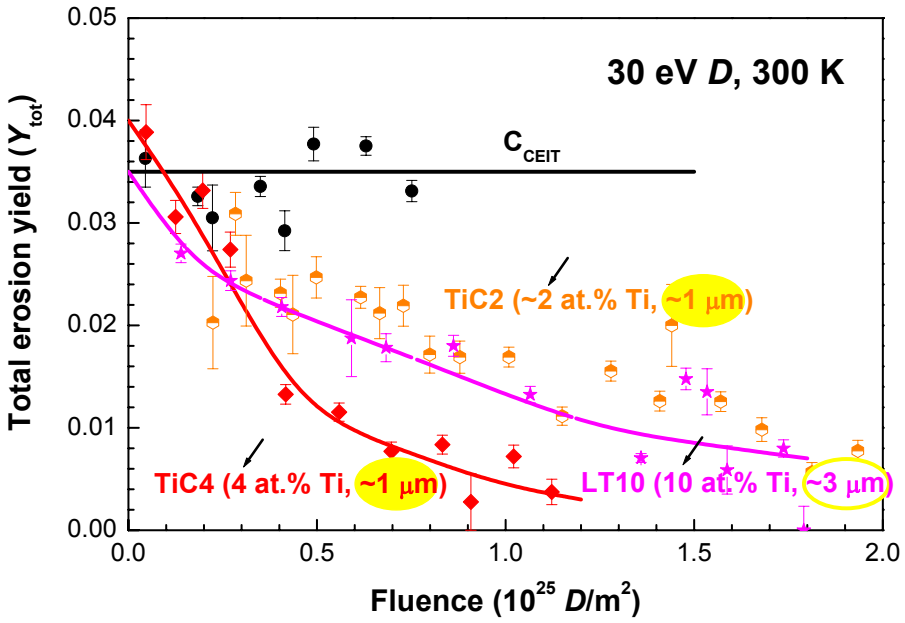

Fig. 4.3. Fluence dependence of the total erosion yield measured by weight loss for 30 eV deuterium impact at *RT*. The lines are only to guide the eye. The results are shown for pure fine-grain graphite (C_{CEIT}), two *TiC*-doped samples with different *Ti* concentrations manufactured at *CEIT* (TiC2: 2 at.% and TiC4: 4 at.%), and the commercial *Tic*-doped LT10 (10 at.% *Ti*). The mean particle size of the carbides is given.

As before, **Fig. 4.3** does not show any reduction of the yield by doping at low fluences, compared to pure graphite, i.e. an influence of doping on Y_{surf} is not perceptible. The 4 at.% *Ti*-doped graphite again represents the strongest reduction of Y_{tot} after a long bombardment time. The reduction of the yield observed for the 2 at.% *Ti*-doped graphite sample is similar to the one seen for the 4 at.% *Ti*-doped sample, but after about twice the fluence. This is in accordance with the contribution of the preferential erosion of carbon to the reduction of the yield: higher dopant concentration protects a larger region of carbon from further erosion.

The very similar fluence dependence of Y_{tot} for the 2 and the 10 at.% *TiC*-doped graphites is also noticeable, even though these two specimens have very different amount of dopant. But the size of the dopants also plays an important role in the reduction of the yield by shielding the structure of carbon. As expected, the fluence needed for the same increase in surface coverage is smaller for smaller grain sizes

Summarising, the analysis of **Fig. 4.3** reveals a dependence of Y_{tot} on both the amount and the size of dopant particles. This dependence is well understood if we assume the preferential erosion of carbon as the only mechanism responsible for the reduction of Y_{tot}. The reduction of the yield is faster for larger amounts of dopants and smaller sizes,

because the thickness of the surface layer, which has to be eroded until achieving a complete carbide-covered surface is smaller.

The last fluence dependence measurements of Y_{tot} were performed on other undoped and 4 at.% *Ti*-doped graphites produced at *CEIT* under 30 eV deuterium ion bombardment changing the conditions of the experiment: increasing the temperature to 620 K in order to investigate the fluence dependence of Y_{tot} when the thermal erosion regime, Y_{therm}, is activated.

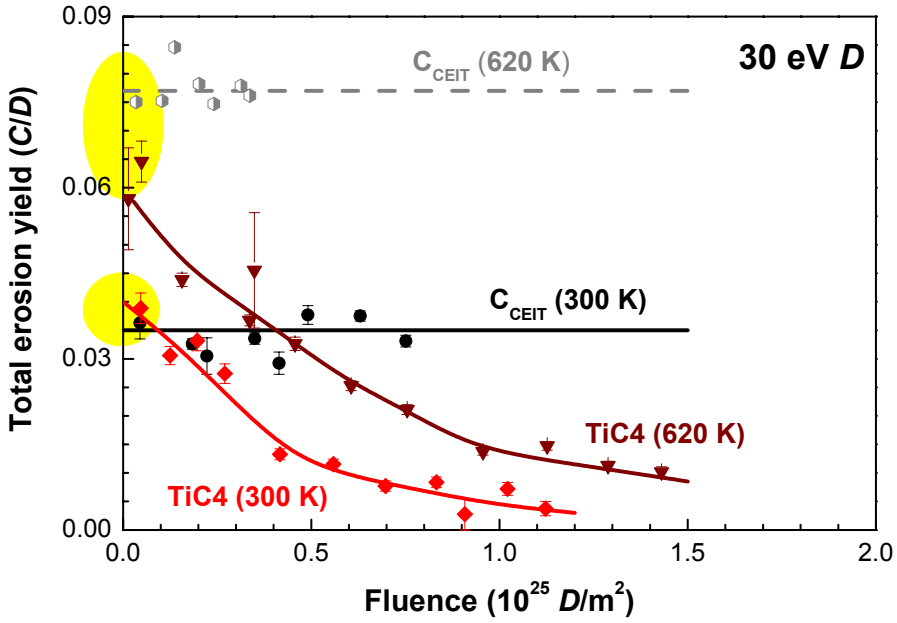

Fig. 4.4. Fluence dependence of the total erosion yield measured by weight loss for 30 eV deuterium impact at *RT* and at 620 K. The lines are only to guide the eye. The results are shown for pure fine-grain graphite (C_{CEIT}) and for *TiC*-doped fine-grain graphite from *CEIT* containing 4 at.% of *Ti* (TiC4).

Fig. 4.4 gives the results. Again, for comparison, the fluence dependence of Y_{tot} for the pure and the 4 at.% *Ti*-doped graphites measured at *RT* have been included. For the 4 at.% *Ti*-doped specimen, the evolution of Y_{tot} with the fluence at elevated temperature is very similar to the one observed for the analogous sample at *RT*: for both, the corresponding measured data points show a relatively parallel drop when the fluence increases. The geometrical effect of the dopants explains the diminution of Y_{tot} with the fluence. A higher erosion yield is also expected when the thermal erosion regime is entered (see **Fig. 2.2**)

But the central difference between the behaviour shown at *RT* and the one observed at 620 K can be noticed in Y_{tot} at very low fluences (indicated with yellow ellipses in **Fig. 4.4**). When Y_{therm} is activated at elevated temperatures, a clear reduction of Y_{tot} for the 4

at.% *Ti*-doped graphite turns out, compared to the undoped case. This reduction has never been observed at *RT*. From **Fig. 4.4** it can surely be concluded that, as soon as Y_{therm} is activated, chemical changes caused by doping are involved in the reduction of Y_{tot}.

The influence of doping on Y_{therm} will be further investigated in detail in the next sub-section by temperature dependence measurements.

b) Discussion

Fluence dependence experiments have been performed in order to evaluate the contribution of the preferential erosion of carbon to a reduction of the net erosion and to investigate the influence of dopants on Y_{surf}. All results showed a reduction of Y_{tot} with increasing deuterium ion fluences. For the majority of the results this diminution can be explained by considering the expected preferential erosion of carbon and the corresponding enrichment of dopant on the surface [24,29,128,129].

However, an additional dopant-dependent effect on Y_{surf} seems essential to explain the different erosion behaviours observed for each different type of dopant (illustrated in **Fig. 4.2**). If the carbide grains had the same size and were in the same amount similarly distributed among the carbon material, the same area of carbon should be protected after similar ion fluences, such that the same reduction had to be observed, independent of the type of dopant. Since the reduction measured for each dopant is different (see **Fig. 4.2**), a possible chemical influence on Y_{surf} by doping is again open to discussion.

Chemical changes would implicate that the presence of the dopant affects the electronic structure of some neighbouring carbon atoms around it. Possibly, these changes would be different depending on the type of element selected as dopant. The created bonds between deuterium and carbon atoms would perhaps be strengthened, or even the presence of the dopant could prevent the formation of these hydrocarbon molecules. However, accepting this chemical influence of the dopants as true, an important observation remains unintelligible: why does this reduction not occur already at low ion fluences? In principle, there is no reason to presume that the electronic system of carbon is not affected from the beginning of the ion bombardment. An evidence of this is given by the analysis of **Fig. 4.4**. This figure shows two supplementary experiments performed at 620 K for the investigation of the fluence dependence of Y_{tot} when Y_{therm} is activated. At low fluences, a clear reduction of Y_{therm} is observed for the 4 at.% *Ti*-doped graphite compared to the undoped one measured at the same temperature, which indicates that chemistry is definitely involved in the diminution of Y_{therm}: the bombardment

time was too short to modify the surface by preferential erosion of carbon; so it is not possible to explain the reduction only by the geometrical shielding effect. If chemistry were also implicated in the reduction of Y_{surf}, some similar appearance would have to be noticeable at low fluences, too. So this premise does not look consistent.

In order to search for an answer to the apparent incongruous observations concerning **Fig. 4.2**, surface morphologies of the eroded samples as well as composition changes caused by the preferential erosion of carbon were further investigated by *Scanning Electron Microscopy* (*SEM*). Besides, re-deposition of eroded particles and loss of carbide grains, which might introduce already-mentioned errors in the determination of Y_{tot}, were also considered.

c) Surface morphology and composition changes

The preferential erosion of carbon after high ion fluences was confirmed by *SEM* investigations. As an example, **Fig. 4.5** shows the strongly changed surface morphology with a roughness of several µm for the *TiC*-doped graphite (for which Y_{tot} was investigated in **Fig. 4.2**) after an accumulated ion fluence of ~1.1x10^{25} *D*/m^2. A columnar structure had developed, where the *TiC* grains protect the underlying graphite from further erosion.

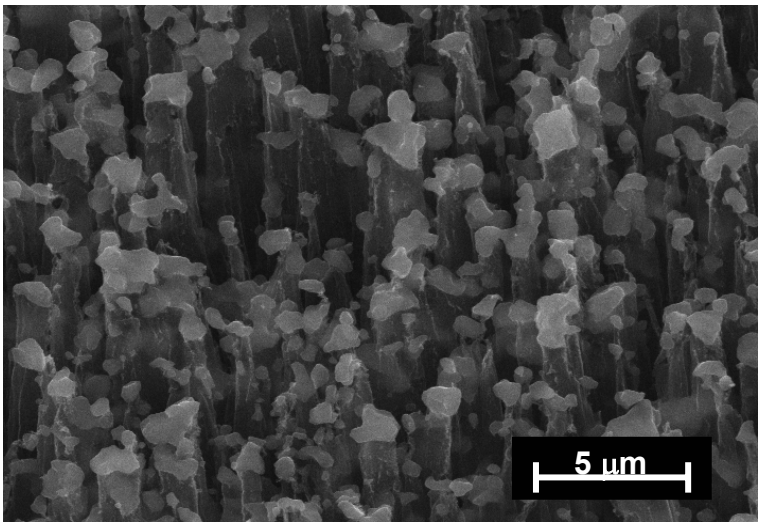

Fig. 4.5. Surface morphology of the sample TiC4 (4 at.% *Ti*-doped fine-grain graphite) after erosion with 30 eV *D* impact at *RT* (accumulated ion fluence ~1.1x10^{25} *D*/m^2).

The *WC*-doped graphite also displays a similar columnar structure after long fluences. But the distribution of *WC* grains in the carbon matrix is fairly inhomogeneous, as it can be distinguished in *SEM* pictures of this specimen, shown in **Fig. 4.6**.

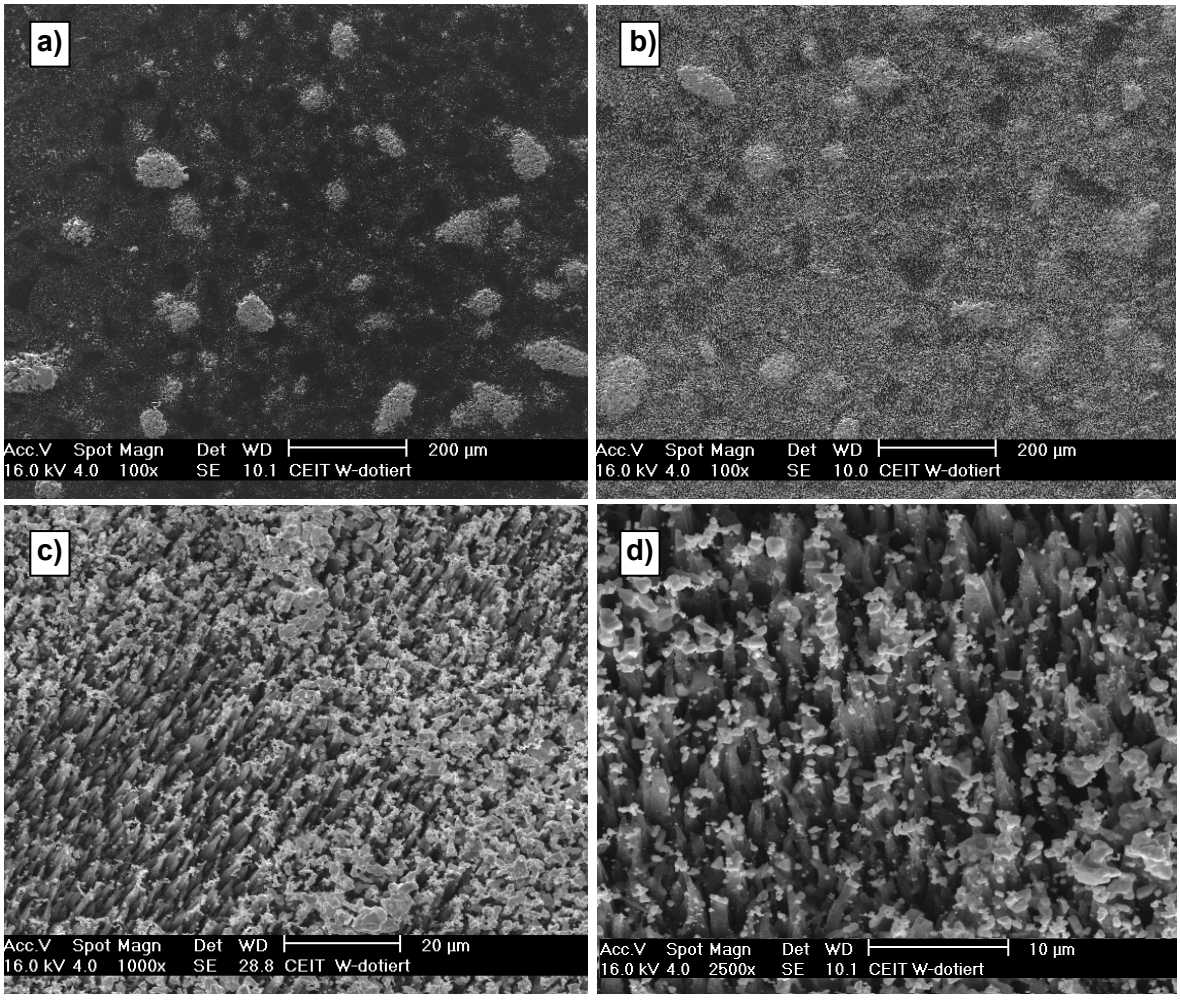

Fig. 4.6. *SEM* images showing the surface morphology of the specimen WC4 (*WC*-doped graphite from *CEIT* with 4 at.% *W*) **a**) before and **b**), **c**) and **d**) after deuterium ion bombardment at 30 eV impacting energy. Agglomerations and areas with depletion in metal carbides are visible. The enrichment in *WC* grains on the surface is also patent.

The distribution of V_8C_7 grains in the V_8C_7-doped graphite is imperfect as well[2]. **Fig. 4.7 a** and **b** show further *SEM* images of this specimen. By simple visual inspection, the enrichment in carbide grains at a micro-scale after erosion is discernible on the surface.

[2] The specimens mentioned here were from the first batch produced at *CEIT*; currently, *WC*- and V_8C_7-doped graphites are also manufactured with homogeneous distribution of the dopants.

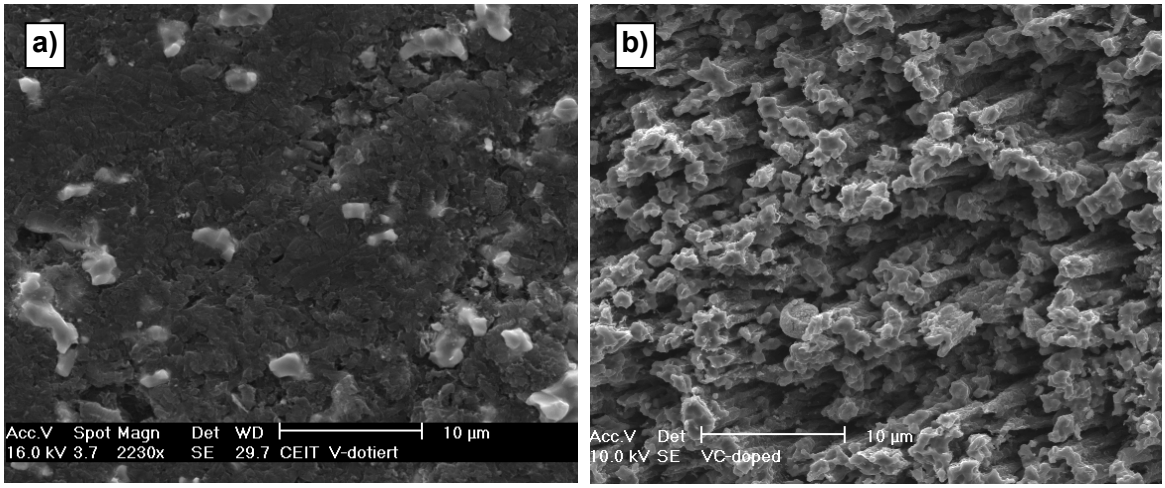

Fig. 4.7. *SEM* images showing the morphology of the specimen VC4 (V_8C_7-doped graphite with 4 at.% *V*) **a**) before and **b**) after bombardment with 30 eV deuterium ions at *RT*. The V_8C_7 grains have bright contrast, while the dark regions correspond to carbon.

This already commented introduction of heterogeneities in the distribution of the carbides during the manufacture (see sub-section 3.1.1) increases the main distance between carbide grains in some regions; so corresponding higher ion fluences will be required for eroding the complete carbon surface of the *WC*- and V_8C_7-doped samples until obtaining a total carbide-covered outside.

Besides, if a possible loss of carbide grains during the erosion experiment is considered, the corresponding error introduced in the calculation of Y_{tot} will be the higher, the heavier the carbides are. So for the case of the *WC*-doped graphite, a small loss of carbide grains could considerably have systematically increased the value of Y_{tot}, due to their high weight.

Finally, it can be concluded from the examination of the surface morphologies that no difference in chemical behaviour is required to explain the differences shown in **Fig. 4.2**: Y_{surf} is not chemically affected by doping with metal carbides.

Further surface morphology investigations were performed for the undoped graphites, in order to compare their eroded surfaces with the modified surface morphologies of the eroded carbide-doped graphites. To illustrate this, **Fig. 4.8** compares the surface morphology of a pure graphite (**a**) before and (**b**) after erosion under 30 eV deuterium ion bombardment at *RT*. A surprising finding was discovered by *SEM* examination: after erosion, the graphitic areas are also covered with a needle-like structure. The directional impact of the deuterium ions is evident from the images (see **Fig. 4.8 b**).

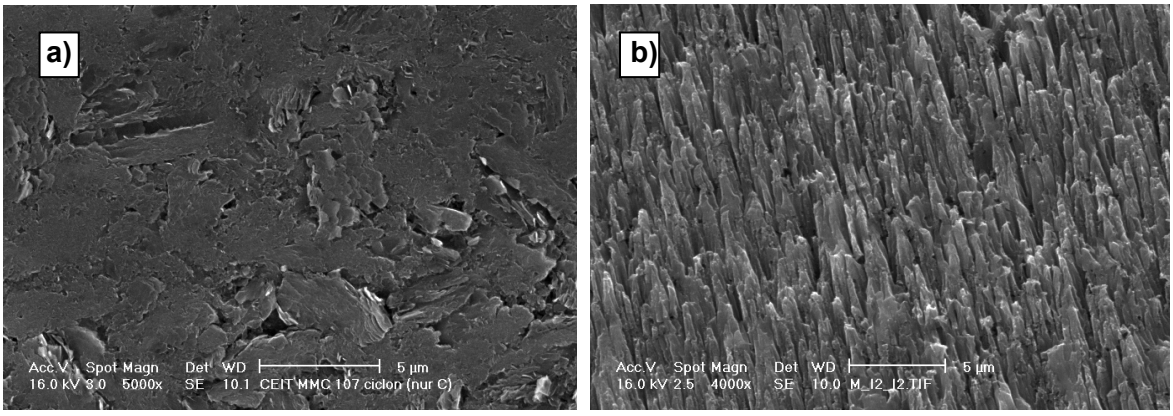

Fig. 4.8. *SEM* images of a pure fine-grain graphite produced at *CEIT* (C_{CEIT}) **a**) before the erosion experiment and **b**) after deuterium ion bombardment at impacting energy of 30 eV and at *RT* (accumulated fluence ~1×10^{25} D/m^2).

EDX analysis proved that no impurities remain on the top of the cone structure, which would have clarified the strongly rough morphology. So another explanation is required. From the comparison of both structures, it can be elucidated that erosion starts at weak structural places, such as porosity or grain boundaries. During ion bombardment, the initial surface roughing becomes more pronounced, and due to the reflection of deuterium ions and the angular dependence of the physical sputtering [46], abrupt slopes are formed in the carbon structure. After long fluences, the surface structure looks like the image shown in **Fig. 4.8 b.**

It is important to remark that changes in the surface morphology of pure carbon after low energetic deuterium ion impact does not necessarily lead to a reduction in net erosion. In fact, no fluence dependence of Y_{tot} has been observed for the pure graphite (already shown in **Fig. 4.4**). So, although a strong roughness is developed, erosion of the top of the needle structures also takes place.

d) Comparing results with erosion measurements by plasmas

In this sub-section, the obtained fluence dependencies of Y_{tot} measured at the Garching high current ion source will be compared with those obtained by well-characterised plasmas with a high content of thermal atomic hydrogen: the inductively coupled *RF* plasma generator at the University of Augsburg, and the plasma simulator PISCES-B at the University of California in San Diego (*UCSD*).

The motivation for the performance of these experiments was to take advantage of the higher deuterium fluxes reached at these plasma simulators in order to extend the

fluence dependence of the measurements. This allows to accumulate high fluences very quickly (in some hours, which would have been several days at the Garching high current ion source).

Another important aim was to evaluate the contribution to the erosion yield of simultaneously incident atomic deuterium with deuterium ions. As it has already been introduced in sub-section 3.2.1, the particle and energy loads to the *PFM* are characterised by a broad variety of particle, energy, and angle distributions. As input data for simulations of the plasma-wall interaction, erosion yields from ion beam experiments are used [9,170,171]. In the case of carbon, this has to be done with care, because its chemical erosion by atomic hydrogen has a synergetic effect with simultaneously impacting hydrogen ions [43,72,157]. In particular for carbon, impact of atomic hydrogen results in an erosion yield two orders of magnitude lower than with simultaneous bombardment by atomic hydrogen and low energy ions (ion energy above several eV) [72]. Therefore, simple superposition of erosion yields, which is right when only physical sputtering occurs, does not describe the behaviour of carbon-based materials under simultaneous impact of atomic and ionic hydrogen.

With these aims, pure graphite samples as well as doped graphites from *CEIT* were exposed to the well-characterised plasmas at the University of Augsburg and the *UCSD* within the frame of a collaboration work in order to perform fluence dependence measurements. In the following the main results obtained in both places will be shown and discussed.

➔ Augsburg: planar inductively coupled RF plasma

Before presenting the results, a brief description of the main plasma parameters used is necessary. A plasma was ignited in a mixture of D_2 (H_2) and *He* gas in the ratio 1 to 10 at a total pressure of 20 Pa in a small vacuum chamber (~2 l volume). The reason to use *He* was to maximise the total (atomic and as well as ionic) hydrogen flux onto the specimen. A *radio frequency* (*RF*) power of 250 W was inductively coupled into the plasma with a planar coil (*frequency*, f_{RF} = 27.12 MHz). So the impacting particle flux onto the specimen consisted of thermal atomic deuterium (hydrogen) and ions, in addition to the D_2 (H_2) and He_2 gas.

The atomic deuterium (hydrogen) flux was determined to be $2.6 \pm 0.3 \times 10^{21}$ $m^{-2}s^{-1}$, whereas the ionic part of the impacting particle flux was determined to be $5.2 \pm 0.5 \times 10^{20}$

$m^{-2}s^{-1}$, i.e. the atomic flux was ~5 times larger than the ionic flux [172,173]. All fluences were determined by multiplying these fluxes with the exposure time.

The energy of the atomic (also called thermal) deuterium was equivalent to the plasma temperature, ~650 K (~0.06 eV). The ionic (or also called energetic) deuterium usually gained an energy of 30 eV by biasing the specimen, except for one measurement, in which their energy was only 15 eV. The distribution of deuterium ions in the plasma consisted of D^+, which were the majority, D_3^+ (with an equivalent energy of 10 eV per *D*) and D_2^+ (15 eV per *D*), which were both in an amount a factor of 3-5 less than the D_3^+ ions.

The amount of impacting *He* ions was 100 times less than those of *D* ions, which is understandable by considering the differences of their ionisation energies (13.6 eV for hydrogen and 24.6 eV for helium). Due to this small amount, effects of *He* on the chemical erosion were neglected.

The carbon erosion yield was determined from the spectroscopically measured time-resolved $D\gamma$-line and *CD*- and C_2-bands, which monitor the *D*, CD_4, and C_2D_y fluxes, respectively. The time evolution describes the fluence dependence of the chemical erosion in relative units. At the beginning of the plasma exposure all plasma and wall parameters had to come to equilibrium. During this stabilisation phase, which took about half an hour, the corresponding erosion data could not be obtained. This fact causes that a possible fluence dependence of the yield in the first erosion stage might be hidden.

The determination of Y_{tot} averaged over the applied fluence was performed by weighing the specimens before and after the plasma exposure outside the vacuum chamber, and attributing the whole weight loss to carbon erosion. The results are shown in **Table 4.2**. These weight loss data were also used to scale the spectroscopic signals to carbon erosion yields. More details of the experimental set-up and the data analysis can be found in [172,173].

In order to evaluate the synergetic effect of the thermal atomic deuterium in presence of energetic ionic deuterium, the erosion yield defined as eroded carbon atoms per incident thermal + energetic deuterium (Y_{t+e}) and the yield defined as eroded carbon atoms per energetic deuterium only (Y_e) have been separately considered (see **Table 4.2**). Y_e will be compared with the total erosion yield measured at the high current ion source by mono-energetic ion beam, which is now called Y_i for avoiding confusions, as it has already been defined: eroded carbon atoms per incident deuterium ions. In addition, **Fig. 4.9** shows the evolution with deuterium fluence for some specimens.

Name	Ion energy (eV)	Specimen temperature (K)	Erosion yield Y_{t+e} (*C* / thermal + energetic *D*) (%)	Erosion yield Y_e (*C* / energetic *D*) (%)
EK98	30	300	0.79 (0.48 for H)	4.8 (2.9 for H)
R6650M	30	300	0.95	5.7
R6650M	30	500	1.1	6.4
HPG	30	500	0.63	3.8
C_{CEIT}	30	500	1.3	7.9
TiC4	15	300	0.33	2.0
RGTi91	30	300	0.76 (0.58 for H)	4.5 (3.5 for H)
C/SiC	30	300	0.44	2.7
VC4	30	500	1.3	7.9
WC4	30	500	0.62	3.7
WC4in	30	300	*3.6*	-
ZrC4	30	500	1.3	7.9

Table 4.2. Y_{tot} obtained for different specimens from deuterium plasma experiments by weight loss measurements considering only erosion of carbon. Data in parentheses correspond to Y_{tot} from hydrogen plasma experiments.

The specimen holder was actively cooled during almost all measurements to achieve *RT* (~300 K), which was the temperature chosen for most experiments. Without cooling the specimen heated up to about 500 K.

The results will firstly be shown for undoped graphites. For the fine-grain graphites (C_{CEIT} and R6650M, see **Table 4.2**), Y_e at ~500 K is increased by a factor of 1.5 to 2 compared to the already shown Y_i at *RT* (~4%, see **Fig. 4.2**). An small increase is expected due to the higher temperature, but an important part of the increase of the yield can be attributed to the synergetic effect of simultaneous impact of atomic and ionic deuterium. So for the flux ratio of atomic to ionic deuterium used, the erosion yield is at most doubled. The reported flux dependence of the carbon erosion yield by hydrogen [27] can be neglected for these measurements, because the deuterium flux of ~3 × 10^{21} $m^{-2}s^{-1}$ is just below the range where the yield starts to decrease.

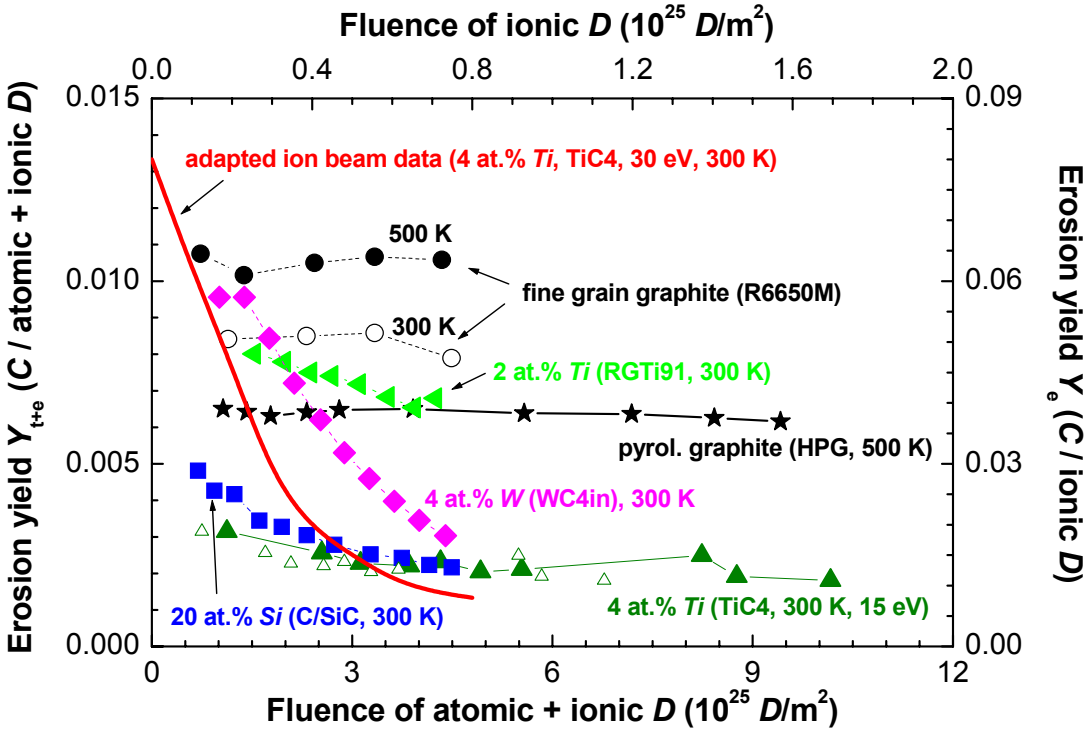

Fig. 4.9. Fluence dependence of the chemical erosion yield obtained by *RF* deuterium plasma exposure with an ionic deuterium energy of 30 eV. The erosion yield is given with respect to the ionic deuterium fluence only (axis on the top and on the right) and with respect to the sum of atomic and ionic deuterium fluence (axes on the bottom and on the left). For comparison, the data of the TiC4 eroded at 15 eV ionic deuterium are re-scaled to 30 eV (open triangles). The data of the TiC4 eroded with the deuterium ion beam are also adapted to the data obtained under atomic + ionic deuterium impact (thick red line) for comparison.

For the pyrolytic graphite with the basal planes almost parallel to the surface (HPG), no increase of the erosion yield Y_e compared to Y_i was found. A significant variation of the erosion yield with the type of carbon material was observed at ~500 K under plasma exposure with 30 eV ionic deuterium; e.g. Y_{t+e} was ~1.2% for two different fine-grain graphites (C_{CEIT} and R6650M) and, however, only 0.63% for pyrolytic graphite. These variations can be explained by the anisotropy of the erosion yield of the basal and prism plane of graphite [66] and by the amount of possible reaction sites for the atomic deuterium, both natural and ion-induced, in these materials. It should also be noted that the maximum of the chemical erosion for plasma exposure was found at temperatures around 800 K, while for ion beams it is already reached at 620 K due to the lower deuterium flux used [27].

For both, the fine-grain and the pyrolytic graphite, no fluence dependence of the erosion yield is observed, in accordance with the fluence dependencies shown for the fine-grain graphite produced at *CEIT* (C_{CEIT}) at *RT* and 620 K under deuterium ion beam impact (see **Fig. 4.4**).

Fig. 4.9 also shows the evolution of the erosion yield with the fluence for different doped carbon materials. The most pronounced fluence dependence by plasma exposure was measured for a *WC*-doped graphite (WC4in), which has a strongly inhomogeneous dopant distribution. The evolution of the erosion yield with the fluence is comparable to those observed by the deuterium ion beam (see **Fig. 4.2**). But the absolute calibration of the erosion yield by weight loss seems uncertain for this material because the weight loss data are too high and the spreading is too strong for the four specimens measured. The most reasonable explanation for this is that *WC* grains dropped off after exposure. So, the spectroscopically determined fluence dependence was scaled to an estimated total yield Y_{t+e} of 0.75% in **Fig. 4.9**.

For the 2 at.% *Ti*-doped graphite RGTi91, only a slow but steady reduction of the yield with the fluence is observed, which is expected due to the low dopant concentration and the large grain size of that material (see **Table 3.1**). The erosion yield of the C/SiC composite (some properties of this material are summarised in **Table 3.1**) changes with fluence from a faster decrease to a slower one at high fluences (~5 × 10^{25} *D*/m^2).

The erosion of the 4 at.% *Ti*-doped graphite TiC4 already reaches steady state after a fluence of ~3 × 10^{25} *D*/m^2. The carbon erosion necessary to create the dopant enrichment and the rough surface seems to have already taken place in the stabilisation phase of the plasma. This implies that the fluence during the stabilisation phase was higher than calculated, which is also indicated by the spectroscopic data. Therefore, the yield is overestimated for that exposure. Additionally, the fact that this material was eroded by the plasma at a deuterium ion energy of 15 eV instead of 30 eV has to be taken into account. It is observed that the erosion yield of pure graphite for 30 eV is increased by a factor of 1.5-2 compared with 15 eV deuterium [172,173]. The data for 15 eV impact are also plotted with re-scaled fluence in **Fig. 4.9** (factor 1.5).

For comparing the fluence dependencies by ion beam bombardment and plasma exposure, the fluence and the erosion yield axes of the ion beam data have been adapted. For this, the contribution of the atomic deuterium to the erosion of TiC4 has been equalled to the contribution by 30 eV deuterium ions only. Therefore, the fluence scale of ionic energetic deuterium was compressed by a factor of 2, while the ion beam yield axis was stretched by a factor of 2. The ion beam data of TiC4 are plotted with such an adaptation in **Fig. 4.9**. Even if for the plasma-exposed case only the steady state and not the decrease of the yield is observed, the results are in reasonable agreement with the ion beam results.

From the results shown in **Fig. 4.9** it can be concluded that the erosion yields for several carbon materials measured by ion beams and by plasma exposure are of the same order of magnitude and have the same evolution with fluence.

The **morphology** of the plasma eroded specimens was further investigated using *SEM* and compared with the morphology created after ion beam impact. **Fig. 4.10** shows examples of the surface morphology created on (**a**) a pure and (**b**) a *ZrC*-doped graphite after plasma exposure at fluences of several 10^{25} D/m^2. Even on pure graphite, a very rough morphology is created by the incident deuterium. The surface structure is more cotton-like and porous after plasma exposure, compared to those observed after ion beam bombardment. An explanation to this difference could be that the atomic deuterium from the plasma exposure slightly smears out the directional structure. But changes in the surface morphology of the pure graphites does not cause an observable fluence dependence of the erosion yield, as it has been shown in **Fig. 4.9**.

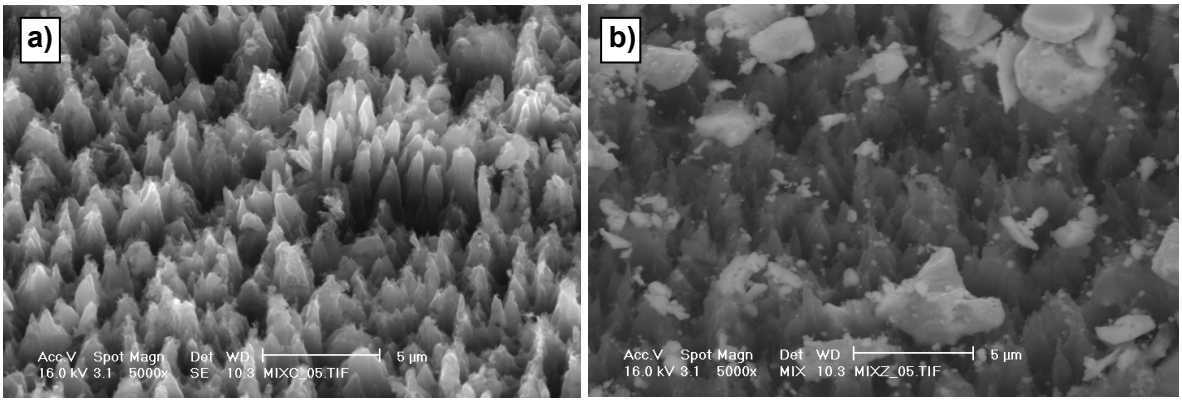

Fig. 4.10. *SEM* images of **a**) pure graphite C_{CEIT} after 6.8 × 10^{25} D/m^2 plasma exposure and **b**) *ZrC*-doped graphite with 4 at.% *Zr* (ZrC4) after 6.8 × 10^{25} D/m^2 plasma exposure at 500 K. The deuterium ionic part of the plasma had an energy of 30 eV.

The presence of dopant grains on the surface leads after erosion to the formation of needles with dopant grains on top, with only a slight undercut in the case of ion beam experiments, as shown in **Fig. 4.5**, emphasising the impacting direction of the deuterium ions. After plasma exposure, the surface is also strongly enriched with dopant grains, but additionally the dopant grains are strongly undercut (**Fig. 4.10 b**). Some of the grains seem to have nearly no contact to the region below the grains. The shielding of the graphite beneath the dopant grains is not as efficient as for pure deuterium ion impact, perhaps due to contribution of the atomic deuterium to the total erosion. This difference in the undercut could be explained by synergetic effects between atomic and ionic deuterium, but also by a possible disturbance of the electrical potential on the microscopic scale.

➔ San Diego: plasma simulator PISCES-B

PISCES-B is a plasma simulator located at the *University of California in San Diego* (*USCD*). Three *WC*-doped fine-grain graphite samples manufactured at *CEIT* with 4 at.% of *W* (WC19_1, WC19_2 and WC19_3) were sent there for the investigation of the fluence dependence and morphology changes created after exposure to deuterium plasma. This plasma simulator has the advantage of reaching higher ionic deuterium fluxes compared to the plasma simulator in Augsburg.

Each *WC*-doped graphite sample was exposed to different ion fluences while keeping the sample temperature at ~373 K or less. A sample bias of –50 V was used to accelerate ions into the sample, giving an effective ion impact energy of ~40 eV. Although this energy is slightly higher than the standard 30 eV used for the most experiments with ion beams and also with plasma impact in Augsburg, this energy was necessary to obtain a measurable *CD* band signal with the optical spectrometer in order to look at the fluence dependence of the chemical erosion yield. But a comparison of the data is certainly possible.

The plasma run parameters and calculated weight loss yields for each of the three samples are given in **Table 4.3**. Determination of the erosion yield was based on the assumption that the carbide grains do not erode significantly and that any undercutting of the graphite binder does not result in the loss of carbide grains from the surface, i.e. it was again assumed that only carbon erosion contributes to the weight loss.

Sample	Plasma				Sample				
	p (mtorr)	V_f (V)	T_e (eV)	N_e (cm^{-3})	T (K)	E_{ion} (eV)	Flux ($m^{-2}s^{-1}$)	Fluence (cm^{-2})	Y_{tot} (C/D_{ion})
WC19_1	4.0	-17	8±2	6×10^{11}	333±10	40±2	7.5×10^{21}	6.8×10^{24}	0.044
WC19_2	3.0	-12	6±2	1×10^{12}	353±10	44±2	1.1×10^{22}	5.2×10^{25}	0.018
WC19_3	5.0	-14	8±2	1×10^{12}	373±10	42±2	1.1×10^{22}	1.3×10^{26}	0.011

Table 4.3. Run plasma parameters and weight loss yields obtained for three similar WC-doped samples (WC19_1-3).

During the first two runs, instrumental problems made difficult the investigation by optical spectroscopy of the fluence dependence. But on the last run the optical spectroscopy technique was successfully used to investigate the fluence dependence of the chemical erosion from the *WC*-doped specimens. A fluence dependence also seems

to be apparent in PISCES, as **Fig. 4.11** shows. The data supplied show the integrated intensity of the *CD* band (normalised to the plasma $D\gamma$ line to remove influences due to plasma variation in time) with the *CD* band intensity far from the sample subtracted to correct for background wall erosion. After integrating along this plot, up to the 3 fluences that the samples were run to, seems to give relative values that relatively good agree with the trend in carbon yields measured by weight loss. These values are given in **Table 4.4**. The table also lists the surface composition of the samples determined using *energy dispersive X-ray spectroscopy* (*EDX*). For fluences of 5×10^{25} m^{-2} and higher, it appears that the surface is predominately the composition of the carbide dopant.

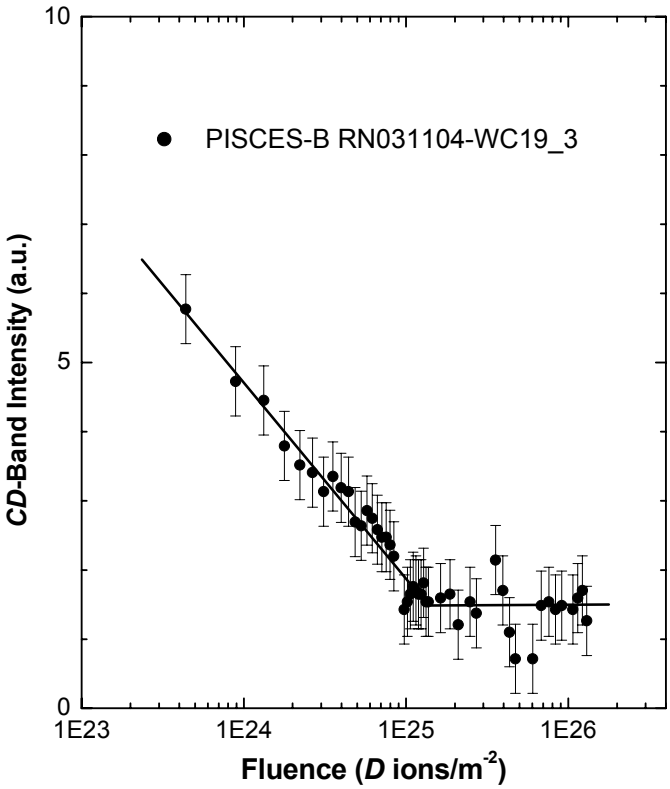

Fig. 4.11. Integrated *CD*-band emission in front of the target (normalised to $D\gamma$ and background corrected).

Sample	Y_{tot} weight loss (C/D_{ion})	Y_{tot} OES RN031104 (a.u.)	Surface composition (*EDX* analysis at 4 kV)		
			O	C	W
WC19_1	0.044±0.013	0.31	2	90	8
WC19_2	0.018±0.005	0.18	2	51	47
WC19_3	0.011±0.003	0.15	4	49	47

Table 4.4. Comparison of weight loss yield to spectroscopic observation of *CD* band during RN031104 and *EDX* analysis of sample surface.

SEM micrographs of **Fig. 4.12** show topographies very similar to those already observed under 30 eV mono-energetic ion bombardment (see **Fig. 4.5**). Images on the right are taken at an inclination of 30° to the electron beam for making possible the observation of needle structures. The low fluence exposed samples (see **Fig. 4.12 b** and **d**) clearly show the needle structure, while the highest fluence exposed sample (**Fig. 4.12 f**) does not; the graphite binder has been eroded deep into the sample in this case, leaving *WC* grains as the only visible structure.

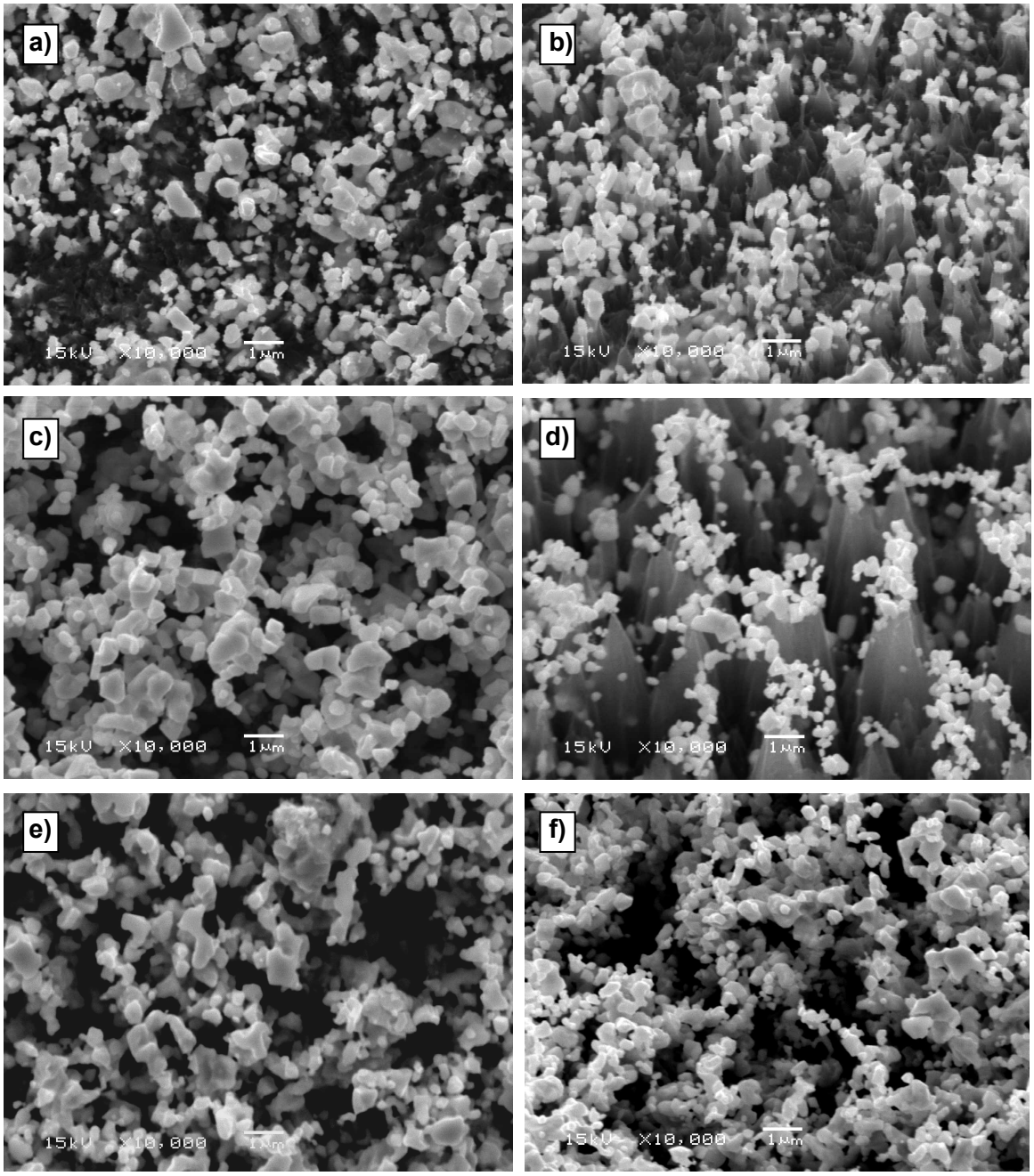

Fig. 4.12. *SEM* images of the *WC*-doped graphites after plasma exposure in PISCES. **a**) and **b**) WC19_1, fluence: 6.8×10^{24} cm^{-2}; **c**) and **d**) WC19_2, fluence: 5.2×10^{25} cm^{-2}; **e**) and **f**) WC19_3, fluence: 1.3×10^{26} cm^{-2}. All images on the right are tilted 30°.

Metal-doped nano-dispersed carbon films

In order to evaluate multi-component effects when dopants are nano-dispersed in the carbon structure, fluence dependence measurements at 30 eV deuterium ion impacting energy were also performed on some metal-doped nano-dispersed carbon films. With these materials, a fluence dependence of the erosion yield is also expected, but in a much smaller fluence scale than for the carbide-doped fine grain graphites.

The determination of Y_{tot} by weight loss measurements is in this case not feasible, because the films are very thin (some hundred nm); high accumulated fluences would lead to the erosion of the whole film thickness, and after low fluences, the weight loss is often smaller than the accuracy of the measurement. Another approach to evaluate the fluence dependence of Y_{tot} is to investigate the erosion products measured by *QMS*. This was used here.

As an example, **Fig. 4.13** shows for three different fluence scales the fluence dependence of the CD_4-production rate at 620 K of a 10 at.% *Ti*-doped *a-C:H* film produced at the University of Greifswald.

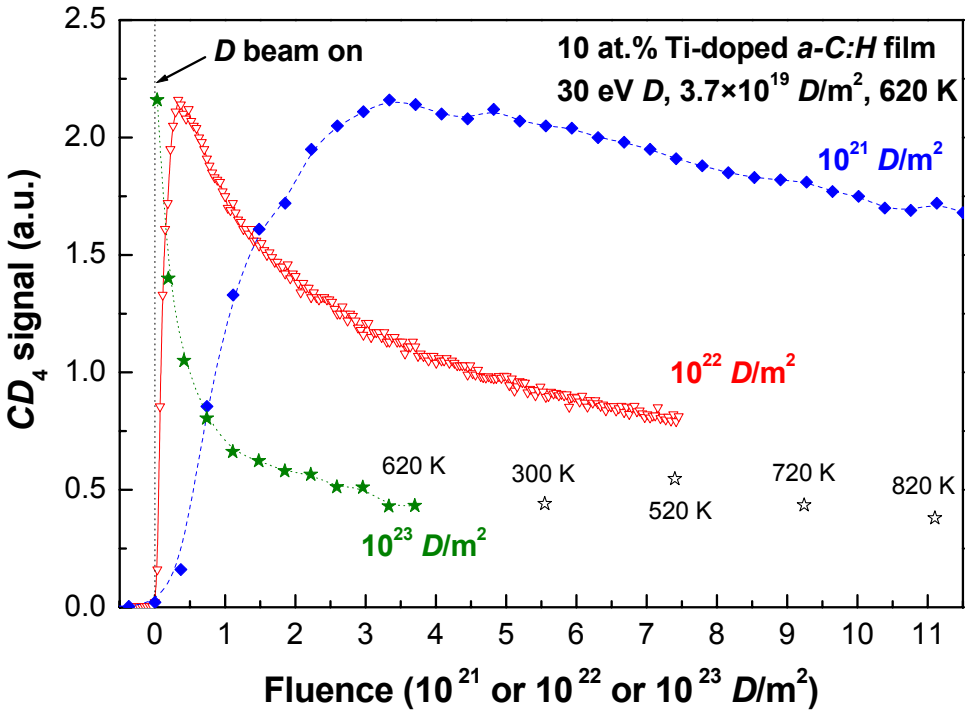

Fig. 4.13. CD_4-production vs. fluence of a 10 at.% *Ti*-doped *a-C:H* film eroded at 620 K with 3.7×10^{19} D/m^2s of 30 eV. The same data are shown for three different fluence scales. At the highest fluences the temperature was changed as labelled.

The increasing CD_4 signal at very low fluences (below 3×10^{21} D/m^2) can be explained due to a delayed CD_4-production until the precursor for the hydrocarbon emission is formed [174,175]. Beyond fluences of 3×10^{21} D/m^2, the production of CD_4 molecules decreases and by ~4×10^{22} D/m^2 the rate falls to 50% of the maximum amount. A further decrease of the CD_4 signal is observed after the highest applied fluence of 4×10^{23} D/m^2.

For comparison, the bombardment was interrupted on one occasion after a fluence of 7.4×10^{22} D/m^2 in order to try to determine the averaged Y_{tot} by weight loss measurement,. Although with a considerable error, Y_{tot} could be measured to 2.5 ± 1.5%. After higher fluences Y_{tot} could not be determined by weight loss, because the mass loss had decreased below the detection limit (± 1 µg).

Fig. 4.13 also shows the temperature dependence of the CD_4-production at even higher fluences (data represented with black stars). Nearly no variation of the CD_4 signal with temperature is observed after these high fluences.

Similarly to the fluence dependence of Y_{tot} observed for the carbide-doped fine-grain graphites, an enrichment of *Ti* at the surface of the thin film could explain the drop of the CD_4-signal with the fluence. In order to prove this, the averaged composition of this film and its surface composition inside and outside the erosion spot were measured by *XPS*. In fact, *Ti* was enriched at the surface due to preferential erosion of carbon to a value of 0.44 *Ti* atoms per *C* atom after a fluence of 1.1×10^{24} D/m^2. About 20% of the *Ti* atoms were detected in form of carbides inside the erosion spot, whereas they were only a few percent outside the erosion spot. The largest amount of *Ti* was metallic or oxidised, due to the absorption of oxygen and oxidation when the film was translated from the vacuum chamber, where the erosion measurements were performed, to the *XPS* apparatus.

After these results it can be concluded that *Ti* enrichment at the surface is associated to the observed diminution of the CD_4-production, which was reduced by a factor of less than a fourth of the maximum rate.

Conclusion to the fluence dependence measurements

The surface regime of the chemical erosion of carbon, Y_{surf}, is not chemically affected by doping. However, preferential erosion of carbon and the resulting enrichment of dopant on the surface leads to a very strong reduction of the net erosion of carbon, which will be the faster reached, the finer distributed and smaller the dopants are. A development of a strong surface topography is always expected.

4.1.3. Temperature dependence measurements

In order to study the chemical influence of doping on Y_{therm}, temperature dependence measurements were performed under 30 eV and 1keV deuterium bombardment. Y_{CD4} was determined with a *QMS* as a method to qualitatively measure Y_{therm} (for a quantitative determination of Y_{therm} the contribution to the yield of other chemical species would also have to be taken into account, as it has already been explain in the sub-section 3.2.4).

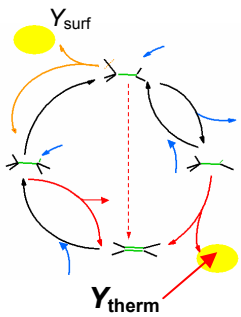

The experiments started at *RT*; thus for each measurement performed at 30 eV deuterium impacting energy (see sub-section 3.2.4), the first data point of Y_{CD4} corresponds to the surface regime of the chemical erosion, Y_{surf}.

The contribution of the surface enrichment of dopants to the reduction of Y_{CD4} can be neglected in the experiments performed on the carbide-doped fine-grain graphites, due to the low fluences required for measuring (usually below ~5×10^{23} D/m^2). However, on the nano-dispersed doped films enrichment is expected to be developed after shorter fluences, due to their much finer structure. For that reason, a possible enrichment of dopant on the surface was controlled by comparing two data of Y_{CD4} measured at the same temperature (*RT*), but at different times: firstly at the beginning, when the film still has a fresh surface, and again at the end of the erosion experiment, after the cooling-down phase.

The obtained results regarding the influence of dopants on Y_{therm} will be shown separately for the two kind of materials investigated: firstly for the carbide-doped fine-grain graphites from *CEIT*, and subsequently for the metal-doped nano-dispersed films. The second part will be longer due to the importance of the results obtained.

Carbide-doped fine-grain graphites

Prior to the temperature dependence experiments of the carbide-doped fine-grain graphites, the effects of **radiation damage** by energetic deuterium ion impact were investigated. The aim was to evaluate how much the pre-irradiation history affects, and also whether the graphitic structure after a certain pre-irradiation history can be restored by heating or not.

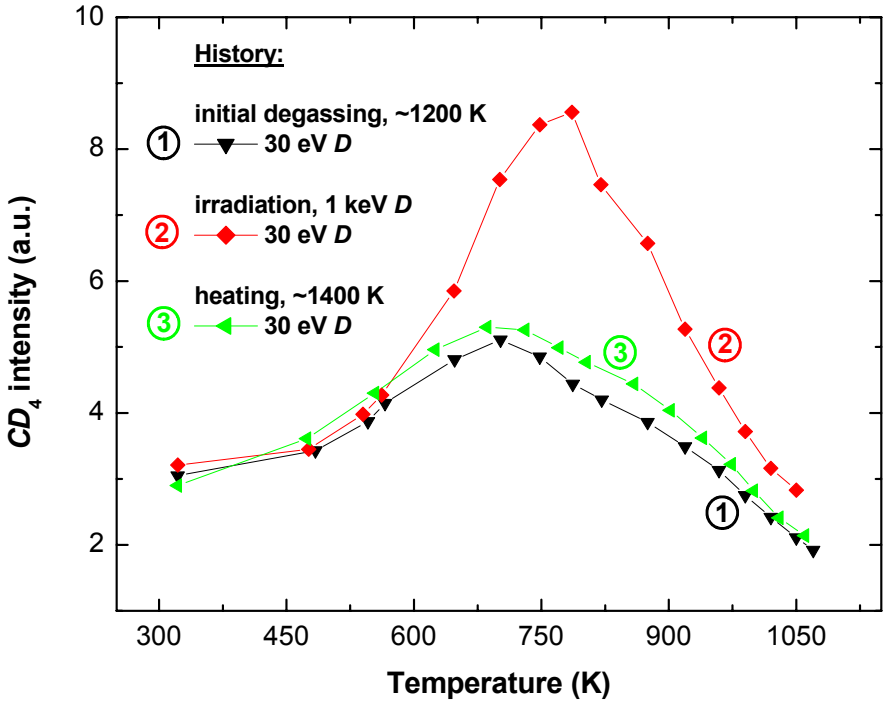

Fig. 4.14. Comparison of the CD_4 signal measured for the pure fine-grain graphite from *CEIT* C2350 under 30 eV deuterium impact energy, ① with polished surface and after degassing at ~1200 K (black); ② pre-irradiated surface at ~800 K and 1 keV deuterium impact energy, fluence ~8.8×10^{23} D/m^2 (red); and ③ after heating up to ~1400 K (green).

Fig. 4.14 shows the results of three sequentially measured temperature dependencies at 30 eV deuterium impact of a pure graphite specimen with the background contribution already subtracted. The first was measured on the initial degassed specimen. The second was performed after irradiation with high energetic deuterium ions, without pre-heating at ~1200 K in between. Finally, a third measurement was repeated with the same deuterium impacting energy but after heating at ~1400 K. The intensity of the mass 20 (corresponding to CD_4) was evaluated with *QMS*.

The CD_4 signal is at least 60% higher when the sample has been pre-eroded at 1 keV deuterium impact at around 800 K. It has to be noted that the maximum of the yield shifts to higher temperatures (T_{max}~800 K) due to the pre-irradiation. This fact corroborates that surface damage has to be taken into account. After heating at 1400 K, the damage nearly disappears.

As aforementioned in sub-section 2.1.2 about surface damage, when energetic hydrogen ions penetrate during bombardment into the graphitic structure, they are slowed down, leaving broken carbon bonds and imperfections, which are new active sites for successive reactions with the incoming hydrogen. The penetration range of the deuterium

ions into the surface is correlated to their energy [104], so the damaged surface layer is thicker, for higher impacting energy of the ions.

Consequently, in order to avoid effects of the pre-irradiation history, temperature dependence experiments were carried out on new polished samples which were always degassed at ~1200 K. This temperature has been proved to be sufficient for new samples.

Fig. 4.15 shows the **temperature dependence** of the Y_{CD4} of pyrolytic graphite and carbide-doped fine-grain graphites, corresponding to 4 at.% *Ti*, *V* and *W* **a**) for 1 keV and **b**) 30 eV deuterium bombardment.

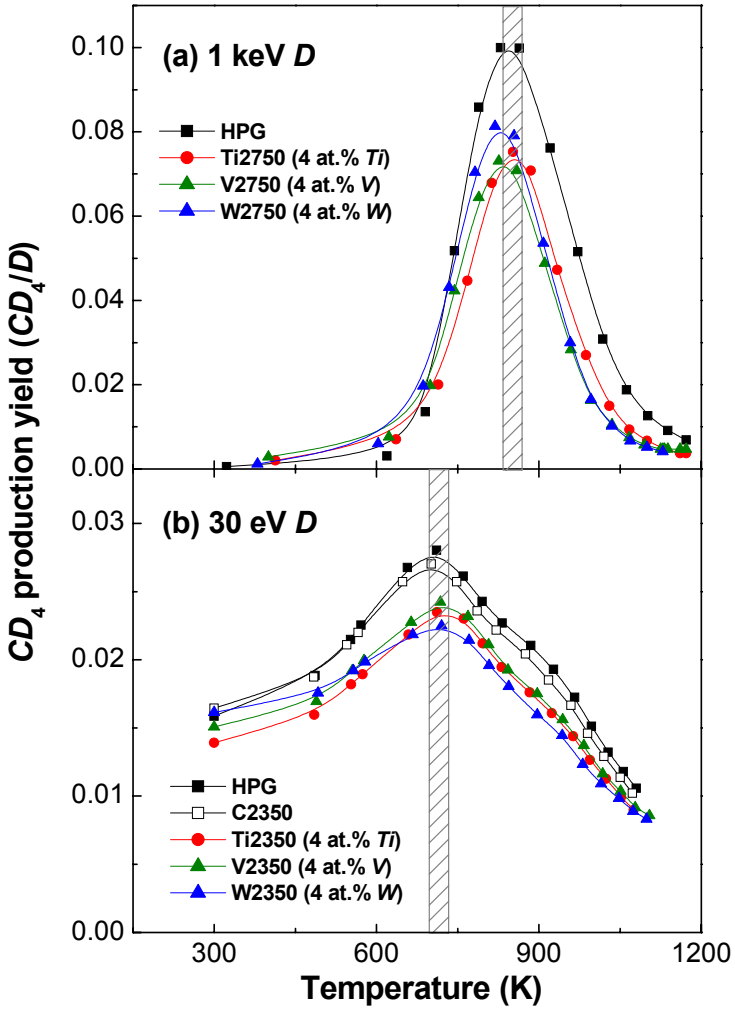

Fig. 4.15. Temperature dependence of Y_{CD4} of pyrolytic graphite and carbide-doped fine-grain graphites with 4 at.% *Ti*, *V* and *W* on the bulk for **a**) 1 keV and **b**) 30 eV *D* bombardment. All samples were not pre-irradiated and the accumulated ion fluences during the measurements were always below 2.5×10^{23} *D*/m^2.

A reduction of about 25% of Y_{CD4} at the same temperature of maximum erosion, T_{max}, with respect to pure graphite is observed for the doped graphites under both deuterium impacting energies. Additionally, a shift of T_{max} is perceptible from around 825 K to above 700 K by decreasing the deuterium impact energy from 1 keV to 30 eV. Such a shift was

already reported [59,168]. As an explanation to this behaviour, B.V. Mech *et al.* [168] suggest that kinetic processes associated with the energetic particles delay the thermal release of hydrogen, i.e. T_{max} increases with increase of impact energy.

Conclusion

A reduction of Y_{CD4} at T_{max} has been observed when graphite is doped with metal carbides. This reduction, of ~25% compared to pure graphite, cannot be explained by a simple geometrical shielding and enrichment of the carbides at the surface, because accumulated fluences were not high enough for this, and even the amount of dopant at the surface layer was depleted after the polishing (see **Table 3.2** for details of each sample). The same reduction has already been observed at low fluences by the fluence dependence measurement performed at ~620K shown in **Fig. 4.4** (see also sub-section 4.1.2). So the thermally activated regime of the chemical erosion of carbon, Y_{therm} is chemically influenced by doping.

Metal-doped nano-dispersed carbon films

Due to the stronger expected reduction of the chemical erosion, the smaller and finer distributed the dopants are, temperature dependence measurements were also performed on the metal-doped nano-dispersed carbon films.

In this sub-section, the results will be chronologically shown in order to facilitate their understanding. To begin with, first results obtained on the few *Ti*- and *Mo*-doped *a-C:H* films produced in Greifswald will be presented. Some questions arose after the realization of these experiments. To answer them, temperature dependence measurements were performed on doped *a-C* films especially produced with this aim at *IPP-Garching*. Experiments were even carried out at temperatures below *RT*. In the second part of this sub-section these results will be exposed and the questions will be answered.

a) First results: a-C:H films from Greifswald

Temperature dependence experiments were performed on three fresh *a-C:H* films doped with 10-13 at.% *Ti* and on an additional *a-C:H* thin film containing 50% *Mo*. The temperature dependence of Y_{CD4} was predominantly investigated, as well as the CD_3

production (mass 18). The films were continuously bombarded with fluxes in the range of 7.1-8.6×10^{19} *D*/m^2s and with deuterium impacting energy of 30 eV, while the temperature was increased in steps.

To illustrate this, **Fig. 4.16** shows the time evolution of the temperature and the mass spectrometer signals of mass 18 and 20 for a 10 at.% *Ti*-doped *a-C:H* film.

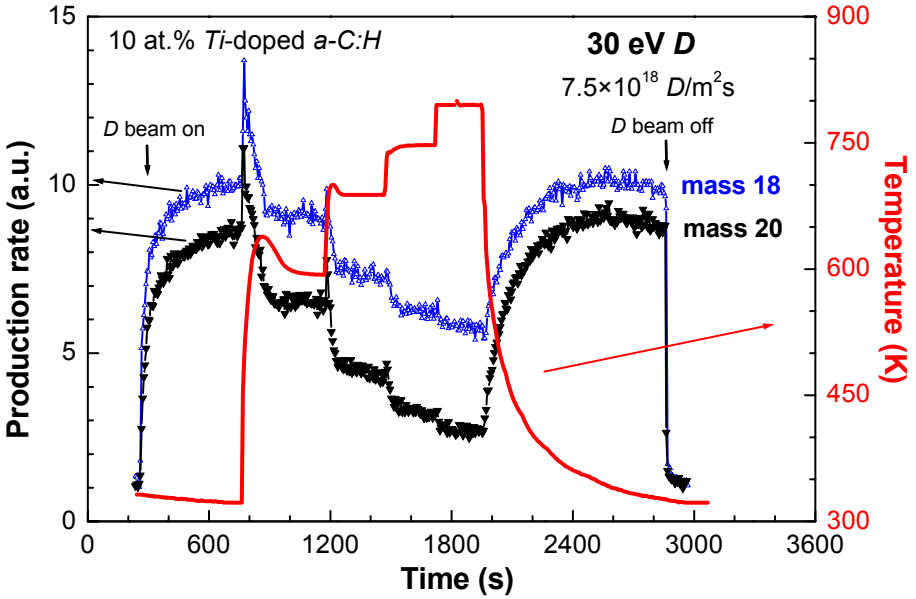

Fig. 4.16. Temperature evolution and time-resolved mass spectrometer signals of mass 18 and 20 of a 10 at.% *Ti*-doped *a-C:H* film.

Directly after changing the temperature, transient peaks in the emission of CD_4 are observed, as it has been explained in sub-section 3.2.4. Each temperature step was held until the signals of the masses 18 and 20 were nearly constant. The erosion yields derived from mass 20 (Y_{CD4}) are plotted in **Fig. 4.17** after background correction as a function of the temperature. For comparison, data for pyrolytic graphite from *UC* (HPG) and for a *TiC*-doped fine-grain graphite with 4 at.% *Ti* from *CEIT* (Ti2750) are inserted.

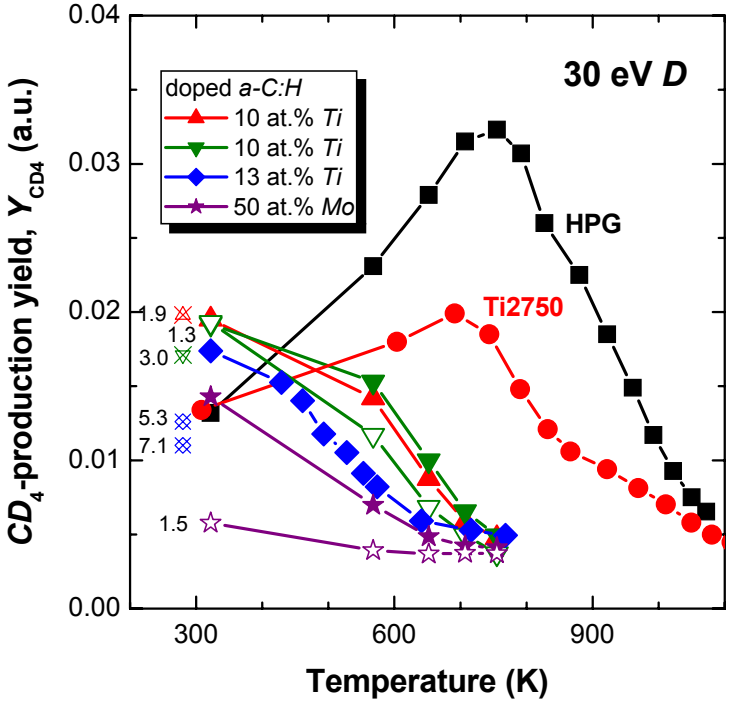

Fig. 4.17. Comparison of CD_4-production yield, Y_{CD4} vs. specimen temperature for four thin films, pyrolytic graphite and a ~4 at.% *TiC*-doped graphite from *CEIT* (Ti2750). Open and crossed symbols indicate data of a second repeated measurement as well as data after cooling down to *RT* (displaced to 250 K in the figure). The accumulated fluences are labelled in 10^{22} *D*/m^2. The used fluxes were between 7.1 and 8.6×10^{18} *D*/m^{2}s. All films were degassed before the measurements at ~1200 K for times above 10 minutes.

Two similar 10 at.% *Ti*-doped *a-C:H* films show the same steadily decreasing Y_{CD4} with temperature, which indicates a very strong reduction of the chemical erosion at elevated temperatures compared to pyrolytic graphite. This behaviour is only slightly affected by enrichment, as demonstrated by the fact that about the same CD_4-production is obtained after the cooling down phase, when returning to *RT* (see **Fig. 4.16**). Furthermore, a similar temperature dependence is observed by repeating this experiment with one of these pre-bombarded films (**Fig. 4.17**, open triangles), which would have been impossible to reproduce if important *Ti* enrichment had occurred.

The programme controlling the temperature ramp was modified in order to get more intermediate temperatures and corresponding data between 300 and 550 K. The aim was to look for a possible maximum of the CD_4 signal between this temperature range. After that, a temperature dependence experiment was performed on the 13 at.% *Ti*-doped film (see **Fig. 4.17**). Due to the increment of the number of temperature steps at low temperatures, higher fluences than generally used were accumulated. Besides, the measurement was continued after cooling down to *RT* in order to check whether the

fluence dependence observed in **Fig. 4.13** was also noticeable. The results again show that Y_{CD4} decreases monotonically with temperature, and no maximum is observed. After a fluence of 5.3×10^{22} *D*/m^2 the target has been cooled down to *RT* and Y_{CD4} is reduced by about 15% compared to the first measurement at *RT*. The rate is decreased further by 5% at the final accumulated fluence of 7.1×10^{22} *D*/m^2. Therefore, on this 13 at.% *Ti*-doped film the temperature dependence of the Y_{CD4} is already influenced by *Ti* enrichment. To illustrate this, the yields after cooling down to *RT* have been inserted in **Fig. 4.17** with crossed symbols.

An *a-C:H* film containing 50% *Mo* was also investigated with a stepwise increasing temperature. A strong reduction of the production of CD_4 is observed on this film when the temperature increases (**Fig. 4.17**). But the concentration of *Mo* rapidly increased on the surface, as the difference of the repeated second measurement (open stars) indicates and as it has been proved by *XPS* measurements, so enrichment has strongly influenced the temperature dependence of Y_{CD4}.

Due to the correlation of the background corrected signal of mass 20 with CD_4 molecules, and of the signal of mass 18 with emitted CD_3 radicals, the ratio of CD_3 to CD_4 can be investigated through the mass 18 to mass 20 ratio. This ratio has been investigated and the results are shown in **Fig. 4.18**. Due to the uncertainties in the background correction, ratios calculated from small mass signals are specially marked. The ratio changes with temperature, but with a contrary dependence as reported for simultaneous incident of thermal H^0 and energetic *Ar* ions [176]. If the CD_3 comes only from CD_4 cracking, a ratio of ~0.8 with a slight increase with the thermal energy of the particles should occur [177], but this increase is not strong enough to explain all the observed growth of the ratio with temperature. Remarkable is that the ratio at elevated temperatures is always larger for the doped films than for the pure graphites. On the graphite under 30 eV and 1 keV deuterium bombardment the ratio shows a minimum at the temperature of the maximum erosion yield (**Fig. 4.18**, arrows). From the study of this ratio it can be concluded that more CD_3 radicals are emitted at elevated temperatures and this increase is even stronger for the doped *a-C:H* films

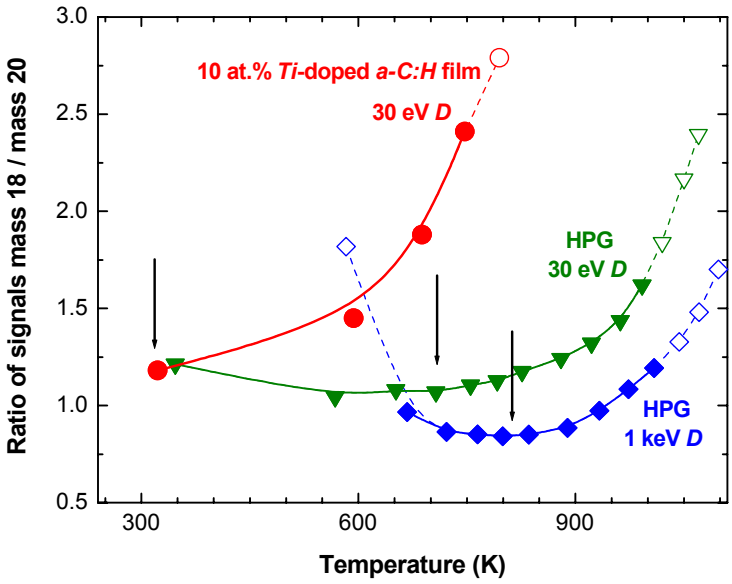

Fig. 4.18. Ratio of the *QMS* mass signals 18 to 20 vs. temperature. The arrows mark the temperature of the maximum in the observed yields. Open symbols with the respective dashed lines indicate ratios obtained from small mass signals compared to the background.

The mass signals of C_2D_y species have not been shown because they were small and partly covered by the contribution of *CO*. These signals increased with temperature but without correlation to the stepwise increasing temperature, and transient peaks were also not observed on them when the temperature changed.

➔ Discussion

Y_{therm} of nano-dispersed *Ti*-doped *a-C:H* layers was investigated in the temperature range 300 K to 800 K under 30 eV deuterium bombardment. Y_{CD4} decreases monotonically for temperatures just above *RT*. The strong reduction of the chemical erosion yield measured by Y_{CD4} at elevated temperatures compared to pyrolytic graphite may be attributed to a reduction of the *activation energy for hydrogen release*, E_{Hrel}, as in the case of *B*-doped graphites (already illustrated in **Fig. 2.5**). Two questions still arise: i) Does a maximum in the CD_4 emission around *RT* exist (**Fig. 4.19 a**) or not (**Fig. 4.19 b**)? ii) Is the increased CD_4 emission at *RT* correlated with an increased of Y_{surf} or is it just an artefact of the assumptions of the calibration?

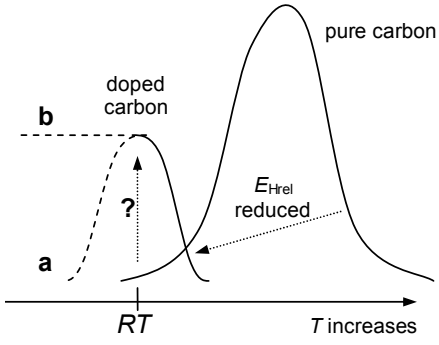

Fig. 4.19. Schematic illustration of the possible effects of nano-dispersed dopants on the thermally activated chemical erosion of carbon.

Measurements with finer temperature steps between *RT* and 550 K were done on a 13 at.% *Ti*-doped *a-C:H* film (**Fig. 4.17**), and no maximum was found above *RT*. Experiments with a cooled target below *RT* are required in order to separate the effect of the two erosion regimes, Y_{therm} and Y_{surf}. Such separation is not possible with the previously presented data.

The maximum Y_{CD4} of the doped *a-C:H* films, which is here observable at *RT*, is reduced by about a factor 2 compared to pyrolytic graphite but has about the same amount as for the 4 at.% *Ti*-doped graphite. Y_{CD4} at *RT* is enhanced compared to the graphites. This enhancement and the observed shift with temperature might also be explained in the frame of the model understanding of the thermally activated regime [27], whether not only E_{Hrel} for deuterium release is reduced due to the *Ti*-doping, like for *B*-doped graphites, but also for the thermal hydrocarbon release, E_{HCrel} (**Fig. 4.19 a**). Both activation energies should be strongly decreased from their best fitting values obtained for pyrolytic graphite (1.8 eV and 1.7 eV, respectively) to below 1 eV.

There were still reasons to have doubts about the increased CD_4 yield at *RT*. In the literature [72], data show that the starting carbon structure affects the yield, and even the effect of the irradiation damage shown in **Fig. 4.14** support the doubts. Definitely, the thin films and the pyrolytic graphite consist of carbon in different binding states, even if the differences are reduced due to the amorphisation and hydrogenation of the pyrolytic graphite by the ion bombardment [72]. The way to investigate this is through a comparison of the measurement not with pyrolytic graphite, but with a comparable undoped carbon film. For this aim, not only doped *a-C* films, but also pure *a-C* films were produced in a second phase at *IPP-Garching*. The results will be shown and discussed in the next sub-section.

Another reason was that the ratio between single carbon-containing species to heavier hydrocarbons (C_1D_z to $C_{x>1}D_y$) may be changed by the doping. This ratio is assumed to be constant for the calibration of Y_{CD4}. A hint for an influence of the doping on this ratio ($C_1D_z/C_{x>1}D_y$) gives the changed CD_3/CD_4 ratio for the doped films with temperature (**Fig. 4.18**). If the increased CD_4 yield is not taken into account, then only the E_{Hrel} must be reduced from 1.8 eV for pyrolytic graphite to 0.9 eV, which is even further than for the boron-doped graphite (1.2 eV).

Concluding after these first measurements, nano-dispersed metal-doped films of this type resulted to be excellent test materials for fundamental investigations. Some questions arose during the analysis of the results showed for them. Therefore, the

influence of different dopants on the processes of the chemical erosion and their impact in respect to their concentrations were further investigated with new doped *a-C* films.

b) Second phase: a-C films from IPP-Garching

➔ Chemical erosion below RT

In order to search for an answer to the question regarding the existence of a maximum in the CD_4 emission around *RT* for the doped thin films, erosion experiments were performed below 300 K. These measurements also tried to separate the possible effects of nano-dispersed doping on Y_{surf} and Y_{therm} at *RT*. *Ti*-doped *a-C* films were selected for the realisation of these measurements, as well as pyrolytic graphite and pure *a-C* film for comparison.

Y_{CD4} of pyrolytic graphite below *RT* was found to be equivalent to the yield at *RT*, behaviour not yet reported up to now. For the same pyrolytic graphite sample, a total erosion yield measured by weight loss of about 4.7% ± 1.5% was found after erosion at different temperatures below *RT* with 30 eV deuterium energy. The value of the yield is in accordance with the published total yields of pyrolytic graphite at *RT* with the same impact energy (30 eV deuterium) [46,59]. In conclusion, the erosion yield of pyrolytic graphite is temperature-independent below *RT*.

Y_{CD4} was also investigated at temperatures in the range between 77 and 300 K under 30 eV deuterium bombardment on a pure *a-C* film and three *Ti*-doped *a-C* films containing 2, 6.5 and 13 at.% *Ti*. To simplify the interpretation of the data, the same experimental results have been shown in two different ways: as a function of the ion fluence in **Fig. 4.20 a** and as a function of the target temperature in **Fig. 4.20 b**. At ion fluences above 10^{23} D/m^2, **Fig. 4.20 a** shows for the 13 at.% *Ti*-doped *a-C* film the strongest reduction of the yield, of around 75%, followed by the 6.5 at.% *Ti*-doped *a-C* film with a reduction of Y_{CD4} around 50% at analogous ion fluences. The 2 at.% *Ti*-doped *a-C* film shows an extremely weak fluence dependence and the pure *a-C* film does not present any change in Y_{CD4} if the ion fluence is varied.

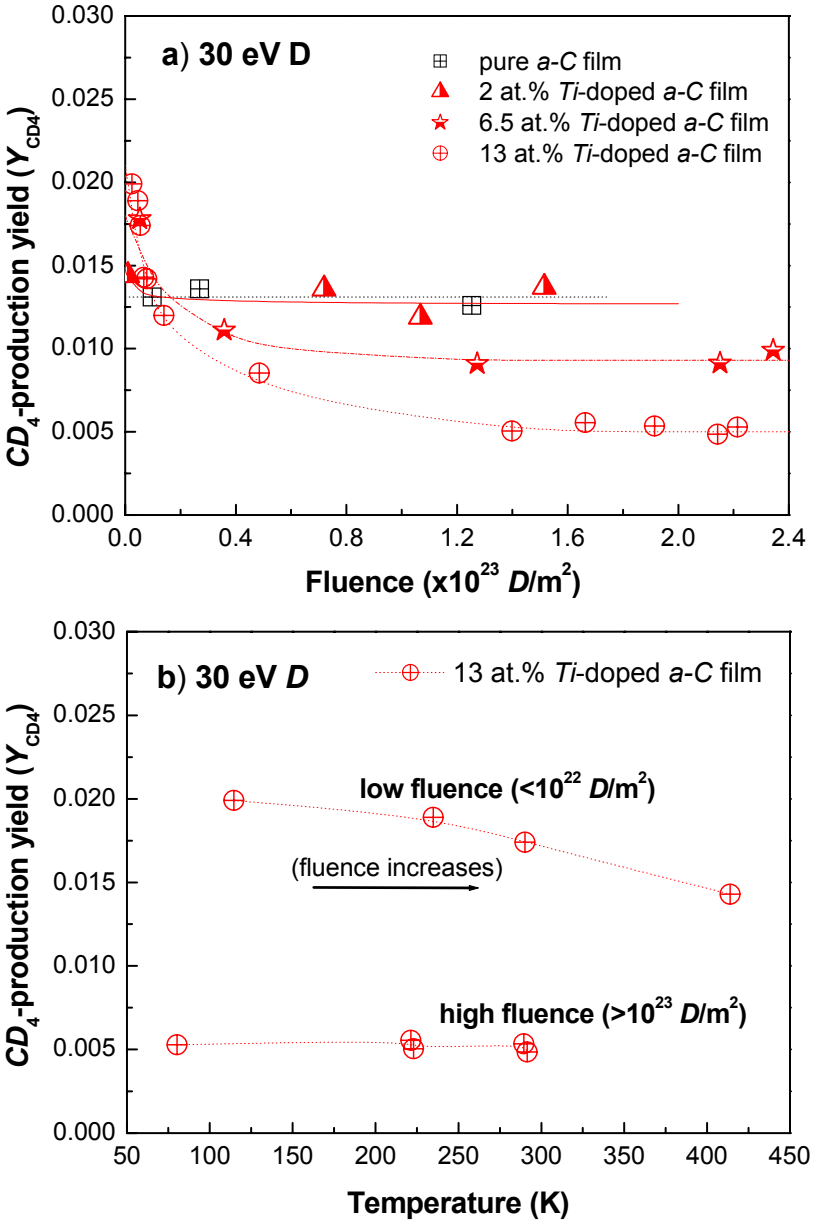

Fig. 4.20 a) Fluence dependence of Y_{CD4} for a pure *a-C* film and three different *Ti*-doped *a-C* films. The data were obtained at different temperatures. **b**) Temperature dependence of Y_{CD4} of a 13 at.% *Ti*-doped carbon film. Data for low ion fluences (<10^{22} *D*/m^2) and high ion fluences (>10^{23} *D*/m^2) are compared. The lines are only to guide the eye.

Fig. 4.20 b shows the temperature dependence of Y_{CD4} for two fluence regimes. At low ion fluences (<10^{22} *D*/m^2), the decrease with increasing temperature is most probably due to the increasing in ion fluence, as shown in **Fig. 4.20 a**. At high ion fluences (>10^{23} *D*/m^2), where the fluence dependence vanishes, no temperature dependence could be found.

These measurements clarify the discussion on the possibility of a maximum of the yield below *RT* for doped graphites. The new results do not show any decrease of Y_{CD4}

below *RT* compared to the yield at *RT*, i.e. no maximum could be found down to temperatures of 77 K. From these results it is possible to conclude how nano-dispersed *Ti*-doping drastically reduces the Y_{CD4} at high temperatures: *Ti* doping enhances the release of hydrogen as H_2 molecules, strongly reducing the activation energy of hydrogen release, E_{Hrel}.

Applying the analytical model for chemical erosion formulated by Roth and García-Rosales in [67] (improved in [27,178]) to the case of the 13 at.% *Ti*-doped *a-C* film, the activation energy for hydrogen release E_{Hrel} has to be reduced from about 1.8 eV (for pure graphite) to 0.9 eV.

Considering all things together, Y_{therm} is largely reduced by *Ti* doping; Y_{surf}, at least at low ion fluences (<10^{22} *D*/m^2 for *Ti*-doped *a-C* films; <10^{24} *D*/m^2 for carbide-doped fine-grain graphites), remains unchanged down to temperatures of 77 K for both types of investigated materials; but the contribution of Y_{surf} to the total erosion yield is strongly reduced by dopant enrichment at high ion fluences (>10^{23} *D*/m^2 for *Ti*-doped *a-C* films; >10^{25} *D*/m^2 for carbide-doped fine-grain graphites). This enrichment is reached faster for homogeneous nano-distribution of metal.

The enrichment of *Ti* on the surface of the eroded thin films was confirmed by *RBS* analysis of 800 keV ^{4}*He*. An example of this is shown in **Fig. 4.21**.

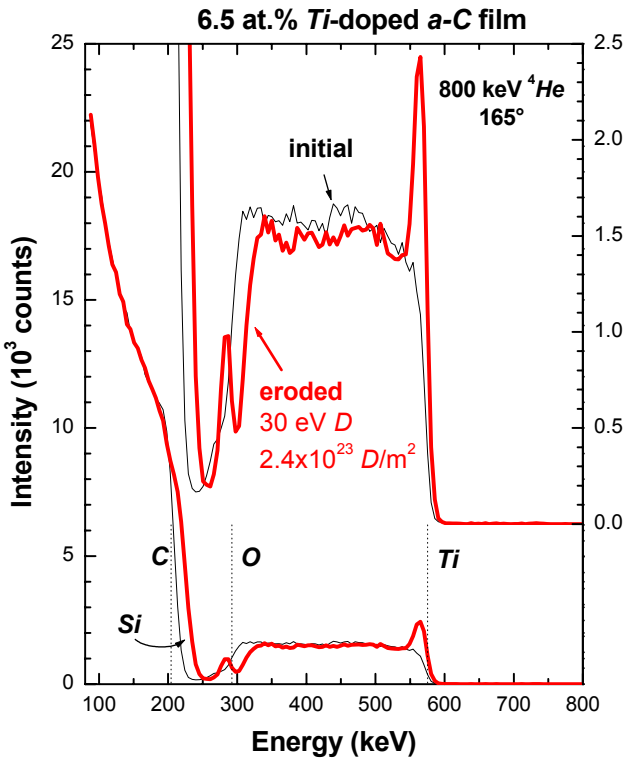

Fig. 4.21. *RBS* spectra of 800 keV ^{4}*He* on the 6.5 at.% *Ti*-doped *a-C* film before (black) and after erosion under 30 eV deuterium ions (red). The accumulated fluence was 2.4×10^{23} *D*/m^2.

Two important differences stand out in **Fig. 4.21**: a prominent peak in the *Ti* signal appears just at the very surface of the film; and a new peak corresponding to *O* has also emerged, i.e. the concentration of *Ti* has risen at the surface of the film due to the preferential erosion of *C* and then oxidised. Oxidation of *Ti* occurs after the remove of this enriched film from the vacuum chamber and the direct contact of *Ti* metal with *O* present in the atmosphere.

Until now, Y_{CD4} has been studied in order to investigate the influence of doping on Y_{therm}. *RBS* technique also gives the possibility to calculate the net carbon loss, i.e. Y_{tot}. This can be done by integrating and subtracting the carbon peaks after and before erosion, because the area underneath the individual curves in the spectrum represents the amount of that element. So in this way, for the 6.5 at.% *Ti*-doped *a-C* film, Y_{tot} was determined to be 1.5% ± 0.5%.

When Y_{tot} and Y_{CD4} are both known, it is possible to calculate approximately the contribution of the eroded CD_4 molecules and the CD_3 radicals to the total erosion and to estimate the contribution of the heavier hydrocarbons to the yield. This was not possible to determine only with *QMS* analysis. So Y_{tot} calculated by *RBS* is about half of the yield reported under the same energy at *RT* for pure carbon [46], and more than the half of the eroded carbon atoms were detected as CD_4. In a previous study performed on pure carbons [59], only a quarter of the total eroded carbon was found in form of CD_4.

With these results it can be concluded that the amount of heavier hydrocarbons and of high sticking erosion species produced have been reduced by the presence of the metal dopant. Therefore, the increased CD_4 emission at *RT* is just an artefact of the assumption of the calibration, which does not take into account variations in the ratios of radicals to molecules and C_1D_z to heavier hydrocarbons, $C_{x>1}D_y$ due to the doping.

➔ Temperature dependence measurements above RT

Similar temperature dependence measurements to those performed on the *a-C:H* doped layers from Greifswald were performed on the *a-C* layers produced at *IPP-Garching*. The main results are summarised in **Fig. 4.22**, which also contents the already shown results obtained below *RT* and the results obtained for the *a-C:H* films from Greifswald. The *a-C* layers were doped with different concentrations of *V*, *Ti* and *W*, as indicated in **Fig. 4.22 a**, **b** and **c**, respectively. For comparison with the doped films, data of a pure *a-C* film and pyrolytic graphite are inserted. The yield of pure graphite exhibits the well-known maximum in the temperature dependence [59,67,72].

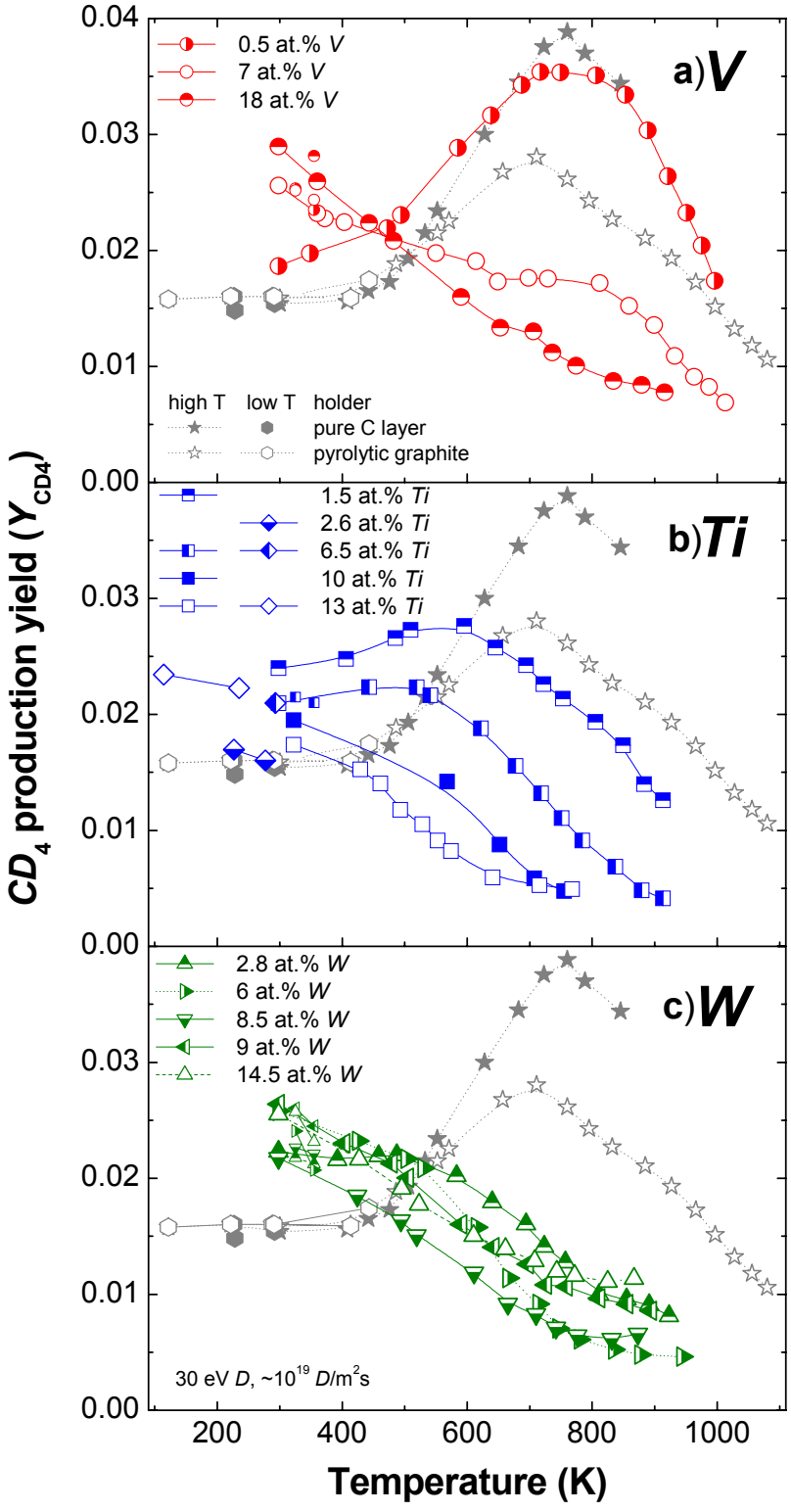

Fig. 4.22. Y_{CD4} of *a-C* films doped with **a**) *V*, **b**) *Ti* and **c**) *W* vs. specimen temperature during deuterium ion bombardment with 30 eV and a flux of ~10^{19} *D*/m^{2}s. The accumulated fluence, which increases with temperature, was always less than 10^{23} *D*/m^2 (mostly less than 5×10^{22} *D*/m^2) at the highest temperature. Yields after cooling down to nearly 300 K are given as small symbols. For comparison, data for pyrolytic graphite, a pure *a-C* film and the already shown *a-C:H* films doped with *Ti* are inserted.

The maximum Y_{CD4} corresponds to the pure *a-C* film, for which T_{max} is shifted about 50 K to higher temperatures compared to T_{max} for the graphites. This behaviour may be explained by the difference of carbon structures [179] between the graphitised carbon material and the disordered amorphous carbon film. In fact, the initial state of the carbon in the target influences the yield. The maximum Y_{CD4} of the carbon film is 30% larger than of the pyrolytic graphite and the fine-grain graphite, a behaviour comparable to the one observed on a pure graphite sample previously pre-eroded with energetic deuterium ions after 30 eV deuterium impact energy due to lattice damage and disorder (see **Fig. 4.14**).

All modifications of the temperature dependence by doping compared to pure carbon illustrated in **Fig. 4.22** can be summarised as: i) Y_{CD4} is increased at *RT* and ii) Y_{CD4} around T_{max} (~750 K) is strongly reduced. In the following the results will be separately analysed for each type of dopant.

For **vanadium-doped** films (**Fig. 4.22 a**), Y_{CD4} at *RT* increases with increasing the *V* concentration; nearly by a factor of 2 for 18 at.% *V*-doping. In contrast, the yield at higher temperatures, e.g. around 750 K, is drastically decreased in the same *V* concentration range (0.5-18 at.% *V*), and for about 6 at.% *V* the yield only steadily diminishes above *RT*.

The temperature dependence of the specimen with 7 at.% *V* shows a pronounced shoulder above 800 K. The signal of mass 19, e.g. CD_3H or *HDO*, exhibits a peak at the same temperature. Similar shoulders and peaks, but of smaller amount, are also visible in other data sets shown in **Fig. 4.22**. Whether these shoulders are in fact originated by erosion or are experimental artefacts is not clear.

For **titanium-doped** films, Y_{CD4} decreases with *Ti* concentration in the whole temperature range. Already for concentration above 7 at.% *Ti*, the maximum vanishes. The yield at *RT* shows the astonishing behaviour, that it jumps up by ~60% already for the lowest *Ti* concentration (1.5 at.% *Ti*) compared to pure carbon film.

For **tungsten-doped** films, such uniform description is not obvious from **Fig. 4.22**. The variation in the yields is smaller than for the other two dopants, even if the concentration range is the same for all three types of doping. For the lowest *W* concentration (2.8 at.% *W*), the maximum of Y_{CD4} above *RT* is already vanished.

To better examine the dependency on metal concentration, some data from **Fig. 4.22** have been plotted in **Fig. 4.23** against the bulk dopant concentration.

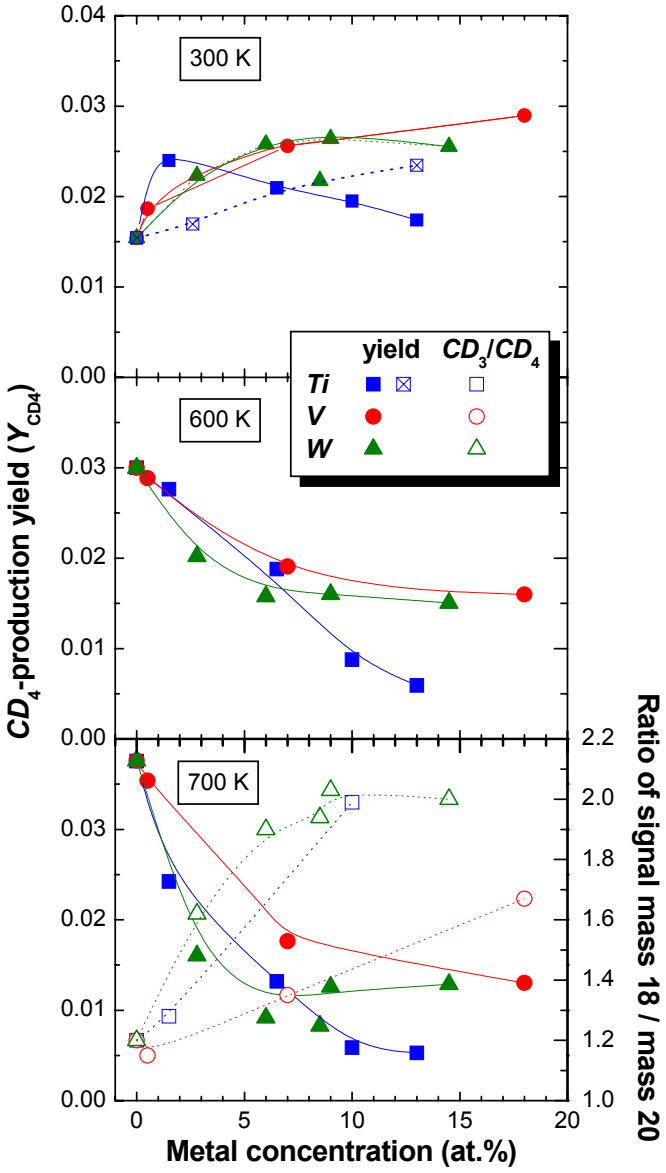

Fig. 4.23. Y_{CD4} at 300, 600 and 700 K (filled symbols) and ratio of the signals of mass 18 to mass 20 at 700 K (open symbols) of carbon films doped with *V*, *Ti* and *W* versus bulk metal concentration by 30 eV deuterium bombardment. The data at 300 K and 700 K have an accumulated fluence of less than 1 and 2×10^{23} D/m^2, respectively. Data of *Ti*-doped films measured below *RT* are also inserted (crossed symbols). The lines are only to guide the eyes.

At *RT*, the yield shows a maximum depending on the dopant concentration. The atomic concentration, for which Y_{CD4} is maximum, is below 1.5 at.%, around 10 at.% and above 18 at.% for *Ti*, *W* and *V*, respectively.

Data of *Ti*-doped films, which were measured below *RT* and were only pre-heated at 410 K, are also inserted in **Fig. 4.23**. The two sets of data showed for *Ti*-doping differ, even as thin film production and erosion measurement procedure were the same. But an important difference between both measurements was the pre-heating temperature, so

diverse thermally induced changes in the films could occur. Hints for such changes are given by results of *XRD*, where the crystallinity of the carbide grains was increased for *V*-, *Zr*- and *W*-doped films due to the thermal annealing at ~1200 K.

Around 600 K, Y_{CD4} continuously decreases with increasing the concentration for the three metals.

As previously discussed (**Fig. 4.18**), the ratio of the signals of masses 18 (CD_3) and 20 (CD_4) of *Ti*-doped films show deviating temperature dependencies compared to pyrolytic graphite. For pyrolytic graphite as well as for the pure *a-C* film, the ratio is nearly constant between *RT* and ~800 K. For all doped films, the ratio increases with temperature. In **Fig. 4.23** the ratio at 700 K is inserted. The increase depends on the dopant concentration. Doping with *W* exhibits the strongest one.

In order to avoid enrichment effects (as mentioned in **Fig. 4.13** and **Fig. 4.17**) the accumulated fluences for all measurements shown in **Fig. 4.22** were kept as low as possible: always below 10^{23} *D*/m^2 and for the most even below 5×10^{22} *D*/m^2. The effect of dopant enrichment was checked, as previously explained, by measuring the yield after cooling down to *RT*, as illustrated in **Fig. 4.24**.

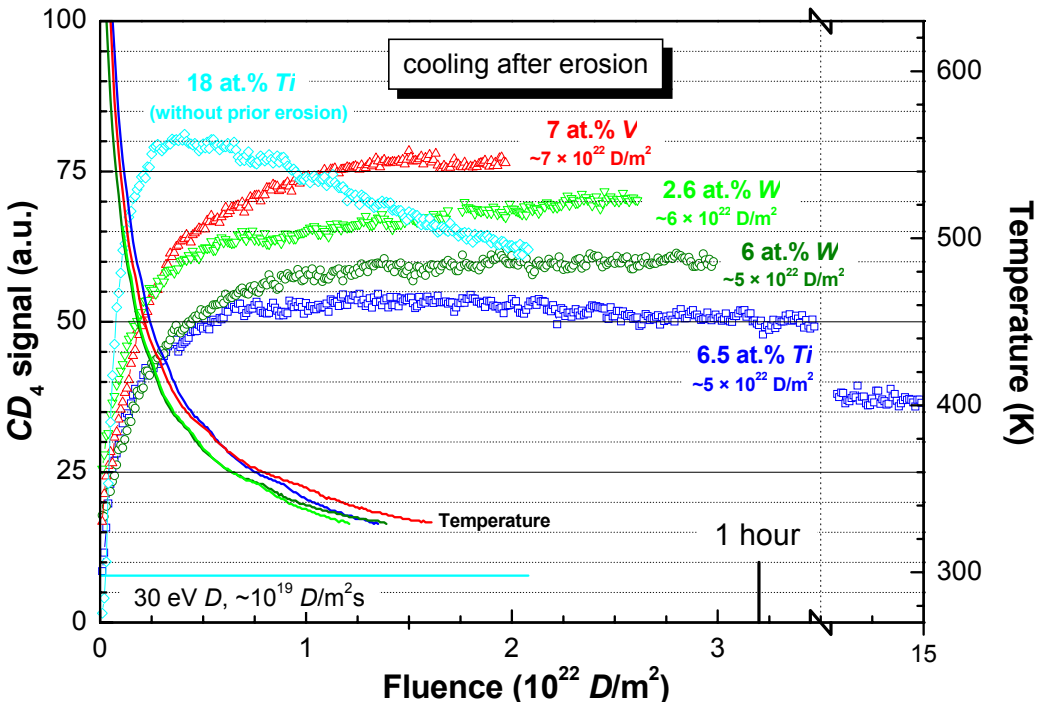

Fig. 4.24. Fluence dependence of mass 20 during the cooling down phase after a temperature dependence erosion experiment. These signals were used as indicator of a possible enrichment of the metals on the surface.

For the films doped with *W* and *V*, Y_{CD4} after the cooling down phase is not smaller compared to the starting values, but even slightly enhanced (<10%) and further increased after cooling (**Fig. 4.24**). For the *Ti*-doped film a slight reduction is observed. These observations possibly correspond just to changes in the ratios of the production species, i.e. the production of CD_4 is enhanced at the cost of a corresponding decrease in the production of heavier hydrocarbons.

Conclusion to the temperature dependence measurements

The temperature dependence of the Y_{CD4} was firstly investigated on carbide-doped fine-grain graphites. A reduction of Y_{CD4} at T_{max} of ~25% compared to pure graphite was observed. This reduction cannot be explained by a simple geometrical shielding and enrichment of the carbides at the surface. So the thermally activated regime of the chemical erosion of carbon, Y_{therm} is found to be chemically influenced by doping.

The temperature dependence of the Y_{CD4} was also investigated on nano-dispersed metal-doped carbon films containing *V*, *Ti* and *W* under bombardment with 30 eV deuterium ions. For all three metals, a strong reduction of Y_{CD4} compared to pure carbon at elevated temperatures is observed. The reduction depends on the metal concentration and the yield diminishes continuously above *RT* for 3 at.% *W*, 6 at.% *V* and 7 at.% *Ti*. This reduction of the Y_{CD4} at elevated temperatures can be explained by a decrease of the activation energy for the hydrogen release E_{Hrel} during ion impact of these dopants, as it was previously observed for *B*-doping [19,21,126]. It could be speculated that this lowered activation energy causes lower desorption temperatures for retained hydrogen in such doped carbon films. This is of high interest for the estimation of the tritium inventory in deposited mixed material.

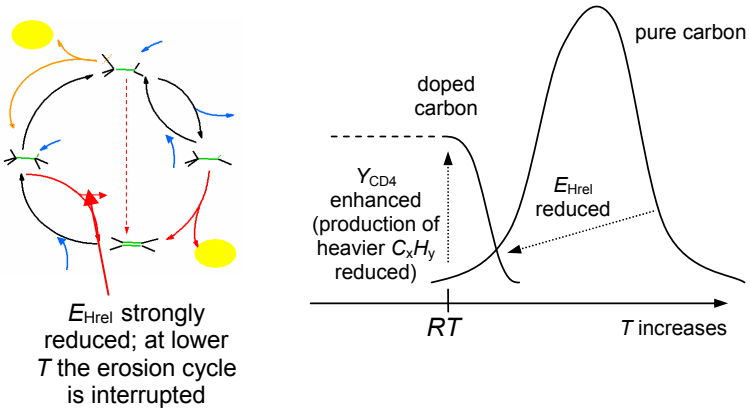

Fig. 4.25. Schematic summary of the effect of nano-dispersed dopants on the thermally activated chemical erosion of carbon.

Y_{CD4} for all doped films is enhanced at *RT* compared to pure carbon and shows a maximum depending on the metal concentration. This maximum is found at concentrations below 1.5 at%, around 10 at% and above 18 at% for *Ti*, *W* and *V*, respectively. The enhanced Y_{CD4} at *RT* implies changes of the distribution of the erosion products to an increased production of CD_4.

Fig. 4.25 summarises schematically the effect of nano-dispersed dopants on Y_{therm} of carbon.

4.2. Influence of dopants on the deuterium retention by implantation

In this second part of section 4, results of *thermal desorption spectroscopy* (*TDS*) measurements are summarised and compared with literature data for discussing the influence of dopants on the deuterium retention by implantation.

The addition of dopants to graphites seems to increase the deuterium retention [88,94,97]. A question still remains unsolved, whether the dopant itself causes this increase with deuterium fluence or it is only produced by changes in the micro- and nano-structure of the surrounding carbon due to the different manufacturing of these materials.

To solve this question, the influence of porosity and type of dopant (*TiC*, V_8C_7, *ZrC* and *WC*) on the deuterium retention implanted at *RT* with 1 keV were studied as a function of deuterium fluence by means of *TDS* for the carbide doped fine-grain graphites from *CEIT*. The samples investigated were graphitised at different temperatures, and had a concentration of metal of 4 at.%. **Fig. 4.26 a** shows the results for different pure graphites; **Fig. 4.26 b** presents all results for the doped specimens, and **Fig. 4.26 c** assembles similar data from the literature.

As shown in **Fig. 4.26 a**, a clear reduction of the deuterium retention is observed on undoped graphite that has been graphitised at temperatures ≥ 2370 K for fluences above 10^{21} D/m^2. In **Fig. 4.26 b** no difference is appreciated on the deuterium retention of all the doped graphites studied, irrespective of the type of dopant and porosity (note that doped graphites graphitised at 2620 K and at 3020 K have been measured; in the first case, the porosity was predominantly open, whereas in the second, almost completely closed, see sub-section 3.1.1). Moreover, the deuterium retention is the same for undoped graphitised graphite than for doped graphites.

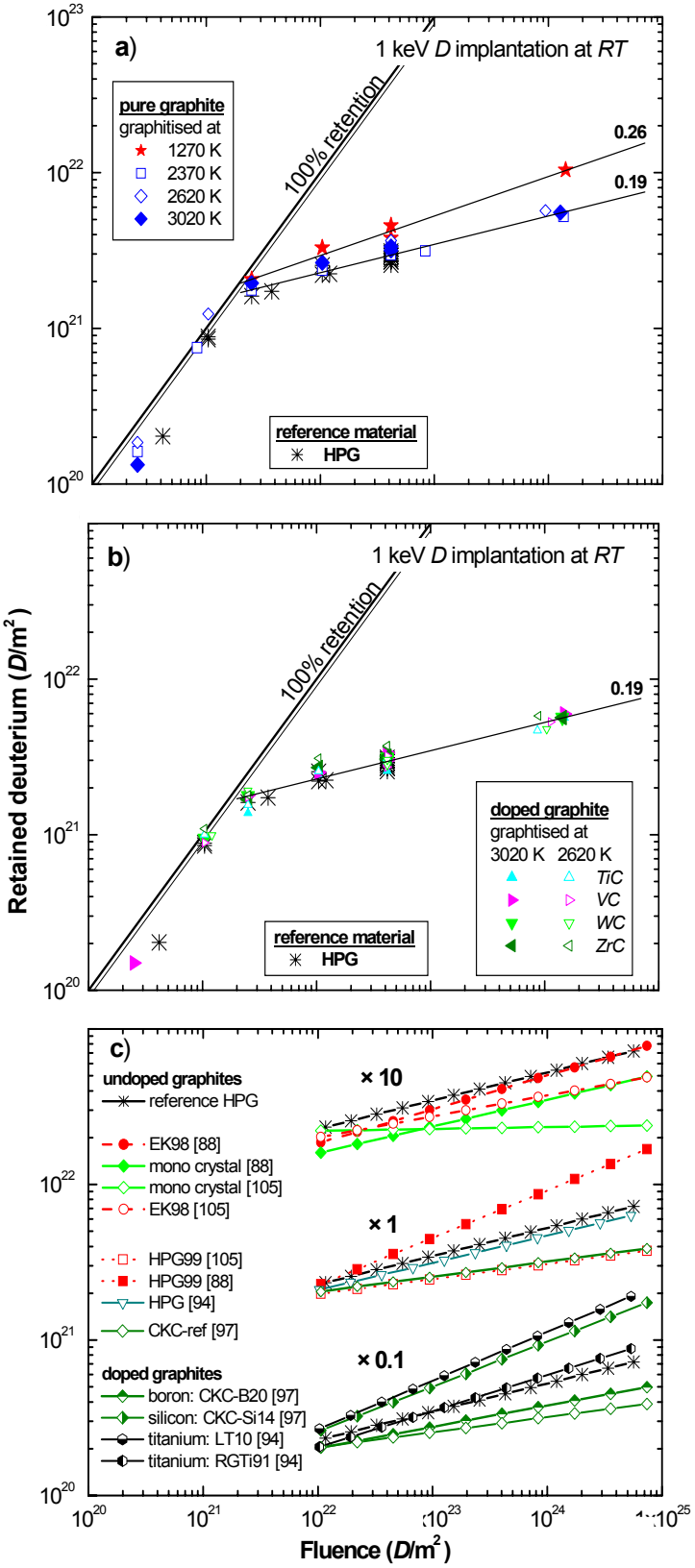

Fig. 4.26. Deuterium retention as a function of implanted fluence: **a**) undoped materials, and **b**) doped materials. The lines correspond to an increase in deuterium retention with fluence of power 0.19 and 0.26 [36]. In **c**) data from literature are shown [88,94,97,105]. In **a**) *Nuclear reaction analysis* (*NRA*) data are included.

The structure of all these graphites is comparable, since all of them have been produced under similar conditions. Therefore, it can be concluded that neither the type of dopants nor the porosity (open or closed) influence the deuterium retention. Additionally, the graphitised materials exhibit practically the same deuterium retention as the pyrolytic graphite taken as a reference material, which has very low porosity and very different microstructure. Pyrolytic graphite was chosen as a reference because in previous studies [94] it was observed to retain less deuterium than any of the graphites analysed here, probably due to its low porosity.

For the present study it can be concluded that the microstructure of the doped graphites from *CEIT* is the most favourable on what deuterium retention is concerned. The higher deuterium retention of the calcinated sample possibly corresponds to a higher porosity, as well as a different morphology of the porosity and a more disordered crystalline structure, with many more defects than in the graphitised samples.

The obtained results have been compared with similar measurements taken by other research groups [88,94,97,105]. **Fig. 4.26 c** illustrates the results of similar measurements on doped and undoped graphites from different producers. Comparison should be accomplished with caution, considering the possible effect of calibration errors of the gauging equipment, and the experimental differences when obtaining the deuterium retention for the materials compared [36]. However, it may be concluded that the carbide-doped fine-grain graphites analysed in this work present similar or even lower deuterium retention than other doped and undoped commercial materials. In any case, adding dopants does not affect the deuterium retention of the materials studied here.

4.3. Answers to the open questions of main interest

- **Answer 1:** according to the results of this work, the optimum material with regard to erosion, thermal conductivity and tritium retention is a *TiC*-doped fine-grain graphite. Tritium retention is similar or even lower than for other doped carbon materials. The highest thermal conductivity was reached by doping with 4 at.% *TiC* (225 W/mK; graphitisation temperature: ~2870 K, dwell time: 2 h), without detriment to other mechanical properties, due to the homogeneous distribution of *TiC* grains. Regarding the erosion, all doped graphites investigated show similar and positive behaviour, whereby the better homogeneity of *TiC*-doping emphasises the choice of this doped graphite.
- **Answer 2:** Two mechanisms are responsible for the mitigation of the chemical erosion by doping. The first one consists of a geometrical shielding effect of the dopants, which enhances the dopant concentration at the surface and protect the underlying carbon atoms from further erosion. The second one is a chemically-induced change of the thermally activated regime, Y_{therm}, by reducing the activation energy of hydrogen release, E_{Hrel}.
- **Answer 3:** The erosion behaviour of the doped graphites developed at *CEIT* is very promising due to their reduced chemical erosion and improved thermo-mechanical properties. Therefore, they can seriously be a better choice than *CFCs* for their use at the divertor plates in *ITER*.

5. Conclusion

The chemical erosion behaviour of the improved carbide-doped fine-grain graphites produced at *CEIT* has been characterised, as well as their deuterium retention by mono-energetic deuterium implantation as a function of the accumulated deuterium fluence.

The influence of doping on the chemical erosion of carbon has been investigated for each chemical erosion regime individually and therefore four statements can be drawn:

- The surface regime of the chemical erosion of carbon, given by Y_{surf}, is not chemically affected by doping. However, preferential erosion of carbon and the resulting enrichment of dopant on the surface leads to a very strong reduction of the net erosion of carbon, which will be the faster reached, the finer and more homogeneously distributed the dopant is. A development of a strong surface topography is always observed, specially for low impacting energies of deuterium. The largest reduction of the total erosion yield, Y_{tot}, observed until now corresponds to a *TiC*-doped graphite with 4 at.% *Ti* after an accumulated fluence of ~10^{25} *D*/m^2. Fluences of this order of magnitude are expected to be accumulated in the *PFM* of *ITER* after ~10 seconds.
- The thermally activated regime of the chemical erosion of carbon, given by Y_{therm} is chemically influenced by doping. A chemically-induced reduction of Y_{CD4} of ~25% at T_{max} has been observed when graphite is doped with 4 at.% metal carbides.
- For nano-dispersed metal-doped carbon films containing *V*, *Ti* and *W*, a strong reduction of Y_{therm} measured by Y_{CD4} at elevated temperatures compared to pure carbon has been observed. The reduction depends on the metal concentration and the Y_{CD4} diminishes continuously above *RT* for doping with several at.% of metal. This diminution of the yield can be attributed to a reduction of the *activation energy for hydrogen release*, E_{Hrel}, similarly to the already known case of *B*-doped graphites. This lowered activation energy may cause lower desorption temperatures for retained hydrogen in such doped carbon films.

- Y_{CD4} for all nano-dispersed metal-doped carbon films investigated is enhanced at *RT* compared to pure carbon and shows a maximum depending on the metal concentration. But this enhancement does not mean an enhancement of the total erosion yield, Y_{tot}, at *RT*, because it is due to changes of the distribution of the erosion products to an increased production of CD_4. The amount of heavier hydrocarbons and of high sticking erosion species produced have been reduced by the presence of the metal dopant and, therefore, the increased Y_{CD4} at *RT* is just an artefact of the assumption of the calibration, which does not take into account variations in the ratios of radicals to molecules and C_1D_z to heavier hydrocarbons, $C_{x>1}D_y$ due to the doping.

In respect to the hydrogen retention, the calcinated samples of the pure fine-grain graphites produced at *CEIT* reveal significantly higher deuterium retention than the graphitised samples, i.e. crystalline order has a considerable influence on the retention of hydrogen. For the doped graphitised samples, neither the type of dopant nor the nature of porosity (open or closed) affects the deuterium retention. Apart from this, the materials studied manifest similar or even lower deuterium retention than other doped and undoped commercial materials.

6. References

[1] G. Janeschitz, K. Borrass, G. Federici, Y. Igitkhanov and A. Kukushkin, J. Nucl. Mater. **220–222** (1995) 73.

[2] R. Behrisch, G. Federici, A. Kukushkin and D. Reiter, J. Nucl. Mater. **313–316** (2003) 388.

[3] M. Merola, W. Dänner, J. Palmer, G. Vielder, C. H. Wu and EU *ITER* Participating Team, Fusion Eng. Des. **66-68** (2003) 211.

[4] G. Janeschitz, *ITER* JCT and *ITER* HTs, J. Nucl. Mater. **290-293** (2001) 1.

[5] R. Aymar and International Team, J. Nucl. Mater. **307-311** (2002) 1.

[6] Technical Basis for the *ITER* Final design, EDA Documentation Series No. **22**, IAEA, Vienna 2001.

[7] G. Federici, C.H. Skinner, J.N. Brooks, J.P. Coad, C. Grisolia, A.A. Haasz, A. Hassanein, V. Philipps, C.S. Pitcher, J. Roth, W.R. Wampler and D.G. Whyte, Nucl. Fusion **41** (2001) 1967.

[8] A. Loarte, "Implications of the use of carbon-based plasma-facing components in the next-step fusion devices", 10th Int. Workshop on Carbon Materials for Fusion Application, Jülich (Germany), September 17-19th 2003.

[9] G. Federici, J.N. Brooks, D.P. Coster, G. Janeschitz, A. Kukuskhin, A. Loarte, H.D. Pacher, J. Stober and C.H. Wu., J. Nucl. Mater. **290-293** (2001) 260.

[10] A. von Keudell, C. Hopf, T. Schwarz-Selinger and W. Jacob, Nucl. Fusion **39** (1999) 1451.

[11] G. Federici, R. Anderl, J.N. Brooks, R. Causey, J.P. Coad, D. Cowgill, R. Doerner, A.A. Haasz, G. Longhurst, S. Luckhardt, D. Mueller, A. Peacock, M. Pick, C.H. Skinner, W. Wampler, K. Wilson, C. Wong, C. Wu and D. Youchison, Fusion Eng. Des. **39-40** (1998) 445.

[12] G. Federici, P. Andrew, P. Barabaschi, J. Brooks, R. Doerner, A. Geier, A. Herrmann, G. Janeschitz, K. Krieger, A. Kukushkin, A. Loarte, R. Neu, G. Saibene, M. Shimada, G. Strohmayer, M. Sugihara, J. Nucl. Mater. **313-316** (2003) 11.

[13] R. Behrisch, J. Ehrenberg, M. Wielunski, A.P. Martinelli, H. Bergsaker, B. Emmoth, L. de Kock and J. P. Coad, J. Nucl. Mater. **145-147** (1987) 723.

[14] J.P. Coad, M. Rubel and C.H. Wu, J. Nucl. Mater. **241-243** (1997) 408.

[15] G. Federici, R.A. Anderl, P. Andrew, J.N. Brooks, R.A. Causey, J.P. Coad, D. Cowgill, R.P. Doerner, A.A. Haasz, G. Janeschitz, W. Jacob, G.R. Longhurst, R. Nygren, A. Peacock, M.A. Pick, V. Philipps, J. Roth, C.H. Skinner and W.R. Wampler, J. Nucl. Mater. **266-269** (1999) 14.

[16] T. Hino, T. Yamashina, S. Fukuda and Y. Takasugi, J. Nucl. Mater. **186** (1991) 54.

[17] C. García-Rosales, E. Gauthier, J. Roth, R. Schwörer and W. Eckstein, J. Nucl. Mater. **189** (1992) 1.

[18] J.W. Davis and A.A. Haasz, J. Nucl. Mater. **195** (1992) 166.

[19] C. García-Rosales and J. Roth, J. Nucl. Mater. **196-198** (1992) 573.

[20] C. García-Rosales, J. Roth and R. Behrisch, J. Nucl. Mater. **212-215** (1994) 1211.

[21] A.Y.K. Chen, A.A. Haasz and J.W. Davis, J. Nucl. Mater. **227** (1995) 66.

[22] P. Franzen, A.A. Haasz and J.W. Davis, J. Nucl. Mater. **226** (1995) 15.

[23] R. Schwörer, H. Plank and J. Roth, J. Nucl. Mater. **230** (1996) 208.

[24] J. Roth, H. Plank and R. Schwörer, Physica Scripta **T64** (1996) 67.

[25] A. Pospieszczyk, V. Philipps, E. Casarotto, U. Kögler, B. Schweer, B. Unterberg and F. Weschenfelder, J. Nucl. Mater. **241-243** (1997) 833.

[26] J.P. Qian, J. Roth, J.R. Song, F. Zhang, L. Yang and G.T. Zhai, J. Nucl. Mater. **258-263** (1998) 706.

[27] J. Roth, J. Nucl. Mater. **266-269** (1999) 51.

[28] R. Jimbou, K. Nakamura, V. Bandourko, M. Dairaku, Y. Okumura and M. Akiba, J. Nucl. Mater. **266-269** (1999) 1103.

[29] M. Balden, Physica Scripta **T81** (1999) 64.

[30] C. García-Rosales and M. Balden, J. Nucl. Mater. **290-293** (2001) 173.

[31] M. Balden, C. García-Rosales, R. Behrisch, J. Roth, P. Paz and J. Etxeberria, J. Nucl. Mater. **290-293** (2001) 52.

[32] E. Salonen, K. Nordlund, J. Keinonen, N. Runeberg and C.H. Wu, J. Appl. Phys. **92** (2002) 2216.

[33] Q.G. Guo, J.G. Li, N. Noda, Y. Kubota, J.L. Chen, Zh.J. Liu, L. Liu and J.R. Song, J. Nucl. Mater. **313-316** (2003) 144.

[34] H. Yagi, H. Toyoda and H. Sugai, J. Nucl. Mater. **313-316** (2003) 284.

[35] A. Ōya and H. Marsh, J. Mater. Sci. **17** (1982) 309.

[36] E. Oyarzabal Vicente, "Influencia de la adición de pequeñas cantidades de carburos en la retención de deuterio de un grafito isótropo elaborado a partir de microesferas de mesofase carbonosa", 2nd Diploma Thesis, Universidad de Navarra, San Sebastián, June 2002.

[37] K. Durocher, "Deuterium retention in doped graphites", Diploma Thesis, Université Pierre et Marie Curie, Paris, June 2001.

[38] I. Quintana Alonso, "Production and characterisation of metal doped carbon films", Diploma Thesis, Universidad de Navarra, San Sebastián, April 2004.

[39] P. Sigmund, in *Fundamental Processes in Sputtering of Atoms and Molecules*, (P. Sigmund, Ed.), Symp. on occasion of 250th Anniversary of the Royal Danish Academy of Sciences and Letters, Copenhagen (1993).

[40] R. Behrisch (Ed.), *Sputtering by Particle Bombardment I*, Topics in Applied Physics, Vol. **47**, Springer, Berlin (1981).

[41] J. Roth, E. Vietzke and A.A. Haasz, "Atomic and Plasma-Material Interaction Data for Fusion", Suppl. Nucl. Fusion **1** (1991) 63.

[42] C. García-Rosales, J. Nucl. Mater. **211** (1994) 202.

[43] C. Hopf, A. von Keudell and W. Jacob, J. Appl. Phys. **94 (4)** (2003) 2373.

[44] Y. Tu, T. Chang and H. Winters, Phys. Rev. B **23** (1981) 823.

[45] H.F. Winters and J.W. Coburn, Surf. Sci. Rep. **14** (1992) 161.

[46] W. Eckstein, C. García-Rosales, J. Roth and W. Ottenberger, “Sputtering Data”, Techn. Rep. IPP 9/82, Max-Planck-Institut für Plasmaphysik, Garching (1993).

[47] J.P. Biersack, W. Eckstein, Appl. Phys. A **34** (1984) 73.

[48] R. Behrisch (Ed.), *Sputtering by Particle Bombardment II*, Topics in Applied Physics, Vol. **52**, Springer, Berlin (1983).

[49] R. Behrisch (Ed.), *Sputtering by Particle Bombardment III*, Topics in Applied Physics, Vol. **64**, Springer, Berlin (1991).

[50] J. Bohdansky, Nucl. Instr. Meth. B **2** (1984) 587.

[51] C. García-Rosales, W. Eckstein, J. Roth, J. Nucl. Mater. **218** (1994) 8.

[52] W. Eckstein and V. Philipps, “Physical Sputtering and Radiation Enhanced Sublimation”, in *Physical Processes of the Interaction of Fusion Plasmas with Solids* (W.O. Hofer and J. Roth, Eds.), Academic Press, San Diego (1996) 93.

[53] J. Bohdansky, J. Roth and H.L. Bay, J. Appl. Phys. **51 (5)** (1980) 2861 with erratum in J. Appl. Phys. **52** (1981) 1610.

[54] E. Pasch, P. Bogen and Ph. Mertens, J. Nucl. Mater. **166** (1990) 33.

[55] N. Matsunami, Y. Yamamura, Y. Itinaka, N. Itoh, Y. Kazumata, S. Mayagawa, K. Morita, R. Shimizu and H. Tawara, Atomic Data and Nuclear Data Tables **31** (1984).

[56] D.L. Smith, J.N. Brooks, D.E. Post, D. Heifetz, Proc. 9th Symp. on Engineering Problems of Fusion Research, Chicago 1981, Institute of Electrical and Electronics Engineers, New York (1982) 719.

[57] W. Eckstein and R. Preuss, J. Nucl. Mater. **320** (2003) 209.

[58] V. Dose, R. Preuss and J. Roth, J. Nucl. Mater. **288** (2001) 153.

[59] M. Balden and J. Roth, J. Nucl. Mater. **280** (2000) 39.

[60] M. Balooch and D.R. Olander, J. Chem. Phys. **63** (1975) 4772.

[61] S.K. Erents, C.M. Braganza and G.M. McCracken, J. Nucl. Mater. **63** (1976) 399.

[62] J. Roth, J. Bohdansky, W. Poschenrieder and M.K. Sinha, J. Nucl. Mater. **63** (1976) 222.

[63] R. Yamada and K. Sone, J. Nucl. Mater. **116** (1983) 200.

[64] A.A. Haasz and J.W. Davis, Nucl. Instr. Meth. B **83** (1993) 117.

[65] A. Horn, A. Schenk, J. Biener, B. Winter, C. Lutterloh, M. Wittmann and J. Küppers, Chem. Phys. Lett. **231** (1994) 193.

[66] J. Küppers, Surf. Sci. Reports **22** (1995) 249.

[67] J. Roth and C. García-Rosales, Nucl. Fusion **36** (1996) 1647, with corrigendum Nucl. Fusion **37** (1997) 897.

[68] M. Wittmann and J. Küppers, J. Nucl. Mater. **227** (1996) 186.

[69] B.V. Mech, A.A. Haasz and J.W. Davis, J. Appl. Phys. **84 (3)** (1998) 1655.

[70] E. Vietzke, J. Nucl. Mater. **290-293** (2001) 158.

[71] J.H. Liang, M. Mayer, J. Roth and W. Eckstein, Nucl. Instr. Meth. **202** (2003) 195.

[72] E. Vietzke and A.A. Haasz in: “Physical Processes of the Interaction of Fusion Plasmas with Solids”, (Edited by W.O. Hofer and J. Roth), Academic Press, San Diego 1996, p.135.

[73] R. Yamada, K. Nakamura, K. Sone and M. Saidoh, J. Nucl. Mater. **95** (1980) 278.

[74] E. Vietzke, K. Flaskamp, V. Philipps, G. Esser, P. Wienhold and J. Winter, J. Nucl. Mater. **145-147** (1987) 443.

[75] E. Salonen, K. Nordlund, J. Keinonen and C.H. Wu, Europhys. Lett. **52 (5)** (2000) 504.

[76] E. Salonen, K. Nordlund, J. Keinonen and C.H. Wu, Phys. Rev. B **63** (2001) 195415.

[77] C.Hopf, „Chemische Zerstäubung und ionenunterstütztes Wachstum amorpher Kohlenwasserstoffschichten – Experimente mit Teilchenstrahlen“, PhD Thesis, Universität Bayreuth, Bayreuth 2003.

[78] C. Hopf, A. von Keudell and W. Jacob, Nucl. Fusion **42** (2002) L27.

[79] J. Roth and W. Möller, Nucl. Instr. Meth. **B7/8** (1985) 788.

[80] B. Söder, J. Roth and W. Möller, Phys. Rev. **B37** (1988) 815.

[81] V. Philipps, E. Vietzke and H. Trinkaus, J. Nucl. Mater. **179-181** (1991) 25.

[82] P. Franzen, J.W. Davis and A.A. Haasz, J. Appl. Phys. **78 (2)** (1995) 817.

[83] Y. Ueda, K. Nakano, Y. Ohtsuka, M. Isobe, S. Goto and M. Nishikawa, J. Nucl. Mater. **227** (1996) 251.

[84] G. Staudenmaier, J. Roth, R. Behrisch, J. Bohdansky, W. Eckstein, P. Staib, S. Matteson and S.K. Erents, J. Nucl. Mater. **84** (1979) 149.

[85] R.A. Causey, M.I. Baskes and K.L. Wilson, J. Vac. Sci. Technol. A **4** (1986) 1189.

[86] W. Möller, J. Nucl. Mater. **162-164** (1989) 138.

[87] W.R. Wampler, B.L. Doyle, R.A. Causey and K. Wilson, J. Nucl. Mater. **176 & 177** (1990) 983.

[88] J.W. Davis, A.A. Haasz and D.S. Walsh, J. Nucl. Mater. **176 & 177** (1990) 992.

[89] K. Asida and K. Watanabe, J. Nucl. Mater. **183** (1991) 89.

[90] K.L. Wilson, R. Bastasz, R.A. Causey, D.K. Brice, B.L. Doyle, W.R. Wampler, W. Möller, B.M.U. Scherzer and T. Tanabe, “Atomic and Plasma-Material Interaction Data for Fusion”, Suppl. Nucl. Fusion **1** (1991) 31.

[91] A.A. Haasz and J.W. Davis, J. Nucl. Mater. **217** (1994) 206.

[92] A.A. Haasz, P. Franzen, J.W. Davis, S. Chiu and C.D. Pitcher, J. Appl. Phys. **77** (1995) 66.

[93] A.A. Haasz and J.W. Davis, J. Nucl. Mater. **220-222** (1995) 832.

[94] M. Mayer, M. Balden and R. Behrisch, J. Nucl. Mater. **252** (1998) 55.

[95] E. Hoinkis, J. Nucl. Mater. **183** (1991) 9.

[96] V.N. Chernikov, W.R. Wampler, A.P. Zakharov and A.E. Gorodetsky, J. Nucl. Mater. **264** (1999) 180.

[97] A.A. Haasz and J.W. Davis, J. Nucl. Mater. **232** (1996) 219.

[98] Y. Gotoh, J. Nucl. Mater. **248** (1997) 46.

[99] B.M.U. Scherzer, R. Behrisch, W. Eckstein, U. Littmark, J. Roth and M.K. Sinha, J. Nucl. Mater. **63** (1976) 100.

[100] S.A. Cohen and G.M. McCracken, J. Nucl. Mater. **84** (1979) 157.

[101] J. Roth, B.M.U. Scherzer, R.S. Blewer, D.K. Brice, S.T. Picraux and W.R. Wampler, J. Nucl. Mater. **93-94** (1980) 601.

[102] W.R. Wampler and C.W., Magee, J. Nucl. Mater. **103-104** (1981) 509.

[103] K.L. Wilson and W.L. Hsu, J. Nucl. Mater. **145-147** (1987) 121.

[104] W. Eckstein, "Sputtering, Reflection and Range Values for Plasma Edge Codes", Techn. Rep. IPP 9/117, Max-Planck-Institut für Plasmaphysik, Garching (1998).

[105] A.A. Haasz and J.W. Davis, J. Nucl. Mater. **209** (1994) 155.

[106] G. Federici, R. Causey, P. Andrew and C.H. Wu, Fusion Eng. Des. **28** (1995) 136.

[107] W. Jacob, Thin Solid Films **326** (1998) 1.

[108] C. Hopf, A. von Keudell and W. Jacob, Diamond and Related Materials **12** (2003) 85.

[109] T. Schwarz-Selinger, M. Meier, C. Hopf, A. von Keudell and W. Jacob, Vacuum **71** (2003) 361.

[110] A. von Keudell, Thin Solid Films **402** (2002) 1.

[111] J. Roth, in *Physics of Plasma Wall Interaction in Controlled Fusion* (D.E. Post and R.Behrisch, Eds.), NATO ISI SeriesB Physics Vol. **131**, Plenum Press, New York, London (1986), 93.

[112] R. Yamada, J. Nucl. Mater. **145-147** (1987) 359.

[113] J.W. Davis, A.A. Haasz and P.C. Stangeby, J. Nucl. Mater. **155-157** (1988) 234.

[114] P. Franzen, E. Vietzke, A.A. Haasz, J.W. Davis and V. Phillips, J. Nucl. Mater. **196-198** (1992) 967.

[115] P. Franzen, „Hochtemperaturreemission von Wasserstoff aus Graphit", PhD Thesis, Technische Universität München, München 1993; also, Max-Planck-Institut für Plasmaphysik, Garching, Report No. IPP 9/92 (1993).

[116] P. Franzen and E. Vietzke, J. Vac. Sci. Techol. A **12** (1994) 820.

[117] J.W. Davis and A.A. Haasz, J. Nucl. Mater. **220-222** (1995) 832.

[118] P. Paz, C. García-Rosales, J. Echeberria, M. Balden, J. Roth and R. Behrisch, Fus. Engin. Des. **56-57** (2001) 325.

[119] C. García-Rosales, P. Paz, J. Echeberria, M. Balden and R. Behrisch, Physica Scripta **T91** (2001) 130.

[120] N. Ordás, C. García-Rosales, S. Lindig, M. Balden and H. Wang, Physica Scripta **T111** (2004) 190.

[121] V.N. Parmon, Catalysis Today **51** (1999) 451.

[122] C. García-Rosales, N. Ordás, E. Oyarzabal, J. Echeberria, M. Balden, S. Lindig and R. Behrisch, J. Nucl. Mater. **307-311** (2002) 1282.

[123] Q.G. Guo, J.G. Li, G.T. Zhai, L. Liu, J.R. Song, L.F. Zhang, Y.X. He and J.L. Chen, J. Nucl. Mater. **290-293** (2001) 191.

[124] G.J. Zhang, Q.G. Guo, Z.J. Liu, L.H. Yao, L. Liu, J.G. Li and J.L. Chen, J. Nucl. Mater. **301** (2002) 187.

[125] C. García-Rosales and N. Ordás, "Desarrollo y caracterización de materiales grafíticos dopados de buenas propiedades plasma/pared para su exposición al plasma de TJ-II", Techn. Rep. *CEIT* IFINAL/1247/R01, Centro de Estudios e Investigaciones técnicas de Gipuzkoa, San Sebastián (2004).

[126] A. Schenk, B. Winter, C. Lutterloh, J. Biener, U.A. Schubert and J. Küppers, J. Nucl. Mater. **220-222** (1995) 767.

[127] S. Marinković, "Chemistry and Physics of Carbon" (P.A. Thrower, Ed.) Marcel Dekker, New York (1984), Vol. XIX, p.1.

[128] H. Plank, R. Schwörer and J. Roth, Surf. Coat. Technol. **83** (1996) 93.

[129] H. Plank, R. Schwörer and J. Roth, Nucl. Instr. Meth. B **111** (1996) 63.

[130] T. Hino, K. Ishio, Y. Hirohata, T. Yamashina, T. Sogabe, M. Okada and K. Kuroda, J. Nucl. Mater. **211** (1994) 30.

[131] Y. Hirooka, R. Conn, R. Causey, D. Croessmann, R. Doerner, D. Holland, M. Khandagle, T. Matsuda, G. Smolik, T. Sogabe, J. Whitley and K.L. Wilson, J. Nucl. Mater. **176 & 177** (1990) 473.

[132] Y. Hirooka, R.W. Conn, M.J. Khandagle, G. Chevalier, T. Sogabe, T. Matsuda, H. Ogura, H. Toyoda and H. Sugai, Fus. Technol. **19** (1991) 2059.

[133] I. Gil Pardo, “Influencia de la adición de carburos en la grafitización de mesofase carbonosa”, Diploma Thesis, Universidad de Navarra, San Sebastián, June 2001.

[134] E. de Juan Pardo, “Influencia de la presión isostática en el proceso de grafitización de grafitos dopados”, Diploma Thesis, Universidad de Navarra, San Sebastián, June 2001.

[135] E. Oyarzabal Vicente, ”Influencia de la adición de pequeñas cantidades de carburos en las propiedades mecánicas de un grafito isótropo elaborado a partir de microesferas de mesofase carbonosa”, 1st Diploma Thesis, Universidad de Navarra, San Sebastián, September 2001.

[136] C. García-Rosales, N. Ordás, E. Oyarzabal, J. Echeberria, M. Balden, S. Lindig and R. Behrisch, J. Nucl. Mater. **307-311** (2002) 1282-1288.

[137] N. Ordás Mur, E. Oyarzabal, C. García-Rosales, J. Echeberria, M. Balden and S. Lindig, “Mejora de las propiedades termomecánicas de grafito isótropo, elaborado a partir de mesofase carbonosa, mediante la adición de carburos”, Boletín de la Sociedad Española de Cerámica y Vidrio 2004 (in press)

[138] N. Ordás, R. Cemboráin, C. García-Rosales, S. Lindig and M. Balden, “Influence of manufacturing parameters on the thermo-mechanical properties of carbide-doped fine-grain graphites”, Proceedings of Carbon ’03, an International Conference on Carbon, 6-10th July 2003, Oviedo.

[139] W. Delle, K. Doizlik, H. Nickel, *Graphitische Werkstoffe für den Einsatz in Kernreaktoren, Teil 1: Pyrolytisch abgeschiedener Graphit*, Thieming Verlag, München, 1979.

[140] W. Delle, K. Doizlik, H. Nickel, *Graphitische Werkstoffe für den Einsatz in Kernreaktoren, Teil 2: Polycristalliner Graphit und Brennelementematrix*, Thieming Verlag, München, 1983.

[141] P. Delhaès (Ed.), *World of Carbon, Vol. 1: Graphite and Precursors*, Gordon and Breach Science Publishers, Singapore, 2001.

[142] M. Merola and the European *ITER* participant group, “Development of carbon materials and plasma-facing components for ITER”, 10th Int. Workshop on Carbon Materials for Fusion Application, Jülich (Germany), September 17-19th 2003.

[143] M. Rödig, M. Kühnlein, M. Merola and B. Schedler, “Effect of neutrons on carbon-based materials“, 10th Int. Workshop on Carbon Materials for Fusion Application, Jülich (Germany), September 17-19th 2003.

[144] C. Arvieu, J.P Manaud, J.M. Quenisset, J. Alloys Compounds **368** (2004) 116.

[145] I. Dahan, U. Admon, N. Frage, J. Sariel, M.P. Dariel, Thin Solid Films **377-378** (2000) 687.

[146] A. G. Ramirez, T. Itoh, R. Sinclair, J. Appl. Phys. **85** (1999) 1508.

[147] D. Nilsson, F. Svahn, U. Wiklund, S. Hogmark, Wear **254** (2003) 1084.

[148] R.G. Agostino, T. Caruso, G. Chiarello, A. Cupolillo, D. Pacilè, R. Filosa, V. Formoso, E. Colavita, L. Papagno, C. Ducati, E. Barborini, C. Lenardi, G. Bongiorno, P. Piseri, and P. Milani, Phys. Rev. B **68** (2003) 035413.

[149] Y.Y. Chang, D.Y. Wang, W. Wu, Thin Solid Films **420-421** (2002) 241.

[150] G.D. Lian, E.C. Dickey, M. Ueno, M.K. Sunkara, Diamond Relat. Mater. **11** (2002) 1890.

[151] S. Inoue, Y. Wada, K. Koterazawa, Vacuum **59** (2000) 735.

[152] A. G. Ramirez, T. Itoh, R. Sinclair, J. Appl. Phys. **85** (1999) 1508.

[153] V.I. Ivanov-Omskii, A.B. Lodygin, S.G. Yastrebov, Compos. Sci. Technol. **63** (2003) 1193.

[154] G. Benedek, P. Milani, V.G. Ralchenko (Eds.), “Nanostructured Carbon for Advanced Applications”, NATO Science Series II: Mathematics, Physics and Chemistry, vol **24**, Kluwer Academic Press, Dordrecht, 2001.

[155] D. Rohde, P. Pecher, H. Kersten, W. Jacob and R. Hippler, Surf. Coat. Technol. **149** (2002) 206.

[156] J. Luthin, H. Plank, J. Roth and Ch. Linsmeier, Nucl. Instr. Meth. B **182** (2001) 218.

[157] E. Vietzke, K. Flaskamp and V. Philipps, J. Nucl. Mater. **111-112** (1982) 763.

[158] R. Yamada and K. Sone, J. Nucl. Mater. **120** (1984) 119.

[159] C. Hopf, A. von Keudell and W. Jacob, J. Appl. Phys. **93 (6)** (2003) 3352.

[160] W. Jacob, C. Hopf, A. von Keudell, M. Meier and T. Schwarz-Selinger, Rev. Sci. Instrum. **74 (12)** (2003) 5123.

[161] H.C. Hill, "Introduction to Mass Spectrometry", 2nd ed. revised by A.G. Loudon, Heyden & Son Ltd. (1966), p.1.

[162] "Quadrupole mass spectrometer: partial pressure measurement in vacuum technology", documentation of Balzers Instruments.

[163] V. Grill, G. Walde, P. Schneider, M. Kurdel, T.D. Märk, Int. J. Mass Spectrom. Ion Processes **129** (1993) 31.

[164] T. Shirai, T. Tabata, H. Tawara, Y. Itikawa, Atomic Data and Nuclear Data Tables, **80** (2002) 147.

[165] A.A. Haasz, O. Auciello, P.C. Stangeby, J. Vac. Sci. Technol. A **4** (1986) 1179.

[166] S. Chiu, A.A. Haasz, J. Nucl. Mater. **196-198** (1992) 972.

[167] V. Philipps, E. Vietzke, M. Erdweg and K. Flaskamp, J. Nucl. Mater. **145-147** (1987) 292.

[168] B.V. Mech, A.A. Haasz, and J.W. Davis, J. Nucl. Mater. **255** (1998) 153.

[169] A.A. Haasz, J.A. Stephens, E. Vietzke, W. Eckstein, J.W. Davis and Y. Hirooka, "Atomic and Plasma-Material Interaction Data for Fusion", Nuclear Fusion Supplement vol. **7** (1998).

[170] J.N. Brooks, Nucl. Technol. Fus. **4** (1983) 33.

[171] D.P. Coster, R. Schneider, J. Neuhauser, H.-S. Bosch, R. Wunderlich, C. Fuchs, F. Mast , A. Kallenbach, R. Dux, G. Becker, ASDEX Upgrade Team, B.J. Braams and D. Reiter, J. Nucl. Mater. **241–243** (1997) 690.

[172] H. Paulin, Ph.D. Thesis, University of Augsburg, Germany, 2000.

[173] U. Fantz and H. Paulin, Physica Scripta **T91** (2001), 25.

[174] S.K. Erents, C.M. Braganza, G.M. McCracken, J. Nucl. Mater. **63** (1976) 399.

[175] R. Yamada, K. Nakamura, K. Sone, M. Saidoh, J. Nucl. Mater. **95** (1980) 278.

[176] E. Vietzke, K. Flaskamp, V. Philipps, J. Nucl. Mater. **128&129** (1984) 545.

[177] T. Schwarz-Selinger, V. Dose, W. Jacob, A. von Keudell, J. Vac. Sci. Technol. A **19** (2001) 101.

[178] J. Roth and H. Pacher, “Chemical Erosion of Carbon Based Materials – a Status Report”, in “Tritium Experience in Large Tokamaks; Application to ITER. Proceedings of the IEA Workshop”, Princenton, NJ, United States, 1998.

[179] K.U. Klages, A. Wiltner, J. Luthin, and Ch. Linsmeier, J. Nucl. Mater. **313-316** (2003) 56.

Appendix A

Introduction into fusion

A.1. Introduction

The main worldwide consumption of energy is currently made of fossil fuels such as oil, coal and gas. During the last decades, their exploitation is strongly rising because of the process of industrialisation and the increasing world population. The burning of these fuels carries out grave climate changes due to massive CO_2 emission into the atmosphere and, furthermore, their resources are restricted and finally becoming insufficient and more expensive [A-1,A-2]. For these reasons, substitutes for fossil fuels should urgently be developed. Nuclear fusion is being investigated in this framework as an alternative energy concept. Even although its performance presents difficulties from the engineer point of view, fusion has substantial advantages compared to other current energy supplies, such as its nearly inexhaustible fuel supply and to be environmentally friendly, so that it has a significant potential in this respect.

A.2. Nuclear Fusion

Nuclear fusion is the nuclear reaction between nuclei of light elements that fuse together to form a heavier element releasing large amounts of energy. This process takes place continuously in the core of the sun where, at temperatures of 10-15 million degrees Celsius, hydrogen (*H*) is converted to helium (*He*) providing enough energy to sustain life on Earth.

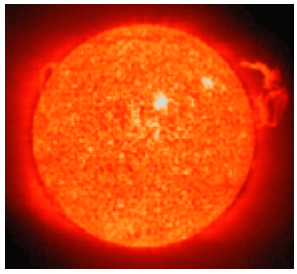

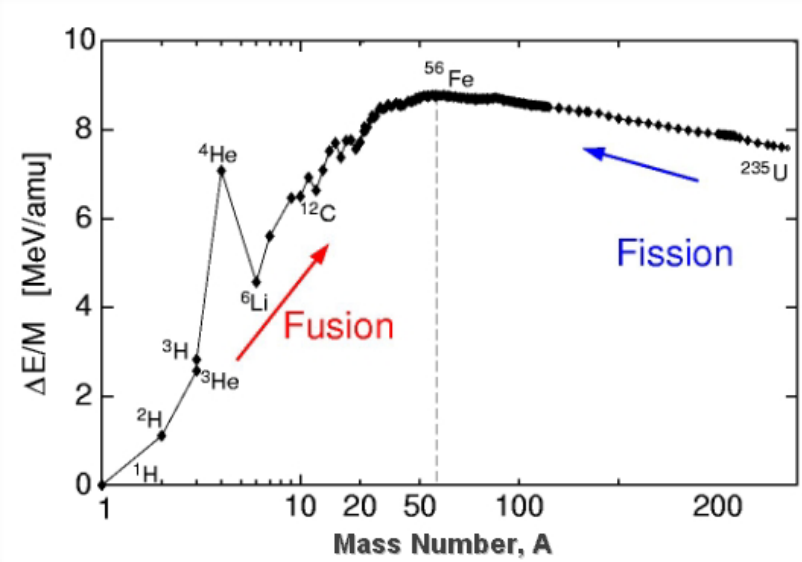

Fig. A.1. Binding energy per nuclear particle (nucleon) in MeV as a function of the Mass Number, *A* [A-3]

Fig. A.1 shows the binding energy per nucleon as a function of the Mass Number, *A*. It has a maximum around 9 MeV for nuclei closed to the iron (*Fe*), which is the most stable nucleus. For light elements, the larger *A* is, the stronger is the binding energy per nucleon (**Fig. A.1**), i.e. the nucleons are lighter and the nucleus more stable. Therefore, in a fusion reaction between light nuclei, the total mass of the resultant nuclei is slightly less than the total mass of the original particles; this mass difference is converted into kinetic energy of the resultant fusion products, as described by Einstein's famous equation:

$$E = mc^2 \tag{A.1}$$

where *E* is the released energy, which is equal to the mass difference, *m*, multiplied by the squared velocity of the light, *c*.

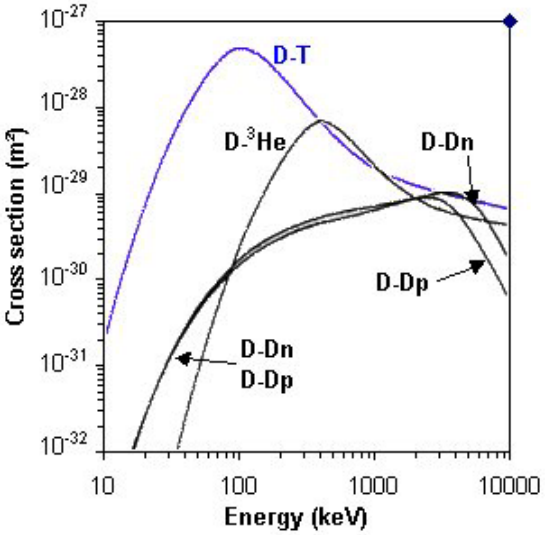

Fig. A.2. Cross-sections of different fusion reactions as a function of the required energy [A-4].

There are several fusion reactions involving light isotopes, but the reaction between the nuclei of the two heavy isotopes of *H* -deuterium (*D*) and tritium (*T*)- is the most suitable one (**Fig. A.2**); this reaction proceeds as following:

$$D + T \rightarrow {}^4He\ (3.517\ \text{MeV}) + n\ (14.069\ \text{MeV}) \tag{A.2}$$

where the energies given are the kinetic energies of the reaction products: ^4He and a neutron (*n*). *D* is a plentiful resource: it is naturally found in sea water with a density of 30 g/m^3. *T* is a weak radioactive element, and it transforms spontaneously into non-radioactive *He*, emitting an electron (e^-) and causing energy to be released in the form of beta radiation (β) with a half-life of 12.43 years. This low-energy β cannot penetrate human skin, so that only consuming large amounts of *T* could be dangerous. In a fusion reactor, *T* can be produced from the reaction of lithium (*Li*), which will cover the central part of the reactor, with the neutrons released from the fusion reactions:

$$^{6}Li + n \rightarrow {}^{4}He + T + 4.86\ \text{MeV} \quad \text{(A.3)}$$

$$^{7}Li + n \rightarrow {}^{4}He + T + n - 2.5\ \text{MeV} \quad \text{(A.4)}$$

There are large reserves of *Li* in the Earth's crust. Eventually, reactions involving just *D-D* or *D-He* (^{3}He) may be also used, but they are not as favourable as the *D-T* reaction, which has by far the largest cross section for relatively low temperatures [A-5].

The development of nuclear fusion as an energy source is one of the most complex scientific and technical tasks ever undertaken for non-military purposes and it will still span several human generations. In order to induce the fusion of nuclei of *D* and *T* it is necessary to surmount the Coulomb repelling force so that the attractive nuclear forces come into play. To achieve this, the particles must retain their energy and remain in the reacting region for a sufficient time. At these required temperatures (around 10 keV, that is about 100 Mills. ºC[1]) the fuel is completely ionised; the resulting gas is an electrically neutral mixture of nuclear ions (positive) and electrons (negative) with very high thermal kinetic energies, called plasma. There are currently known three methods to confine the plasma in order to generate nuclear fusion: *gravitational, inertial and magnetic confinement*. But only the two last methods are possible for producing nuclear fusion on Earth.

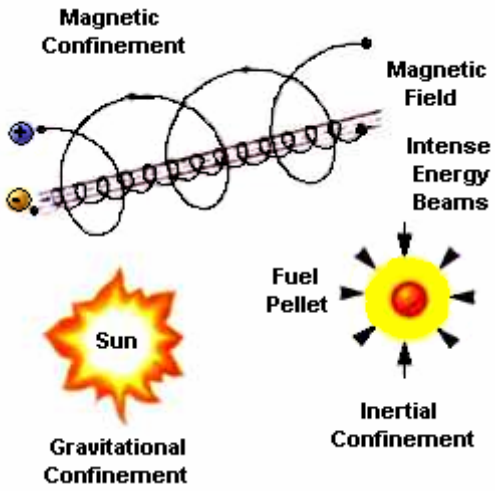

Fig. A.3. Plasma confinement methods.

Inertial fusion consists of micro-explosions of small fuel pellets by means of powerful lasers or particle beams. Confinement of the fuel is based on the inertia of the pellet fuel mass, which resists the natural expansion when it is heated to thermonuclear fusion temperatures. Additional information about inertial fusion can be found in [A-6].

Magnetic fusion heats and confines hot plasma within closed nested magnetic surfaces in a toroidal vacuum vessel. The European fusion effort is concentrated on the latter and only this method will be briefly reviewed here.

[1] The temperature is lower than that corresponding to the energy of maximum cross-section (**Fig. A.2**) because the required reactions occur in the high-energy tail of the Maxwellian distribution of heated particles.

A.2.1. Magnetic Plasma Confinement

In a fusion reactor, the magnetic plasma confinement can basically be performed with two different approaches: **tokamak** and **stellarator** (**Fig. A.4**).

Tokamak means in Russian “toroidal chamber” (toroidalnaya kamera magnitnoi katushki); the Russians L. Artsimovich and A. Sakharov invented it in 1952. The realisation of the closed nested magnetic surfaces for plasma confinement is obtained by superposition of a strong toroidal field of the order of several Tesla with a poloidal field from an internal toroidal current flowing in the plasma (**Fig. A.4 a**) [A-5]. The toroidal field is produced by a set of external discrete coils equally spaced around the vacuum vessel; this field keeps the plasma away from the walls but, however, it is not enough to confine the plasma by itself. For that reason, a second poloidal field is necessary to cancel out the natural pressure inside the plasma, which tries to make it expand. Transformer coupling of the currents in toroidal ring coils induces the toroidal plasma current, which produces the necessary poloidal magnetic field component and, in addition, heats the plasma by ohmic heating. As a result of the superposition of both magnetic field components, nested magnetic surfaces are formed, which effectively confine the charged particles of the plasma. Further toroidal coils are installed for plasma positioning, shape control and for diverting the magnetic field lines at the plasma boundary away from the plasma core, in order to enable magnetic plasma limitation and to solve the particle and energy exhaust problem; this device is called *divertor*.

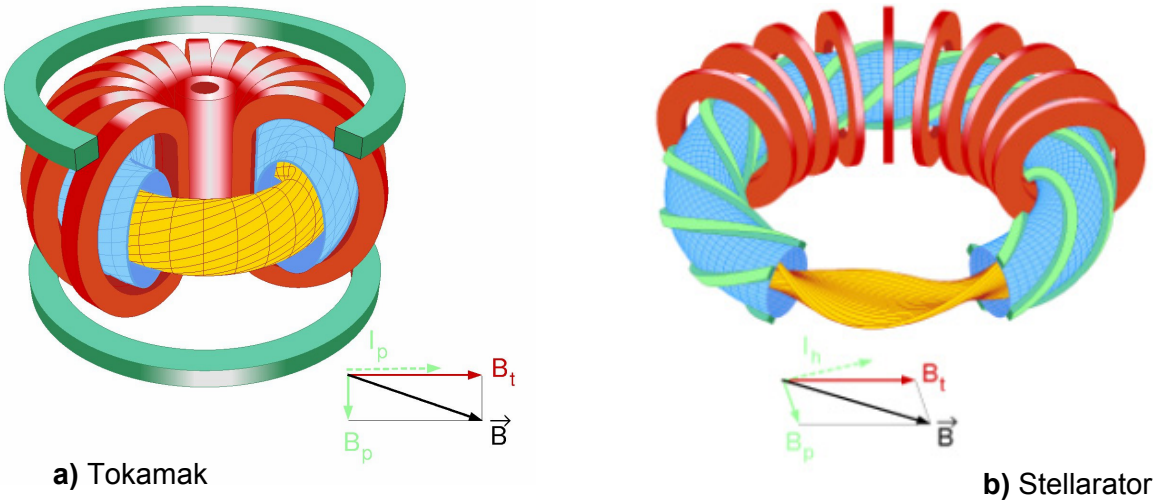

a) Tokamak **b)** Stellarator

Fig. A.4. Schematics of the magnetic plasma confinement approaches tokamak (**a**) and stellarator (**b**).

In the **stellarator configuration** (**Fig. A.4 b**), closed nested magnetic surfaces are entirely created by specially shaped external superconducting coils. The stellarator thus explicitly allows stationary plasma confinement. There is no net current flowing within the plasma. This implies, however, that magnetic surfaces can be established only if the plasma has a toroidally periodic (i.e. not axially symmetric) form. The stellarator concept became even more attractive after the development of optimised confinement configurations and of the modular coil arrangement, and particularly after the discovery of quasi-dynamic and quasi-helically symmetric configurations, which main attain very favourable intrinsic confinement properties.

In view of the fact that the tokamak concept has been brought to a high level of development in all the major fusion programmes of the world, the following information will be focused on it.

To obtain in a tokamak a net positive energy output, i.e. to reach the so-called *ignition* condition, *D-T* plasma has to be heated to temperatures up to very high temperatures (at least 12 keV, ~140 mills. ºC) and a good confinement is necessary. Several criteria have been developed in order to quantify the required confinement in a tokamak. Generally such criteria arise from the balance of the energy given up by the *He* in heating the plasma against the many mechanisms of energy loss (conduction, diffusion and radiation). Normally, the *plasma density (n)*, the *plasma temperature (T)* and the *energy confinement time (τ_E)* are used to quantify the result and the balance equation results in the following triple product, or criteria for *ignition*:

$$n \cdot T \cdot \tau_E \cong 6 \times 10^{21} \text{ m}^{-3} \text{ keV s} \qquad \text{(A.5)}$$

n must be sufficiently large for fusion reactions to take place at the required rate ($>10^{20}$ m^{-3}). The fusion power generated will be reduced if impurity atoms released from the fusion reaction dilute the fuel; consequently, *He* ash must be removed. τ_E measures the efficiency of the magnetic insulation; it is the characteristic time-scale for plasma cooling when the source of heat is removed, and it has to be in the order of seconds. T must be high enough to prevail the repulsive Coulomb's force and to produce an adequate amount of fusion reactions.

In **Fig. A.5** the fantastic progress obtained in magnetic fusion in the last 30 years is shown. Three generations of tokamaks with doubling of characteristic dimensions at each step led to a 10000 times higher value of the fusion triple product.

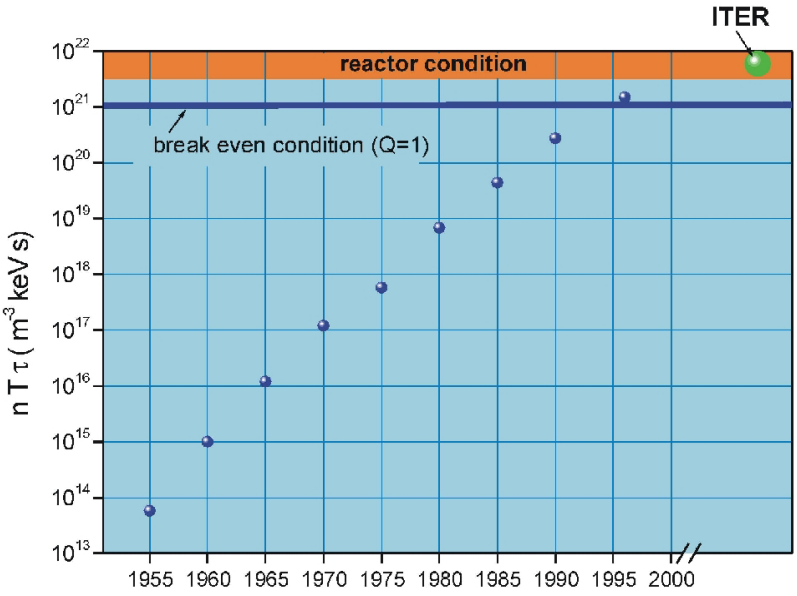

Fig. A.5. Progress on fusion.

Alternative, non-tokamak magnetic fusion approaches (stellarators, reversed field pinches) may offer economic and operational benefits. However, these approaches are more than one generation behind the tokamak line.

A.2.2. ITER

The International Thermonuclear Experimental Reactor (*ITER*) is the next major step for the development of fusion (see **Fig. A.5**). Scientists and engineers from Europe, Canada, Japan, Russia, Korea, China and USA are working in an unprecedented international collaboration on this reactor, which is the second world's largest international co-operative research and development project after the International Space Station (*ISS*).

With the impending construction and operation of *ITER*, fusion research is at the dawn of a new era. *ITER* will be the first machine based on the tokamak configuration to provide plasma dominated by α-particle heating, combining the plasma physics with the key reactor technologies of high heat flux components and long-term superconducting magnet technology necessary for power production.

One of the main *ITER* goals is to demonstrate the safety and environmental potential of fusion power for its essential characteristics: low fuel inventory, ease of burn termination, low power and energy densities, large heat transfer surfaces and the fact that confinement barriers exist and must anyway be leak-tight for successful operation.

A cutaway of the *ITER* Tokamak is shown in **Fig. A.6**. The magnet system consists of 18 Nb_3Sn toroidal field (*TF*) coils, a central solenoid (*CS*) of six modules, which can be powered separately, six *NbTi* poloidal field (*PF*) coils, and 18 *NbTi* saddle-shaped coils. *ITER* will be the first device to use *Nb_3Sn* superconductors on a large scale. It adopts a new design of superconducting cables in a conduit of steel [A-7].

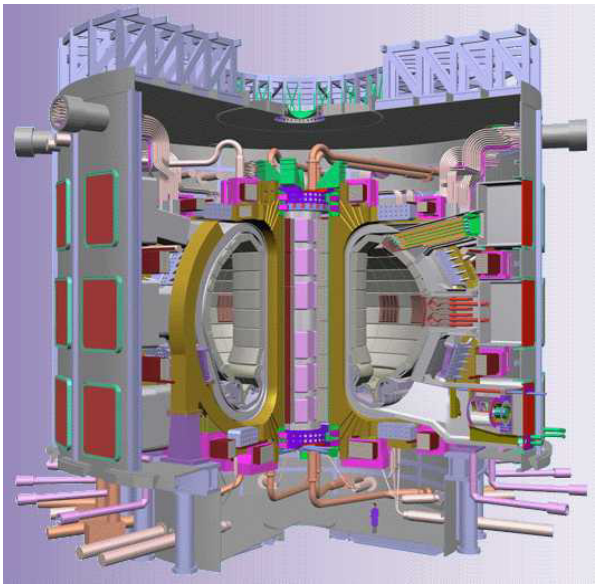

Fig. A.6. Cutaway of *ITER* tokamak.

The major parameters and dimensions of *ITER* are shown in **Table A.1**:

Total Fusion Power (MW)	500 (700)
Plasma major radius (R,m)	6,2
Plasma minor radius (a,m)	2,0
Plasma current (I_p,MA)	15
Plasma volume (m^3)	837
Plasma surface (m^2)	678
Current drive power (MW)	73

Table A.1. Main parameters and dimensions of *ITER*.

ITER's goal is to demonstrate the scientific and technical feasibility of fusion energy for peaceful purposes, which means to demonstrate moderate power amplification and extended burn of *D-T* plasmas, with steady-state as an ultimate goal and to perform testing of high heat flux and nuclear components [A-8].

A.2.3. Plasma-wall interactions

Although the magnetic confinement avoids the direct contact between the hot *H* plasma and the plasma-facing materials (*PFMs*), plasma diffusion and drift across the magnetic surfaces are unavoidable. Besides, the interaction of the plasma with the surrounding wall is a necessary condition because the wall should absorb all the power produced by the α-particles and introduced by external heating [A-9,A-10] and it has also to enable exhaust of the produced ^4He ash [9,10]. Plasma-wall interactions lead to a variety of different processes in the near surface region of the walls, some of which modify the properties of the boundary and main plasma in a feedback-like behaviour. An important example is the plasma-induced release of impurities.

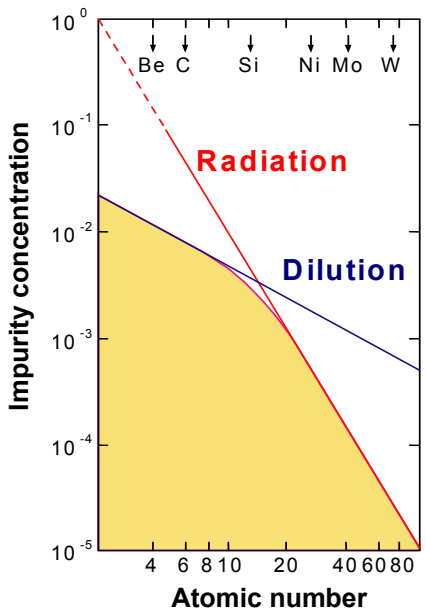

Fig. A.7. Maximum tolerable concentration of impurities.

Impurities present a number of problems in tokamak plasmas. One is the *irradiative power loss*, principally due to line radiation from partially stripped ions. Another is *fuel dilution*. This arises because impurity atoms produce many electron and, for a given plasma pressure, these electrons take the place of fuel particles. At high concentrations, impurities prevent the plasma being heated. This is particularly a problem during the plasma start-up phase, since impurities radiate most strongly at low temperatures before they become highly ionised. Impurities can also lead to disruptions as a result of edge cooling and consequent current profile modification. Depending on the *atomic number* (*Z*) of the impurity, there is an impurity concentration limit in the hot plasma (**Fig. A.7**) that should not be reached to ensure plasma stability [A-11].

From the plasma, a flow of ions and neutral atoms reaches the surfaces surrounding the plasma. The incident particles lead to *erosion processes* on the material's surfaces. Radiation from the plasma as well as the incident particles causes *energy deposition* on the surface of the plasma-facing component. The resulting *thermo-mechanical loading* of materials and components limit the lifetime of the component. Excessive heat loads during operation lead to destruction by melting or fracture. Furthermore, the materials can also adsorb hydrogen isotopes and eventually release fractions of the sorted gas under thermal loading. This influences the particle balance during plasma operation of the device. In

addition to these fluctuations, the more residence *inventory of hydrogen isotopes* in a fusion device depends strongly on the selection of materials and should be minimised. The intense *neutron irradiation* also damages to materials, which results in degradation of dimensional stability, physical and mechanical properties. So *PFMs* have to be developed and optimised in order to meet these requirements.

Plasma-facing components will be in *ITER* necessarily experimental due to the need to explore a wide variety of physics regimes to find the optimum performance and to identify any promising development paths for future devices. It is therefore essential that they are replaceable as simply as possible. For this purpose *ITER* uses a modular approach to in-vessel components, with the use of blanket modulus and divertor cassettes that can be removed through the ports in order to minimize waste, thereby minimising cost and environmental impact. This procedure has been demonstrated for both blanket and divertor at full scale [A-12].

The choice of *PFMs* for high heat flux components is a compromise between material durability, tolerance to peak loading, trapping of *tritium* and plasma poisoning. Different materials have been chosen for different locations, depending on the relative importance of these effects (**Fig. A.8**): beryllium (*Be*) for the first wall, *C* for the divertor target plates, and tungsten (*W*) for the divertor throat. A number of technologies for joining *PFMs* to cooling channels and to structural support have been developed, and prototypes of all components have been tested in high heat flux facilities to model the operational loads.

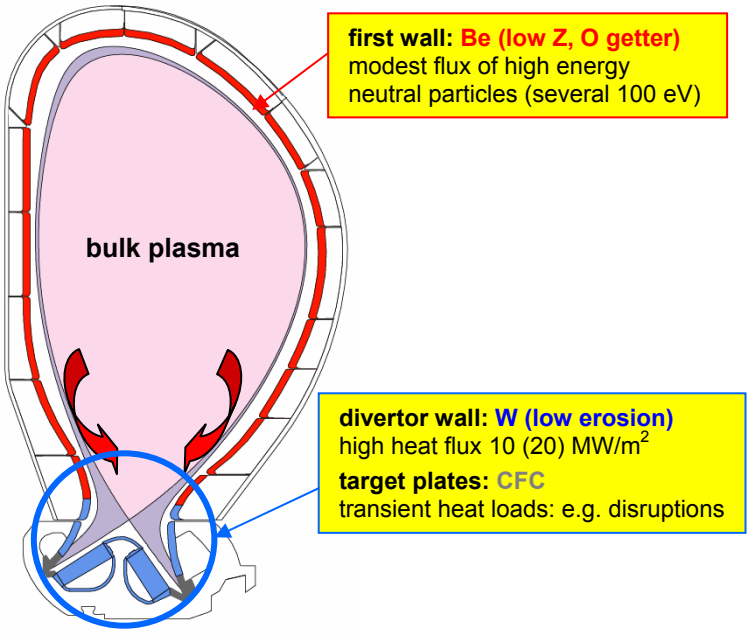

Fig. A.8. Poloidal cross-section of an *ITER* plasma, showing the current selection of *PFMs* for the first wall and the divertor plates.

Tritium co-deposition with eroded *C* is expected to be the dominant *T* retention mechanism in *ITER* even if the use of *C* is limited to the divertor strike plates. On-going experiments in specific facilities [A-13] have already shown that the low values of codeposition are obtained by maintaining the wall temperature above 100 °C. If necessary, some remedial action (*T* removal techniques, or replacing *C* with *W*) can be implemented to offset underestimated or unforeseen phenomena.

A.3. References

[A-1] J. Ongena, G. Van Oost, “Energy for Future Centuries. Will fusion be an exhaustible, safe and clean energy source?”, Transactions of Fusion Science and Technology, vol. **41** (2002).

[A-2] U. Schumacher, “Status and Problems of Fusion Reactor Development”, Naturwissenschaften **88** (2001) 102.

[A-3] U. Schumacher, *Fusions-Forschung. –Eine Einführung-*, Wissenschaftliche Buchgesellschaft, Darmstadt (1993) p. 3.

[A-4] F. Engelmann, in *Physics of Plasma Wall Interaction in Controlled Fusion* (D.E. Post and R.Behrisch, Eds.), NATO ISI Series B Physics Vol. **131**, Plenum Press, New York, London (1986).

[A-5] J. Wesson, *Tokamaks*, Oxford Engineering Science Series 48, 2nd Edition, Clarendon Press–Oxford (1997).

[A-6] W.J. Hogan (Ed.), *Energy from Inertial Fusion*, International Atomic Energy Agency, Vienna, Austria (1995).

[A-7] Technical Basis for the *ITER* Final design, EDA Documentation Series No.**22**, IAEA, Vienna (2001).

[A-8] R. Aymar, Y. Shimomura, M. Huguet, V. Chuyanov and ITER teams, “*ITER*: Fusion Research at the Dawn of a New Era“, International Atomic Energy Agency, 19th IAEA Fusion Energy Conference, Lyon, France, Oct. 2002.

[A-9] D. Reiter, G.H. Wolf and H. Klever, Nucl. Fusion **30** (1990) 2141.

[A-10] R. Behrisch and V. Prozesky, Nucl. Fusion **30** (1990) 2166.

[A-11] W. Möller and B.M.U. Scherzer, J. Appl. Phys. **64** (1988) 4860.

[A-12] D. Maisonnier, G. Cerdan, S. Chiocchio, C. Damiani, J.-P. Friconneau, R. Haange, M. Irving, E. Martin, J. Palmer, A. Poggianti, M. Siuko, E. Tada, N. Takeda, A. Tesini, R. Tivey and A. Turner, “ITER-FEAT Divertor Remote Maintenance”, 18th IAEA Fusion Energy Conference, Sorrento, Oct. 2002, paper ITER/P24.

[A-13] V. Philipps, J. P. Coad, G. Matthews, P. Wienhold, A. Kirschner, J. Brooks, G.F. Federici and R. Laesser, “Recent results on long-term fuel retention in *JET* and Textor and predictions for *ITER*”, International Atomic Energy Agency, 19th IAEA Fusion Energy Conference, Lyon, France, Oct. 2002.

Appendix B

Graphites: structure and properties

Catalytic graphitisation by doping

B.1. Structure and Properties of Graphites

Carbon is known to occur with three different crystalline varieties: *diamond*, *rhombohedral graphite* and *hexagonal graphite*, whereas the two first are thermodynamically metastable. The crystal structure of *diamond* is cubic face centred, where four carbon atoms at the corner of a regular tetrahedron forming strong covalent sp^3 bonds to every surrounding carbon atom. In contrast, the basic form of carbon in *graphite* is constituted with sp^2 type aromatic bonds that form condensed hexagonal cycles. The stacking of these planar atomic sheets, called graphenes, forms bulk forms of *graphite* [B-1-B-3].

A single crystal of *graphite* has a hexagonal lattice structure, where the graphene layers are stacked either in translational …ABAB… sequence (*hexagonal graphite*) or with a periodicity …ABCABC… (*rhombohedral graphite*). *Hexagonal graphite* has an in-plane nearest neighbour distance of 1.421 Å and perpendicular interplanar distance of 3.354 Å at room temperature (*RT*), as shown in **Fig. B.1 a**:

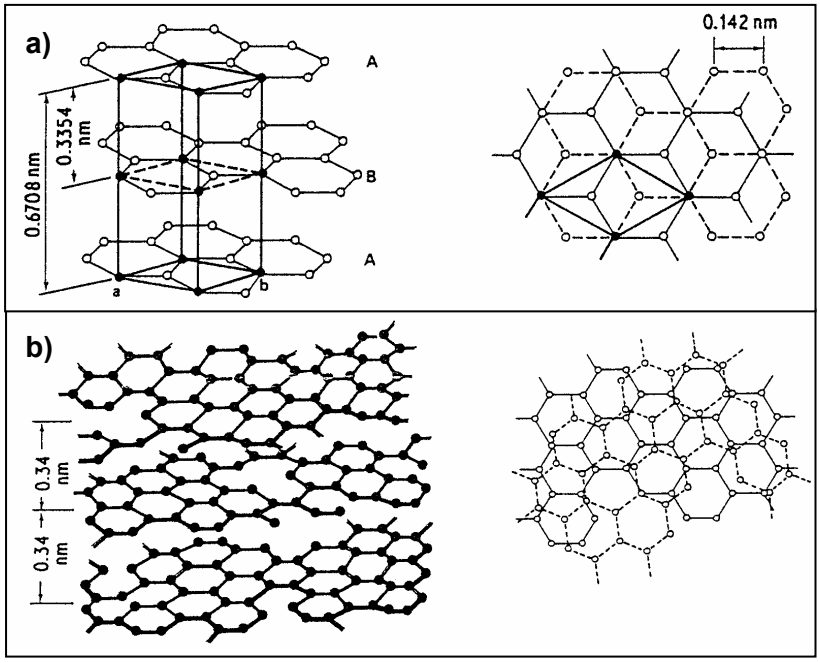

Fig. B.1. Diagrams of structures of (**a**) ideal hexagonal graphitic structure and (**b**) turbostratic structure of carbon [B-4].

Within the graphene layers, the carbon atoms are linked by extremely strong covalent bonds (binding energy of 4.8 eV), for which three of the four valence electrons are involved as localised σ-electrons. The fourth non-localised electron, or π-electron, leads to

bind the layers among themselves by a quasi-metallic bound. Besides, due to the adjustment of the neighbouring layers against each other, Van der Waals forces are also superposed and hold the layers together (binding energy between layers from 0.1 to 0.2 eV). The π-electrons are responsible for the high electrical and thermal conductivity of graphite parallel to the basal plane. However, graphite is an excellent insulator in the direction perpendicular to the basal plane. The anisotropy of the graphite binding energies is also manifested in further physical properties: i.e., the Young's modulus parallel to the basal plane is approximately 1000 GPa, one of the highest theoretical values of all materials; but perpendicular to the layers, the Young's modulus is much lower [B-5].

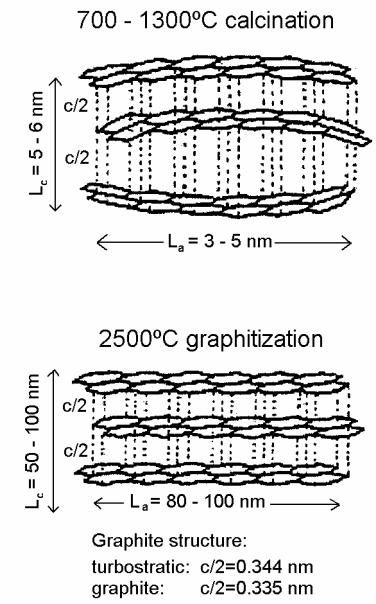

Fig. B.2. Graphitic structure after calcination and after graphitisation [B-2].

The route of carbon production is thermal decomposition of pyrolysis of carbonaceous compounds. After calcination at temperatures until 700-1000ºC and before graphitisation, the carbon is unordered and it still contains impurities, like Oxygen (*O*) or Hydrogen (*H*). Carbon has a quasi-2D structure (*turbostratic structure*, see **Fig. B.1 b**, in which the unordered approximately parallel carbon layer planes are weakly bound by Van der Waals forces. During graphitisation at temperatures above 1500ºC the unordered stacked layers becomes more and more crystalline towards the perfect hexagonal graphite structure, and the spacing between the *(002)* planes decreases. This reduction in crystallite spacing is accompanied by an enormous increase in the crystallite size parallel (L_a) and perpendicular (L_c) to the graphite basal plane (**Fig. B.2**). The crystallite height L_c is generally used for the determination of the crystallinity of graphitised samples (*degree of graphitisation)* [B-1], which can be determined from X-ray diffraction measurements by measuring the breath of the basal plane reflection, given by the Scherrer formula [B-6]:

$$L_c = \frac{0.9\,\lambda}{B\cos\theta} \qquad \text{(B.1)}$$

where λ is the wavelength of the radiation used (for *Cu K*α line, λ=1.54184 Å), *B* is the angular position of the full width at maximum of the *(002)* reflex and θ is the angular position of the *(002)* reflex.

B.2. Catalytic graphitisation by doping with metallic carbides

Obtaining graphitic materials requires high temperatures in order to reach the adequate atomic arrangement that will cause the stable graphitic layers to form (graphenes). These high temperatures may reach 2500-3000 ºC. Incorporating certain metallic elements is known to facilitate the formation of graphite, lowering the temperature necessary to transform a carbonaceous material with a low degree of order into a graphite with a high degree of crystallinity [B-7]. These metals have a catalysing effect on graphitisation. During the past years, huge efforts have been made to understand the mechanisms that play a part in catalytic graphitisation, specially in the production of s*ingle wall carbon nanotubes*, *SWNT*s. Several models that take into consideration phase transformations have been developed searching for an explanation on the transformation of amorphous carbon into graphite, in the presence of metals. Among them, the S-L-S model (Solid-Liquid-Solid) is based upon processes of dissolution-precipitation of carbon, catalysed through molten nanometric metallic particles, carbon supersaturated (*M-C* particles).

Assuming a number of observations this model can be applied to the graphitisation process of the graphites investigated in this thesis:

- Overwhelming increase in the size of the graphitic crystals (L_c) above a certain temperature, which is different for each dopant, and close to the eutectic temperature of the *C*-metal system of the carbide.
- Variation of the porosity at practically the same temperature as for the changes in L_c.
- Broadening of the particle size distribution of the carbides after graphitisation. This manifests in two facts: high mobility of the carbides during graphitisation, provoking local heterogeneities; and presence of nano-metric carbides after graphitisation, which are much smaller than the initial carbides.

The steady state of the catalysing substance may be significantly different from its conventional equilibrium state. As in this case, it can be found in a metastable steady state supersaturated and molten, which does not agree with what the stable phase diagram dictates. A clear example of the formation of metastable phases during catalytic processes would be the emergence of liquid phase in the metallic particles responsible for

catalysing graphitisation of amorphous graphite, at temperatures noticeably lower than the eutectic of the *C*-metal system, as will be next explained [B-8].

B.2.1. Catalytic graphitisation according to the S-L-S model

Catalytic graphitisation according to the S-L-S model takes place in carbonaceous materials which contain metals belonging to groups VI and/or VIII, and implies the dissolution of the amorphous carbonaceous phases inside the metal (partially or totally liquid), and their subsequent precipitation in the form of graphite when the system is cooled, or as a result of super saturation of metallic particles. In other words, it is a liquid phase graphitisation in which the metal acts as a means of transport. According to this model [B-9,B-10], studied on amorphous doped carbon layers, the catalytic graphitisation mechanism takes place in three stages:

B.2.1.1. Liquefaction of the M-C particles

The first step in the catalysis process is the formation of liquid nano-particles supersaturated with carbon. When the temperature is high enough, the metallic particle absorbs carbon from the matrix in contact with its surface. As the absorption process evolves, the smallest particles (and the outer region of the biggest) turn into liquid. The small size particles melt at extraordinary low temperatures, between 500 and 900 ºC below the eutectic, because a metastable solution supersaturated with carbon forms in the catalysing metal, and may contain up to 50 wt. % of carbon.

The following reaction must be considered first:

$$C_{amorphous} \xrightarrow[metastable]{} C_{graphitic} \tag{B.2}$$

and takes place as shown in **Fig. B.3**:

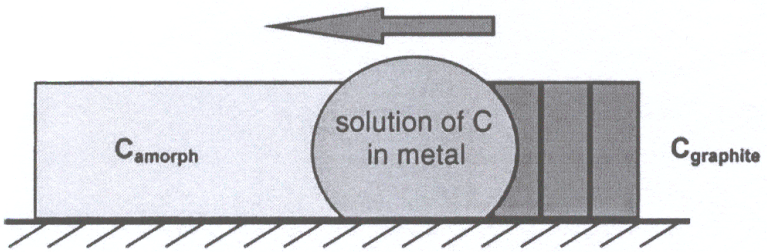

Fig. B.3. Schematic of the fluidification of a nano-particle of catalysing metal in the graphitisation of amorphous graphite. The top arrow indicates the direction of the particle motion [B-8].

Since during graphitisation the chemical potencial of carbon μC in the carbon-metal solution must obey the law μC (amorphous) > μC (in metal) > μC (graphite), the concentration of dissolved carbon in the metal at steady state must be much higher than when the metal is in contact with graphite. Several authors, Parmon [B-8] and Gorbunov [B-11] among others, have determined that the transition to liquid requires absorption of amorphous carbon in approximately the same volume as of metallic particles. The concentration of reactive carbon dissolved can be estimated assuming equilibrium with the amorphous carbon [B-8]:

$$\left[C_{amorphous}\right] = \left[C_{graphite}\right] exp\left(\frac{-\Delta_r G}{RT}\right) \approx 4\left[C_{graphite}\right] \tag{B.3}$$

$[C]_{amorphous}$ and $[C]_{graphite}$ are the concentrations of dissolved carbon in the metal in contact with amorphous carbon and graphite, respectively; and $-\Delta_r G$ is the difference between the Gibb's free energy of the amorphous carbon and the graphite. According to Schröeder's relationship an estimation of the melting temperature of the solution can be easily obtained. The magnitude of the reduction in the melting temperature of the metallic nano-particles may reach 500-900 ºC with regard to the eutectic. This means that in the metal-carbon system, particles melt at lower temperatures the higher their content of carbon.

The reason for this important decrease in the melting point of the catalysing particles compared to pure metal, is the weakening of the bonds and the increase in the fraction of bonds between excited metal atoms, due to their interaction with the dissolved carbon atoms.

The state of the *M-C* particles formed by interaction of the metallic particles with the carbonaceous matrix depends on their size. They can be in liquid state, or partially molten.

Krivoruchko [B-9] carried out a study of the evolution of morphology of different particles, as a function of time. The experiments were accomplished in-situ by *TEM*, with amorphous carbon foils doped with catalysing particles. His main results have been summarised in the following regarding the particle sizes:

- 10-50 nm. Particles melt instantaneously and totally; and immediately afterwards, they start to flow along the surface of the amorphous carbon foil.
- 50-150 nm. Initially, just the outer regions, in contact with the amorphous carbon, turn into liquid. The nucleus of the particles remains solid and immobile. From this point on, the system can progress in different ways:

- The liquid can be reabsorbed by the particle from which it came, leaving and empty space. As a result of successive processes of formation of liquid by super-saturating carbon, melting and absorbing liquid, the concentration of carbon in the particle is high enough to turn it completely into liquid. From that moment on, the *M-C* molten particle starts to move within the carbonaceous matrix.
- The fine crown of *M-C* liquid separates from the nucleus, spawning a liquid particle of about 10-50 nm, that moves independently.

- 150-500 nm. Only the outermost regions of the particles, in contact with the amorphous carbon, turn into liquid. The nucleus, to which barely no carbon from the matrix has diffused, remains solid and motionless.

The catalysing particles experience a gradual change in their size after a series of melting processes, dissolutions and fragmentations during their motion through the matrix. Once fragmented, the particles begin to move independently.

Apart from the cryoscopic effect of the metallic particles super-saturated with carbon, there is another way of influencing the melting temperature of catalysers. The size *r* of the particle tends to reduce the melting temperature of nano-particles smaller than 30-40 nm [B-9]:

$$T_r = T_\infty \, exp\left(\frac{-2\sigma V_m}{R\Delta_m H} \right) \tag{B.4}$$

where σ is the surface tension and *Vm* is the molar volume of the metal. The symbol ∞ refers to a flat particle, which is a particle of infinite size compared with the nano-particle. Nevertheless, the size effect starts to be important only when the particles are smaller than 10 nm.

The exothermal reaction in the transition of amorphous carbon to graphite cannot be responsible for the overheating of the catalysing particles, since it takes place when they are already liquid and begin to move through the amorphous carbon. Moreover, the increase in temperature is of about 10 ºC [B-9], although it may depend on the particle size.

B.2.1.2. Motion of the M-C liquid particles (<30-40 nm) through the amorphous carbonaceous matrix.

As soon as they have formed, the liquid particles start to move in a random fashion through the amorphous matrix, dissolving amorphous carbon on one of their sides and precipitating it on the opposite in the form of graphitic layers (graphenes). Along their motion, the particles leave a graphitic trace behind them, and they can cover distances hundreds of times larger than their own size. The graphene layers that precipitate tend to nucleate in a direction parallel to more or less plane facets of the catalysing particles. The biggest solid particles (>150 nm) remain static.

The *M-C* particles do not react with graphite; thus, the graphitic traces hamper the particle's motion, and forces it to change direction towards areas where amorphous carbon is still available. The result is the formation of winding graphitic traces.

Krivoruchko [B-9] proposes an approximate expression for the rartio of catalytic graphitisation, r_g:

$$r_g = \frac{V_{M-C}\rho}{12} \tag{B.5}$$

where $V_{M\text{-}C}$ is the average speed of the particles in the layer, and ρ is the density of amorphous carbon. The speed $V_{M\text{-}C}$ is much bigger than that of diffusion of carbon in the solid metal, even at higher temperatures. In some cases the difference can be of 2 and 4 orders of magnitude. Kaburagi *et al*. [B-12] suggest that pores can favour particle displacement. This would explain the fact that pores start to close exactly at the temperatures at which the catalytic action of carbides observed in this work begins to be noticeable. Molten carbides flow through the walls of the pores, strangling them.

B.2.1.3. Solidification of the particles

The liquid phase lingers as long as the particles continue to move and the temperature stays constant. As mentioned before, the *M-C* particles do not react with the graphitic phase, which is more stable than the amorphous. Therefore, when the temperature decreases about 30 or 40 degrees, or when no more amorphous carbon surrounds the liquid particles, they stop moving, solidify, and the carbon dissolved in them diffuses towards the surface. Once expelled, carbon crystallises on the surface of the initially metallic particle and turns into carbide. If the speed of segregation is low, the carbon atoms can organise by diffusion, generating a more stable configuration: graphene

layers. Consequently, the particle is quickly encapsulated in the graphite, and the system deactivates irreversibly: since the particles are surrounded by stable graphite, they do not participate in the successive graphitisation processes. If the speed of segregation is high, among other reasons because the cooling speed is high, carbon finds difficulties to diffuse and incorporate into the formed layers. Instabilities arise on the surface and protuberances stick out.

The S-L-S model can be applied to catalytic graphitisation of the doped graphites investigated in this thesis, because the metallic carbides can be considered metallic particles in which atomic carbon occupies interstitial vacancies. These carbides have a relatively wide composition range (except *WC*), hence they can accept more carbon in their net than what they admit at room temperature. Therefore, it may be assumed that the initial particles are metallic particles partially saturated with carbon. With the size distribution of the particles worked till now, they are likely only to melt partially, but catalysers of smaller particle size are expected to be available in the future, and with them a better graphitisation rate will be obtained.

B.3. References

[B-1] W. Delle, K. Doizlik, H. Nickel, *Graphitische Werkstoffe für den Einsatz in Kernreaktoren, Teil 1: Pyrolytisch abgeschiedener Graphit*, Thieming Verlag, München, 1979.

[B-2] W. Delle, K. Doizlik, H. Nickel, *Graphitische Werkstoffe für den Einsatz in Kernreaktoren, Teil 2: Polycristalliner Graphit und Brennelementematrix*, Thieming Verlag, München, 1983.

[B-3] P. Delhaès (Ed.), *World of Carbon, Vol. 1: Graphite and Precursors*, Gordon and Breach Science Publishers, Singapore, 2001.

[B-4] A. Õya and H. Marsh, J. Mater. Sci. **17** (1982) 309.

[B-5] K. H. Hüttinger, Adv. Mater. **2** (1990) No. 8, 349.

[B-6] B.D. Cullity, “Elements of X-Ray Diffraction”, Addison-Wesley Publishing Company, Reading, Massachusetts (1978) p. 99.

[B-7] A. Oya and H. Marsh, J. Mater, Sci **17** (1982) 309.

[B-8] V.N. Parmon, Catalysis Today **51** (1999) 435.

[B-9] O.P. Krivoruchko and V.I. Zaikovskii, Kinetics and Catalysis, **39** (1998) 561.

[B-10] O.P. Krivoruchko, N.I. Maksimova, V.I. Zaikovskii and A.N. Salanov, Carbon **38** (2000) 1075.

[B-11] A. Gorbunov, O. Jost, W. Pompe and A. Graff, Applied Surface Science **197-198** (2002) 563.

[B-12] Y. Kaburagi, H. Hatori, A. Yoshida, Y. Hishiyama and M. Inagaki, Synthetic metals, **125** (2002) 171.

Appendix C

Fine-grain carbide-doped graphites: manufacturing procedure and determination of the thermal conductivity

C.1. Manufacturing procedure

This appendix recapitulates more detailed information about the manufacturing procedure of the doped graphites investigated in this work, which has not been included in the sub-section 3.1.1.

The work accomplished during these years at the *CEIT* has been divided into two stages. The results obtained in the first one served as a starting point for the second, since they supplied useful modifications on the manufacturing procedure to better the final properties. First, the different starting materials used are described. Afterwards, the processing route followed in each stage of the project to optimise the properties, is described. Finally, an explanation about the determination of the thermal conductivity concludes this appendix.

C.1.1. Starting materials

As already mentioned, throughout the project developed at the *CEIT*, two phases can be distinguished: the first corresponds to year 2001, and the second to the following period.

During the first stage, *meso-carbon micro-beads* (*MCMB*) manufactured by Repsol-YPF and mostly micro-mechanised were used as carbon starting material, as well as small quantities of *MCMB* powders elaborated at the University of Alicante.

For the second stage of the project, the remaining *MCMB* powders by Repsol-YPF were used as initial material, and from them 350 samples were produced.

The reason to use *MCMB* carbon powder was the exploration of this novel and very promising path for the production of isotropic fine-grained graphite with significantly improved strength [C-1].

Different metal carbides have been used as dopants: B_4C, α-*SiC*, *TiC*, V_8C_7, *WC* and *ZrC*. Some of their physical properties have been summarised in **Table C.1**. Special care has been taken to the storage of these powders in order to prevent oxidation; although it is difficult due to their great area exposed to it.

	Melting point [C-2] (°C)	Eutectic temperature L ↔ *MC* + graphite [C-2] (°C)	Vapor pressure at 2000 K [C-3] (bar)	Particle size (producer) (μm)	Density [C-4] (g/cm³)	Thermal conductivity at *RT* [C-4] (W/mK)
B_4C	2470	2375	4.5×10^{-8}	~1	2.5	30 – 90
α-SiC	2540	-	2.7×10^{-6}	~1	3.22	~125
TiC	3067	2776	7.6×10^{-10}	~1	4.9	30
V_8C_7	2850	2670	9.4×10^{-9}	0.9 – 1.3	5.7	29
ZrC	3500	2876	3.0×10^{-11}	~3	6.7	29
WC	2785	2785 (Perit.)	4.0×10^{-11}	~0.7; ~0.2	15.6	100

Table C.1. Physical properties of the metal carbides selected as dopants

Nearly all the metallic carbides selected present a catalytic effect on the graphitisation process [C-5]. On the other hand, all these carbides are stable up to very high temperatures (above 2500 °C) [C-6], have a relatively low vapour pressure [C-6] and, except for *SiC* and WC, show a wide stoichiometric range. The eutectic temperature Liquidus ↔ carbide + graphite (if it exists) is also included in **Table C.1**.

The average particle size of the carbides will be of critical importance to the erosion behaviour. It is usually of about ~1 μm, except for *ZrC*, which has an average size of ~3 μm (manufacturer's data), and for *WC*, which is the powder with the smallest particle size (~0.7 μm). During the last stage of the project, a new *WC* powder with an even smaller particle size (~0.2 μm) was acquired. When analysed by *SEM*, the *TiC* and the *WC* (~0.7 μm) powders revealed a narrow distribution and an average size in agreement with the manufacturer's data. Conversely, for *VC* and *ZrC* the distribution was quite wide, with a good number of ~5 μm particles for VC, and 5-10 μm particles for *ZrC*.

The oxygen content (weight %) of the carbides that had been longer stored was measured at the Inasmet technological centre (San Sebastián) obtaining the following results: 5.3 % for *VC*, 2.4 % for B_4C and 0.25 % for *ZrC*. The oxygen content of the other carbides is expected to be negligible. The high oxygen content of *VC* was taken into consideration when preparing the mixture to obtain the desired carbide concentration. That oxygen may account for an increase in porosity after being released during the graphitisation heat treatment, as was actually confirmed.

C.1.2. Production

Fig. C.1 schematically shows the production route followed during the first stage of the project. The results obtained in this first phase evidenced the necessity of improving the route to avoid a series of problems that will be outlined in the following lines.

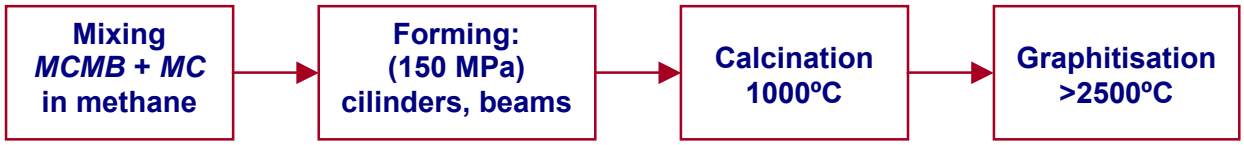

Fig. C.1. Manufacturing route followed during the first phase of the project.

The new production route in the second stage of the project, optimised with the results of stage one, is shown in **Fig. C.2**.

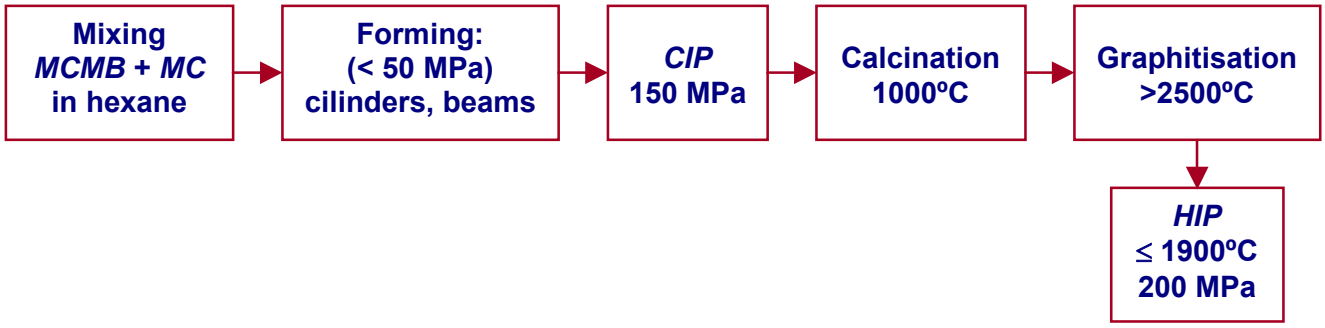

Fig. C.2 New manufacturing route followed during the second phase of the project.

C.1.2.1. Mixing

The manufacture started preparing mixtures of *metallic carbide* powders (*MC*) and a self-sintering powder of *MCMB* in order to obtain about 4 at.% of metal concentration in the final material. For this purpose, the mass loss of the pure *MCMB* carbon powder during the sintering was taken into account, which was measured to be of about 13%.

Obtaining the mixture is a critical step to forestall contamination and achieve a good distribution of the dopants, without agglomerates that would be detrimental to the properties of the material.

During the first stage of the project, the mixtures were prepared using ethanol as liquid light solvent medium in a mixer for 2 hours. In the second stage, to reduce oxidation

of the carbide particles during the mixture, ethanol was substituted by hexane, which is a good dispersing surrounding and is less reactive with the mesophase, obtaining more homogeneous mixtures and avoiding oxidation to a great extent.

Afterwards the mixtures were introduced in a dryer at 90 ºC and 24 hours to eliminate the dispersant environment completely. Once dry, the mixture was then sieved down to approximately 100 μm to reduce the chances of agglomeration.

C.1.2.2. FORMING

Alter the mixture was successfully elaborated and during the first stage of the project, the powders were uni-axially compacted in the shape of cylinders (∅16 mm × 5 mm height) and rods of rectangular cross-section (55×15×~5 mm^3) MPa in a Tinius Olsen press of 30 Tm. The rods were conceived for the flexion experiments (according to norm ISO 4492), from which flexion resistance, Young's modulus and fracture strain was determined for each material after the different heat treatments. The compacting pressure ranged from 100 to 200 MPa, although the majority of the doped samples were compacted with a pressure of 150 MPa.

To steer clear of problems associated to tension gradients formed during the uni-axial compacting process, in the second phase the process was modified performing two types of geometry: cylinders ∅16 mm, and rods 25x7 mm^2, both 5 mm high. The powder was uni-axially compacted at 150 MPa by the floating matrix technique, which closely simulates the compacting process attained with 2 actuators, and reduces density gradients. For every compact, stamps and matrix were lubricated with graphite flakes in the beginning, and with zinc esteorate afterwards.

C.1.2.3. CIP

During the second stage of the project, the uni-axial compacting procedure was replace with *CIP* (*Cold Isostatic Pressing*) at 150 MPa, to avoid growth of cracks by end-capping, to evade density gradients, and to obtain a material as isotropic as possible. Before applying *CIP* the material was uni-axially pre-compacted at 50 MPa to shape it conveniently. Once pre-compacted, they were introduced in latex bags that fit perfectly to the shape of the samples and isolate them from the liquid environment that will transmit the pressure evenly. The mechanical properties of the samples obtained by *CIP* are superior those of samples uni-axially compacted.

C.1.2.4. CALCINATION

Calcination is an intermediate heat treatment between compacting and graphitising, by which organic material transforms into carbonaceous waste. It takes place in an inert environment at temperatures that may reach 1300 ºC. It is a complicated process in which several reactions occur simultaneously (elimination of volatile compounds, formation of radicals, dehydrogenation, condensation, issomerisation, etc.). The removal of volatile compounds is a crucial step and must transpire at low speed to prevent disorganisation or rupture of the carbonaceous net, reason why it is a slow process.

Up to 600 ºC sintering occurs in a transitory liquid phase, and the majority of the volatile compounds are expelled. From that temperature up to 1000 ºC volatile compounds continue to be released, at a much lower rate, and the material now sinterises in a solid phase.

Calcination is carried out in a *RWF* furnace in a nitrogen atmosphere at 1000 ºC, following the next cycle:

- heating from *RT* to 600 ºC at a speed of 0.5 ºC/min

- heating from 600 ºC to 1000 ºC at a speed of 2 ºC/min

- dwell at 1000 ºC during 1 hour

- free cooling

Alter calcination, the material is exclusively constituted by carbon atoms, but its structure is not very well ordered and consists of an aggregate of small crystals. Each of these agglomerates is formed by small layers that have a very similar molecular structure to that of graphite, with some degree of parallelism, and normally some imperfections.

C.1.2.5. GRAPHITISATION

Graphitisation cycles of the sintered samples were performed in two different graphite furnace*s: a Jones v*acuum furnace, which reaches a maximum temperature of 2500°C, and other furnace of the company *Thermal Technology* (*TT*), which can heat up until 3000°C. The graphitisation cycles in the *Jones* furnace and in the *TT* furnace were performed in argon and helium atmosphere, respectively. The heating rate for all doped samples was 20°C/min from 25 to 1000°C (calcination temperature) and 10 °C/min from 1000°C to the maximum temperature. Some graphitisations were performed with a lower

heating rate of 10°C/min in the whole temperature range, to investigate the influence of the heating rate on the final properties of the undoped material.

Throughout the second stage of the project some variations in the graphitisation cycle were incorporated. Thus, the effect of maintenance time was studied and increased to 2 hours. The heating speed was also modified, and in some cases decreased down to 5ºC/min.

C.1.2.6. HIP

In the second stage too, after the graphitisation process, a series of cycles were performed in a *HIP* (*Hot Isostatic Pressure*) press at 200 MPa and two different temperatures, 1700 and 1900 ºC, for the doped samples. The aim was to improve the mechanical properties by achieving a higher density, since the porosity of the doped materials after graphitisation was proved to be practically closed, allowing the use of *HIP* without encapsulation.

C.2. Determination of the thermal conductivity

The *thermal conductivity*, *k(T)*, of the graphitised samples has been determined from the *thermal diffusivity*, $\alpha(T)$, the *heat capacity*, *C(T)*, and the *geometric density*, ρ, according to the following expression:

$$k(T) = \alpha(T) \cdot \rho \cdot C(T) \qquad \text{(C.1)}$$

$\alpha(T)$ was gauged by the *Laser Flash* method at *IPP-Garching*, in the 20 to 1200 °C temperature range. In the case of some samples, for which determining the maximum conductivity was of interest, the diffusivity was also measured below *RT* down to -160 °C, by the *Laser Flash* method too. These low temperature measurements were undertaken at the *Oak Ridge National Laboratory* (ORNL, USA).

Fig. C.3 displays as example the results obtained for some doped graphites produced at *CEIT*.

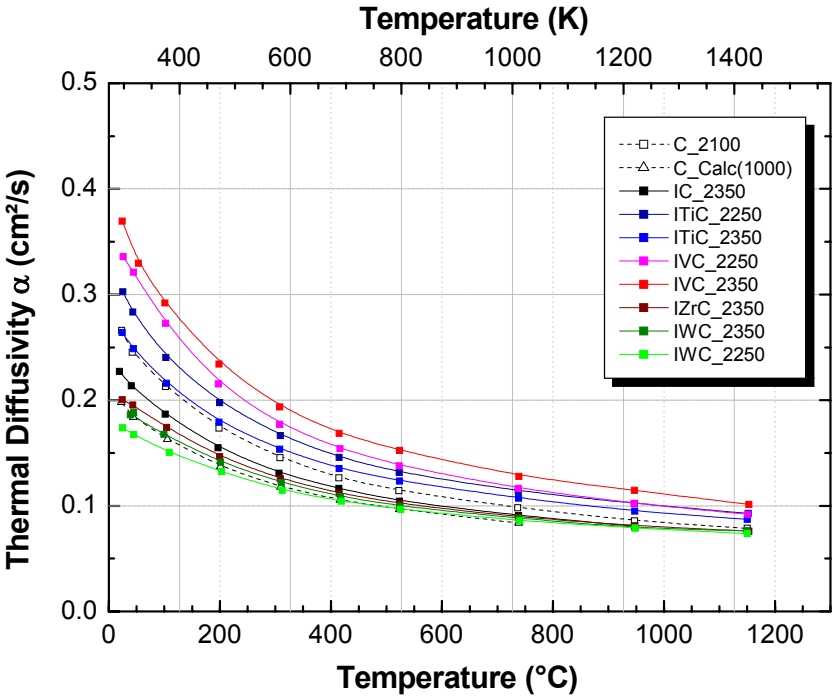

Fig. C.3 Thermal diffusivity of some carbide-doped graphites produced at *CEIT* (4 at.% of metal) as a function of the temperature.

C(T) was calculated from literature data for graphite and the corresponding carbides [C-7], taking into account the concentration of carbides in each sample. **Fig. C.4** shows the heat capacity for the doped graphites developed at *CEIT*.

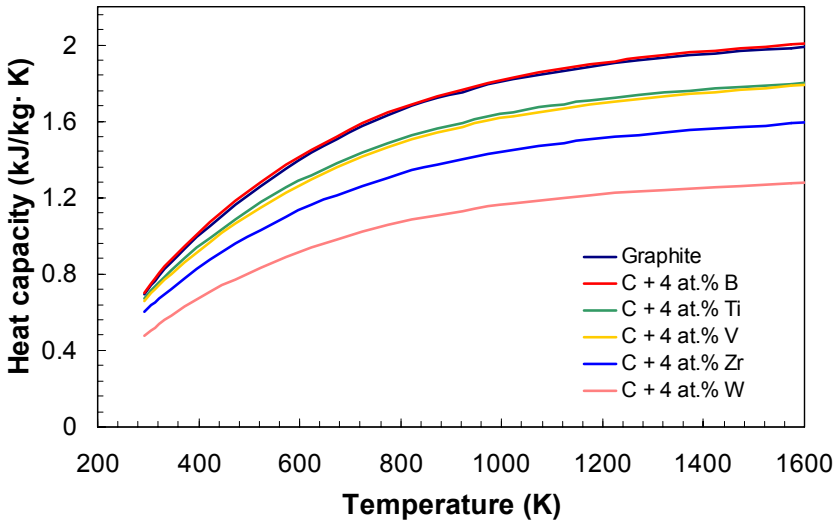

Fig. C.4. Heat capacity as a function of temperature for some carbide-doped graphites produced at *CEIT* (4 at.% metal) [C-8].

The calculated values of heat capacity were compared with other experimental values of similar doped graphites took from the literature [C-7], which were measured by scanning differential calorimetry, and a good agreement between both results was found.

C.3. References

[C-1] K. Hüttinger, Adv. Mater. **2 (8)** (1990) 349.

[C-2] Binary Alloy Phase Diagramms, T.B. Massalski (Ed. In Chief), American Society for Metals vol. **1** (1986).

[C-3] B. Sundman, B. Jansson and J.O. Andersson, "The Thermo-Calc Databank System", Calphad **2** (1985) 153.

[C-4] R.J. Kotelnikof, "Handbook on Super Refractory Materials", Metallurgy publisher, Moscow (1976).

[C-5] A. Oya and H. Marsh, J. Mater. Sci. **17** (1982) 309.

[C-6] C. García-Rosales and M. Balden, J. Nucl. Mater. **290-293** (2001) 173.

[C-7] B.N. Enweani, J.W. Davis and A.A. Haasz, J. Nucl. Mater. **224** (1995) 245.

[C-8] C. García-Rosales and N. Ordás, "Desarrollo y caracterización de materiales grafíticos dopados de buenas propiedades plasma/pared para su exposición al plasma de TJ-II", Techn. Rep. *CEIT* IFINAL/1247/R01, Centro de Estudios e Investigaciones técnicas de Gipuzkoa, San Sebastián (2004).

Appendix D

Characterisation of the mono-energetic deuterium ion beam profiles

Rutherford Backscattering Analysis (*RBS*) at a scattering angle of 165° with 1.5 MeV incident protons was used for the analysis of the flux distribution of deuterium on the bombarded samples and the spot size. For each studied point, the thickness of the amorphous hydrogenated carbon layer deposited on the silicon wafer can be calculated from the *RBS* spectra (**Fig. D.1**).

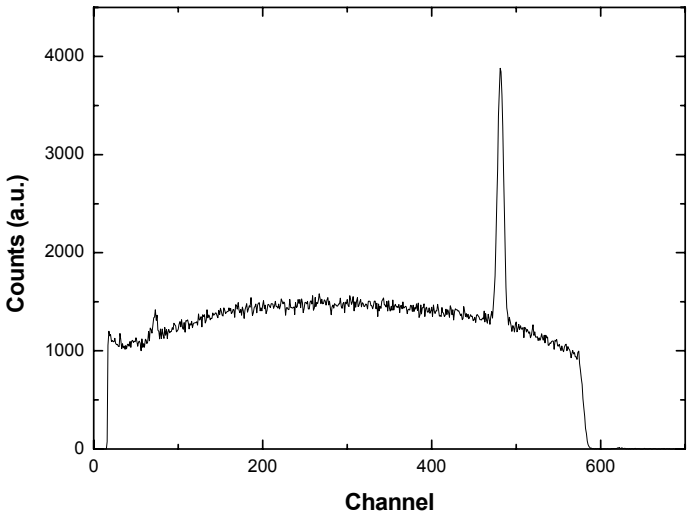

Fig. D.1. RBS spectrum obtained for a target with an *a-C:H* film deposited on a silicon wafer.

The thickness of this thin film in each point can be calculated with the following equation:

$$\delta_C(At/cm^2) = \frac{N_c e \cos\alpha}{Q\Omega \frac{d\sigma}{d\Omega}} \qquad \text{(D.1)}$$

where,

δ_C is the layer depth (at/cm^2),

N_C is the integrated intensity of the peak due to the carbon,

e is the electron charge (C),

α is the incidence angle,

Q is the incident charge (C),

Ω is the solid angle of the detector (1.08×10^{-3} sr)

and $\frac{d\sigma}{d\Omega}$ is the differential cross section (168.8 mbarn/sr; 1 mbarn = 10^{-27} m^2)

Acknowledgments

I never ever thought I would come to the point to write this page of acknowledgements, which is to be honest, not only the most pleasant but also the most difficult duty finishing such a PhD thesis. Three years have passed by since I started it at the Max-Planck-Institut für Plasmaphysik and now – as it seems to me not more than a moment later – it is time to thank all the people who have helped to make this dream come true.

Prof. Dr.-Ing. Dr.-Eng. Hans-Harald Bolt, who provided me the great opportunity to work in this reputable institute among the wonderful Materials Division team, being always available to listen to my concerns and taking me serious.

Prof. Dr. mont. habil E. Werner, who gave me the chance to take my doctor's degree at the TU Muenchen and for reviewing this work.

Prof. Dr. Carmen García-Rosales, who was the one that recommended this place to me. I owe her a lot. She had accompanied me during my course of studies in San Sebastián. But also during my PhD time here in Germany she kept being a person to turn to and to learn from.

Dr. Joachim Roth, who encouraged me to carry on when I was in doubt. Although he was very busy sometimes, he never left the laboratory without having a look at my results and discussing them. I admire his calmness and ability to keep the general scientific overview.

Dr. Martin Balden, my tutor, who deserves my deepest gratitude and most appreciative words. His permanent assistance, advice and infinite patience taught me, that drawing attention to the details is the same important as keeping the eye on the priorities of my work. With his inexhaustible knowledge and great experience Martin has always been open for any kind of explanation and critical discussion. At the beginning I had some problems with his speed of speaking. Yet he was the best tutor I could have had!

Ignacio Quintana for his sacrificing correction of my English in spite of the big distance and the time difference, which is between us now. Furthermore I would like to thank him

not only for being a reliable and discerning colleague during his IPP time but also for being a friend.

Dr. Rainer Behrisch, which has contributed a lot of suggestions and ideas to this work. Using his decades of experience he made me aware of critical points, which I am really grateful for.

Dr. Hans Maier, functioning as a kind of encyclopaedia, he is the man to explain Physics in an every day language and was always ready to help me no matter what, no matter when.

Dr. Klaus Schmid, whose Austrian is not quite easy to understand, I would like to thank for reading through this PhD work last minute.

Freimut Koch for solving my computer problems and Stefan Lindig for always having a kind word.

All the technicians of the laboratory, especially Gabriele Matern, Arno Weghorn, Joachim Dorner, Michael Fußeder and Peter Matern. Watching how helpless I am without them showed me how valuable their work is. Thanks again to Arno for trying to teach me some Bavarian and for making me laugh about it.

Dr. Thomas Schwarz-Selinger for always taking the time to assist me, especially on how to use the Quadrupol.

Carmen Popescu for having been the funniest office mate I ever had.

All the people I might get to know living in the student's residence "Aurach", especially Maria Díaz, Muriel Honhon, Quinita Olmedo, who have made these three years an unforgettable experience for me and Franziska Rack, who spontaneously lend me her notebook when mine was broken and who I spent hours and hours working in the "Studienraum" with.

Last but not least very special thanks to my parents for standing behind me in every single part of my life and for enabling me to realise my studies as well as this PhD. In fact I thank them for loving me the way they do.

All of the above and many others have contributed substantially in one way or another to the preparation of this thesis. I express my deepest gratitude and appreciation to all of them. In case I really forgot to mention anybody here, please believe me, this did not happen on purpose.